HIGH RESOLUTION THERMAL IMAGING FOR ELECTRICAL AND OPTICAL CHARACTERIZATION OF ELECTRONIC AND PHOTONIC DEVICES

by

Kwok-Leung Chan

A dissertation submitted in partial fulfillment
of the requirements for the degree of
Doctor of Philosophy
(Mechanical Engineering)
in the University of Michigan
2007

Doctoral Committee:

Assistant Professor Kevin Patrick Pipe, Chair
Professor Pallab K. Bhattacharya
Associate Professor Katsuo Kurabayashi
Assistant Professor Max Shtein

Acknowledgements

To my advisor Professor Kevin Pipe, I am grateful for his advices, coaching, support and assurance thought out the whole course of my doctoral degree. His guidance has helped me to attain and to uphold high quality research work. Fruitful discussions on topics related to our research interests had not only enriched my knowledge, but also sparked my motivation to explore the realm of fundamental thermal physics and to become a sedulous scholar. I would also like to thank Professor Max Shtein, the advisor of my research related to organic materials. He has shed insights on my research and taught me lots presentation skills both inside and outside the laboratory. I am greatly moved by his passion and ideas in research. As a role model, his presence is invaluable to my future career. Professor Pallab Bhattacharya, one of my dissertation cognate committee members, had taught me important lessons when I was a new comer to the field of semiconductor laser diode. Thanks to his provision of quantum dots lasers, I was able to carry out experiments that yielded valuable findings. Professor Katsuo Kurabayashi, also a member of my dissertation committee, had offered me countless suggestions on my research as well as insights on my findings. Through the courtesy of Professor Kurabayashi, I was able to borrow the equipments that are crucial in my experiments.

The success of my research also involves hard work from the collaborators. I would not be able to complete my thesis without their contributions. I would like to this opportunity to acknowledge Dr. Zetian Mi, and Jun Yang for their excellent work in quantum dot laser fabrication and their continual provision of lasers. I also wish to show appreciation to Dr. Paul Juodawlkis and Jason Plant at Lincoln Laboratory – Massachusetts Institute of Technology for providing the slab coupled optical waveguide laser. I would like to thank Prof. Zhenqiang Ma and Guoxuan Qin at the University of Wisconsin for providing the Si/Ge heterojuncion bipolar transistor. I am also grateful for Dr. Dietrich Lüerßen's advices on the experimental setup of the hardware and his provision of the thermoreflectance LabVIEW program.

My years in Michigan have been spectacular. Not only had I gained tremendous amount of knowledge, I had also found lifelong friendships. I would like to thanks all of my group mates: Kwang Hyup An for teaching me the AFM skills; Andrea Bianchini for having regular headstrong discussions on physics with me at 2 a.m.; Shaurjo Biswas for teaching me the vapor jet deposition; Peter Burgardt for the Chinese Kung-Fu training; Chelsea Chen for teaching me the spin coating techniques; Shuo Chen for the advices on simulation; Chelsea Haughn for assisting me in the pentacene deposition; David Heiser for setting up the purification system; Jingjing Li for the online encouragement; Brendan O'Connor for showing me the deposition tricks and for having discussion on DNA; Amul Sathe for assisting in the experiments; Abhishek Yadav for studying Rabi floppy oscillation and the ultra fast – phase change phenomena with me; and Yiying Zhao for the training on SEM and Mandarin. Certainly, I would like to thanks my best friend Prof. Xiulin Ruan at the Purdue

University for his unconditional support throughout the last five years of my time in Michigan. I would like to give special thanks to Bongsup Shim and Kwang Hyup An who re-introduced me to God that allowed me to have a much deeper understanding of God.

Last but not least, I would like to thank my parents, Kai Kuen Chan and Yuen Ching But, my brother, Andy, and my sister, Sharon for their love and support from the other side of the earth. Their encouragements gave me power to defeat uncountable lonely nights doing experiment especially in the winter. I would also like to thank God for bringing Phyllis to my life. Her endless support, patience, confidence and love has given me courage to overcome all the hurdles in my 9-year journey to become a successful scholar. No word in the world could express my love to her.

This work is supported by the Defense Advanced Research Projects Agency through the EPIC program under Grant No. W911NF-04-1-0429.

Paddy Chan

Ann Arbor, Michigan

2007

Table of Contents

Acknowledgement……..... ii

List of Figures……..... viii

List of Tables……..... xvii

Abstract……..... xviii

Chapter 1 1

Background 1

1.1 Introduction..... 1

1.2 Heat generation and transfer in electronic devices 4

1.3 Micro- to nanoscale temperature measurement approaches 7

1.3.1 Thermocouple 7

1.3.2 Scanning Thermal Microscopy 11

1.3.3 Infrared radiation thermometry..... 13

1.3.4 Thermoreflectance 14

1.4 Thermoelectric measurements used to characterize device-relevant material properties..... 15

1.5 Summary 16

Chapter 2 20

Thermoreflectance and microscale temperature measurement techniques.....20

2.1 Introduction and background 20
2.2 Error due to carrier density induced index change 24
2.3 Thermoreflectance equation 25
2.4 Detection of thermoreflectance signal (ΔR/R) 26
2.5 Measurement setup 30
2.6 Calibration of the thermoreflectance coefficient (κ) 31
2.7 Summary 33
Chapter 3 35
Profiling carrier dynamics in a high power heterojunction bipolar transistor (HBT) by CCD-based thermoreflectance 35
3.1 Introduction 35
3.2 Qualitative analysis of thermal instability in HBTs 39
3.3 Prior simulation and experimental work on temperature and current mapping of HBTs 47
3.4 Thermoreflectance imaging of a SiGe HBT 48
3.5 Thermal circuit of two-finger HBT for profiling current 52
Chapter 4 57
High resolution temperature mapping and thermal lensing in high-power laser diodes 57
4.1 Introduction 57
4.2 Slab coupled optical waveguide laser (SCOWL) 58
4.3 Temperature measurement of SCOWL facet 61
4.4 SCOWL thermal circuit and heat transfer mechanisms 64
4.5 Thermal lensing in high power edge emitting laser diodes 70

4.6 Optical coupling efficiency between the SCOWL and single mode optical fiber 75
4.7 Summary 77
Chapter 5 79
Temperature measurements of a pulsed InGaAs/GaAs quantum dot laser 79
5.1 Introduction 79
5.2 λ=1.1μm InGaAs quantum dot laser 81
5.3 CCD-based thermoreflectance for pulsed devices 83
5.4 Thermoreflectance images of a pulsed InGaAs quantum dot laser 87
5.5 Thermal relaxation time constant 91
5.6 Summary 93
Chapter 6 94
Pentacene thin film transistor characterization by microscale thermal measurement 94
6.1 Introduction 94
6.2 Carrier transport in pentacene 95
6.3 Derivation of transistor channel thickness and carrier concentration 98
6.4 OTFT fabrication 101
6.5 Method and results for measurement of Seebeck coefficient, trap density, and channel thickness 101
6.6 Summary 107
Chapter 7 108
Conclusion and suggestions for future work 108
Bibliography 114

List of Figures

Figure

1.1 The power density increase trend of microprocessor chip the past 15 years [1,2]……. 3

1.2 Length and time scale regimes of various microscale to macroscale heat transfer treatments [3]……. 3

1.3 SEM image of a GaAs-AlGaAs laser diode facet after catastrophic optical damage [8]. ……..... 5

1.4 (Left) SEM image of a carbon nanotube field emitter on a silicon cantilever tip. (Right) SEM image of a cantilever tip after melting failure [11,12]…… 5

1.5 (Left) The infrared thermograph of the OLED at V=22V. (Right) The thermograph of the same device at V=33V. A significant temperature increases at the central region of the device can be observed. [13]…… 6

1.6 SEM image of the OLED in Fig. 1.5 after thermal breakdown of the device. [13]…….. 6

1.7 Schematic of the working principle of a thermocouple. Metal 1 (Metal 2) is an n-type (p-type) material, and electrons (holes) diffuse from the high temperature measurement point to the low temperature reference point. The resulting thermal voltage is measured by the voltmeter…… 9

1.8 If the thermal mass of the thermocouple is larger than the device under measurement, the thermocouple behaves as an external heat sink and cools down the device (the color map here represents a temperature scale). ……..... 10

1.9 (Top) Au/Pd thermocouple probes for scanning thermal microscopy made by electron beam lithography and silicon micromachining. (Bottom) Schematic of a thermistor-based scanning thermal probe. [25,26]…… 12

1.10 The spectral emissive power of blackbody at different temperatures……..... 14

1.11 Schematic illustration of the setup used to measure an applied temperature gradient and induced thermal voltage within a pentacene thin film..…….. 16

1.12 An overview of the presented work…….. 19

2.1 (Left) The normalized radial temperature profile of a VCSEL at different lasing modes. (Right) The optical mode profiles of the VCSEL at different bias levels [21]……. 23

2.2 Transient thermoreflectance response of a 23 nm Au film. G is the electron-phonon coupling factor [27]……. 23

2.3 Schematic of the bias signal sent to the device (blue), external frame trigger signal sent to the CCD camera (blue), and reflectance signal captured by the CCD camera (red)……... 26

2.4 The uncertainty (standand deviation of ΔR/count) of the Opteon 12-bit CCD camera as a function of counts and number of iterations [33]…… 29

2.5 CCD-based thermoreflectance experiment setup…….. 31

3.1 The cross-section view of a npn bipolar junction transistor. E, B, C are representing the contact pads for emitter, base and collector respectively. The arrows are representing the direction of the current [46]…… 37

3.2 . (Top) Current paths for the bipolar junction transistor when biased in active mode. (Middle) Band diagram of the BJT under zero bias (equilibrium condition). (Bottom) Band diagram of the BJT under an active mode bias in a common emitter configuration with the base-emitter junction under forward bias and the collector-emitter junction under reverse bias [46]…… 38

3.3 (Top) Band diagram of a heterojunction bipolar transistor under normal operation without heating. (Middle) Increase or (Bottom) decrease of injection efficiency due to heating, depending on the relative decrease in ΔE_C vs. ΔE_V……... 41

3.4 Optical image of a multifinger heterojunction bipolar transistor with a total of nine emitter fingers…… 42

3.5 The collector current of an InGaAs/InGaAsP HBT as a function of base current and collector-emitter voltage [51]……. 43

3.6 The collector current of an AlGaAs HBT as a function of collector-emitter bias and base current. Two separate region of collector current decrease can be observed [50]……... 44

3.7 (Left) The simplified circuit represents the normal operation of a two finger transistor. (Right) The circuit represents the same transistor under current hogging when the voltage increases. I_h is the current passing through the hot finger and I_c is the current passing through the cold finger. Under current hogging, I_h is larger than I_c and I'_c is smaller than I_c.……..... 45

3.8 Total collector current of an HBT biased by a constant voltage source across its base-emitter junction [54] ……. 46

3.9 Individual collector currents of a 2-finger HBT biased under constant V_{BE}. The dotted line is the collector current of the hot finger, and the solid line is the collector current of the cold finger, isolated by means of ion implantation [54]..... 46

3.10 Two-finger high-power SiGe HBT used for thermoreflectance measurement of current dynamics.…… 50

3.11 (a) Optical image (R). (b)-(f) Normalized thermoreflectance images ($\Delta R/R$) of the SiGe HBT at different V_{CE} biases for V_{BE} =1.52V……..... 51

3.12 Thermal circuit of the two-finger HBT. R_{th} is the thermal resistance from the finger to the substrate, R_{12} is the coupling thermal resistance between the fingers, and T_1, T_2, and T_0 are the left/right finger temperatures and heat sink temperature, respectively……. 53

3.13 (Top) Current ratios and (b) Total currents for the left and right emitter cells, derived by thermoreflectance imaging…… 55

4.1 (Top) Schematic of the slab coupled optical waveguide laser (SCOWL) structure. (Bottom) Top view of a SCOWL device, the wires are for hole injection into the top p-cladding. A micro-thermocouple was shown for performing thermoreflectance coefficient calibration…… 60

4.2 The setup for CCD-based thermoreflectance on SCOWL. A 45 degree silver coated mirror is used to focus on the laser facet…….. 62

4.3 Optical and thermal reflectance images of the SCOWL at different bias levels…….. 63

4.4 (Right) The thermal circuit of the slab coupled optical waveguide laser. (Left) The temperatures of different region of the device. $T_{p\text{-}cladding}$ is the p-type cladding temperature on top of the quantum well. T_{active} is the quantum wells temperature. $T_{substrate}$ is the substrate temperature……. 65

4.5 (Top) The average temperature measured by thermoreflectance at different regions of the SCOWL. (Bottom) The total non-radiative recombination power in the SCOWL active region calculated using the thermal circuit model and the measured temperatures at the active region, *p*-cladding, and substrate…… 68

4.6 First and second harmonics of the thermoreflectance signal at I=2.4A. The second harmonic thermoreflectance signal is much weaker than the first harmonic, suggesting that Joule heating is negligible at the facet. Inset shows the location of the center line [82]……..... 69

4.7 (Top) Experimental results of the SCOWL optical mode intensity measured by a phosphor-coated Si CCD camera focused through an attenuator on the facet (courtesy of J. Plant, MIT Lincoln Lab). (Bottom) Horizontal mode profiles taken at the dotted lines shown in the top figure, demonstrating thermal lensing……... 73

4.8 Finite-element simulation of the optical mode size as a function of bias. The measured two-dimensional temperature maps are used in the finite element model as input parameters. (Bottom) Horizontal mode profiles taken at the dotted lines shown in the top figure…… 74

4.9 Normalized $1/e^2$ mode-field diameter of the optical mode in the x and y directions. The x direction has an 18% drop as the current increases from 1 to 4 A……. 75

4.10 The predicted coupling efficiency between a SCOWL and single mode optical fiber, assuming thermal lensing as measured in Section 4.5. The core diameter of the fiber is assumed to be 3.1 μm…….. 77

5.1 Heterostructure design of the λ=1.1μm quantum dot laser under test……. 82

5.2 Scanning electron microscope image of the laser facet……..... 82

5.3 Experimental setup for high frequency CCD-based thermoreflectance…….. 84

5.4 Simulated active region temperature response to 120mA current pulses at 10kHz with 30%, 60%, 90%, and 100% duty cycles..... 85

5.5 Thermoreflectance image of the peak temperature of a InGaAs QD laser under bias at 120 mA, 10 kHz, and 90% duty cycle……. 88

5.6 Vertical (top) and horizontal (bottom) cross-sections of the peak temperature for bias at 10 kHz, 90% duty cycle, and 120 mA…….. 89

5.7 (Top) Current pulse train sent to the laser diode. (Bottom) Actual temperature response of the active region (gray) and the measured time-averaged response (red-shaded)…… 90

5.8 Active region temperature at 10kHz bias with different assumed thermal relaxation time constants. The dark line is the thermal response assuming a τ of 4 μs, and the blue line is the thermal response assuming a 40 of μs…… 92

5.9 Experimental and simulated results of active region temperature at different thermal relaxation time constants as a function of duty cycle. The thermal relaxation time of the device is observed to be approximately 30μs. …… 92

6.1 Hopping transport mechanism in organic materials, according to the Miller – Abraham model [101]……... 96

6.2 The carrier density of states at the HOMO and LUMO levels of an organic semiconductor……. 97

6.3 Density of states (DOS), carrier concentration, mobility, and conductivity as a function of energy [107]…… 98

6.4 I_D against V_{DS} at different gate voltage bias (-40V to 0V)…… 103

6.5 Measured thermal voltage of the 50nm pentacene thin film transistor at $\Delta T = 1.5K$…….. 103

6.6 Histogram plot of the thermal voltage in Fig. 6.5 measured over time. The red line represents the two best fit Gaussian curves……. 104

6.7 Measured Seebeck coefficient of the pentacene thin films at different thicknesses. The error bars represent the standard deviation values obtained in the Gaussian fitting of Fig. 6.6…… 105

6.8 Field effect mobility and transistor channel thickness as a function of pentacene film thickness……... 109

7.1 Schematic of the thermotransimattance working principle. In similar fashion to thermoreflectance, the bias signal is sent to the device (blue), the external trigger signal is sent to the CCD camera (green), and the transmittance signal is captured by the CCD camera (red)……... 111

7.2 A schematic of a CCD-based thermoreflectance setup using a monochromatic filter on a broad-band light source……. 112

7.3 A schematic drawing of a UV CCD-based experimental setup 113

List of Tables

Table

1.1 Commonly used thermocouple metal pairs and their operating temperature ranges……..... 10

2.1 Thermoreflectance coefficient of different semiconductor materials used in the experiment…….. 33

6.1 Threshold voltage, turn on voltage, trap density, Seebeck coefficient and mobility of the pentacene OTFT at different film thickness……. 106

Abstract

The impact of heating on electronic and optoelectronic devices is becoming increasingly severe as devices scale to smaller and smaller sizes. High temperature not only reduces most performance metrics, but also decreases device lifetime. In order to study and understand these problems, an important step is to measure temperature at small size scales.

Here we show how CCD-based thermoreflectance temperature measurement can be successfully applied to heterojunction bipolar transistors, quantum well lasers, and quantum dot lasers for device thermal characterization with a spatial resolution of 400 nm and a temperature resolution of 10 mK. Indeed, the high spatial resolution of this technique allows one to resolve separate heat sources within a device itself; rather than viewing the entire device as a monolithic heat source, we are able to study the separate internal heat transport mechanisms that often exist.

Specifically, in applying CCD-based thermoreflectance to SiGe-based heterojunction bipolar transistors, we show how temperature mapping can be used to spatially profile device current, including asymmetric behavior such as current hogging. In examining a type of high-power laser, we show how (with proper light filtering) 2D temperature profiles of the facet can be measured and linked to thermal lensing. We then describe how the CCD-based thermoreflectance setup can be modified to accommodate pulsed devices, demonstrating the technique on pulsed InGaAs quantum dot lasers and identifying separate temperature peaks due to active region heating and contact heating.

Finally, we discuss how the measurement of thermal and thermoelectric properties in organic thin films can be used to derive fundamental and device-relevant electrical properties related to interface transport. By measuring the Seebeck coefficient of an OTFT, we show that one can for the first time successfully evaluate the channel thickness in a non-destructive fashion without further fabrication processes.

Chapter 1

Background

1.1 Introduction

Thermal characterization of electronic devices is becoming increasingly important due to the use of nanoscale fabrication technologies to create devices of smaller and smaller size. As the number of devices per area increases rapidly, the power density [W/cm^2] dissipated as heat by the devices increases dramatically. For example, the International Technology Roadmap for Semiconductors (ITRS) predicts that by 2010 the power density of a microprocessor will approach that of a rocket nozzle ($1000W/cm^2$) as shown in Fig. 1.1 [1,2] Because temperature has an adverse affect on nearly all device performance characteristics, such heating will certainly become a barrier to the future development of submicron electronic devices; this motivates the study of heat generation and transfer mechanisms in micro to nanoscale devices.

At different time and length scales, the approaches to study nanoscale energy transfer are different. Fig. 1.2 shows the relevant regimes of the Schrödinger equation, molecular dynamics, the Boltzmann transport equation, and the Fourier equation in the

study of energy transfer [3,4] A number of computational and analytical micro to nanoscale heat transfer studies have been performed based on molecular dynamics and Boltzmann transport, including prediction of the thermal conductivity of nanocomposites [5] and superlattices [6], and phonon generation/transport in sub-90nm metal oxide semiconductor field effect transistors (MOSFETs) [7].

A number of experimental investigations have also been done in the area of micro to nanoscale thermal transport. In the following sections, we discuss the issues and challenges induced by heating in electronic devices and provide a detailed comparison of the relevant temperature measurement techniques.

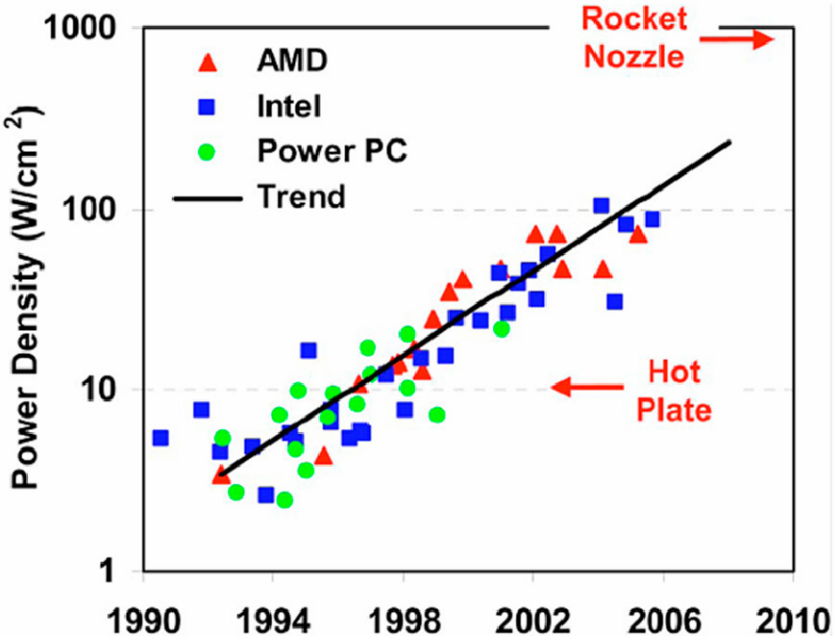

Fig. 1.1: The power density increase trend of microprocessor chip the past 15 years [1,2].

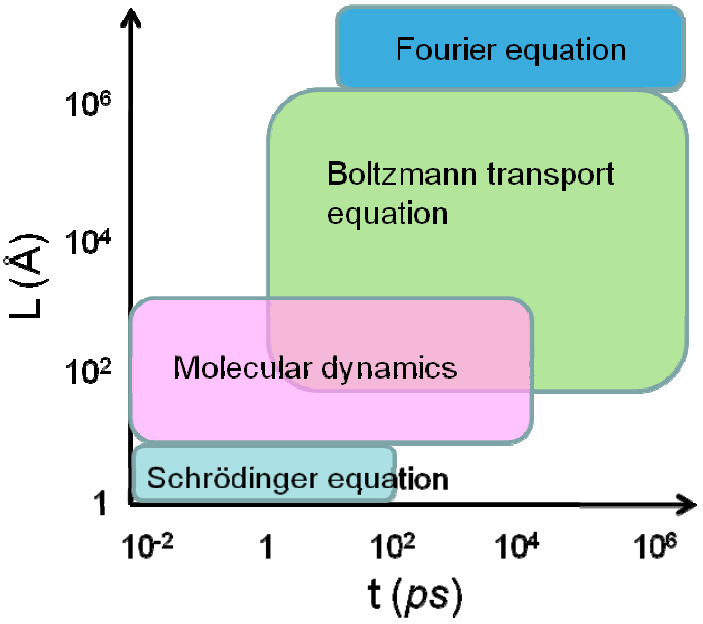

Fig. 1.2: Length and time scale regimes of various microscale to macroscale heat transfer treatments. [3]

1.2 Heat generation and transfer in electronic devices

As discussed in the previous section, heat generation in modern electronic and optoelectronic devices is one of the main problems that must be overcome in order to develop smaller, faster, more powerful, and more reliable devices. Unwanted heating can not only decrease efficiency but also cause breakdown of a device. An example of heat-induced failure is the catastrophic optical damage of a laser diode facet. In a quantum well laser diode, heat generation due to non-radiative recombination (such as Auger recombination) in the active region can produce a significant amount of heat and melt the laser facet (as shown in Fig. 1.3[8]). This melting destroys the photon reflection feedback mechanism, and as a result the diode no longer emits coherent photons. Similar thermal problems exist in structures in which electrical current is funneled into a small region. For example, scanning probe tools using carbon nanotube (CNT) tips [9,10] have demonstrated melting and failure of the probe tip (as shown in Fig. 1.4 [11,12]) when the CNT is in field emission mode, due to electrostatic fields as high as 108 V/cm causing tip temperatures above 1700K. Another device that suffers from thermal dissipation is the organic light-emitting diode (OLED). Fig. 1.5 shows an infrared camera thermal image of an OLED at V=22V and 33V biases respectively. It can be seen that at high bias a region of the OLED significantly increases in temperature, which leads to thermal breakdown of the device [13]. Fig. 1.6 shows a scanning electron microscope (SEM) image of the OLED in Fig. 1.5 after thermal breakdown.

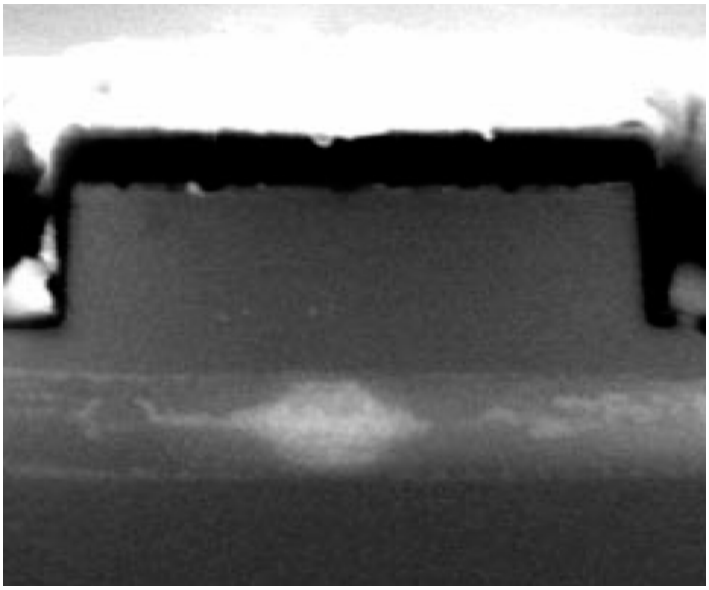

Fig. 1.3: SEM image of a GaAs-AlGaAs laser diode facet after catastrophic optical damage [8].

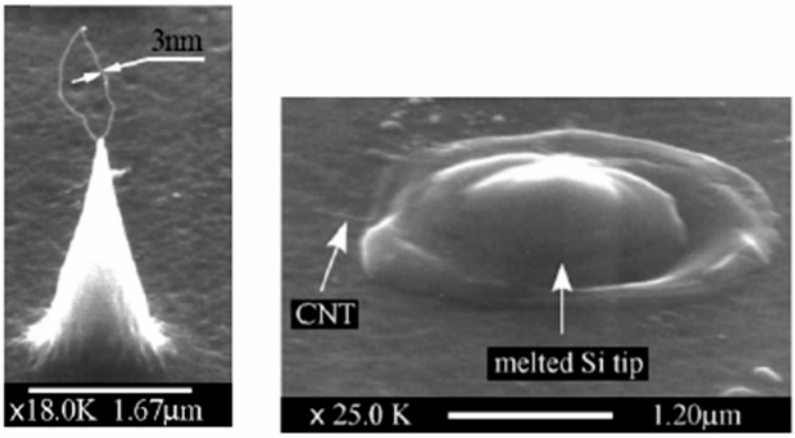

Fig. 1.4: (Left) SEM image of a carbon nanotube field emitter on a silicon cantilever tip. (Right) SEM image of a cantilever tip after melting failure [11,12].

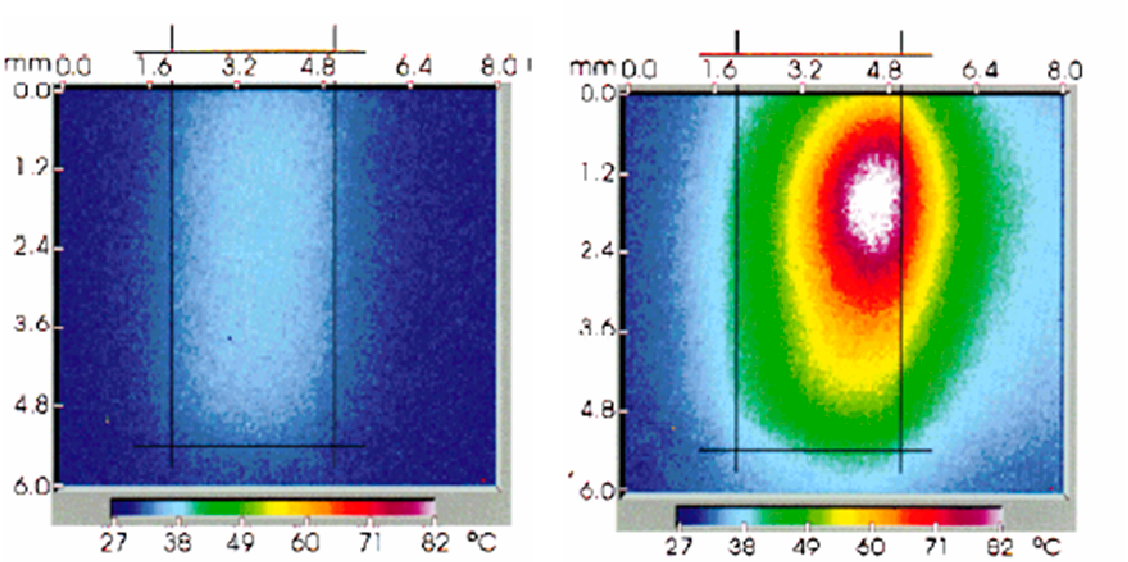

Fig. 1.5: (Left) Infrared thermograph of an OLED at V=22V. (Right) The thermograph of the same device at V=33V. A significant temperature increase at the central region of the device can be observed. [13]

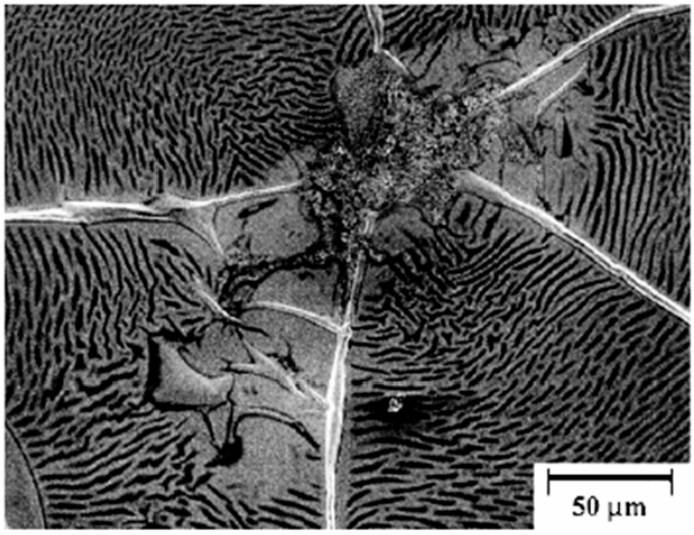

Fig. 1.6: SEM image of the OLED in Fig. 1.5 after thermal breakdown of the device. [13]

1.3 Micro- to nanoscale temperature measurement approaches

Since heating can greatly affect device reliability and performance, various microscale and nanoscale temperature measurement techniques have been developed to investigate thermal effect in electronic devices; such techniques can be distinguished based on their operating mode: contact mode versus non-contact mode.

For contact mode temperature measurements, the temperature sensing unit touches the sample. Typical detection approaches include thermocouples, thermistors, and scanning thermal microscopy (SThM) probes. [14,15,16] Non-contact (remote) temperature detection is usually accomplished by optical techniques such as thermoreflectance or an infrared camera [17,18]. In laser diodes, average active region temperature can be obtained directly by measuring the emission spectrum of the laser diode and correlating the emission peak shift with heating in the active region [19]. In the following sections, the fundamental principles of different temperature measurement methods and their current state of the art will be discussed.

1.3.1 Thermocouple

A thermocouple is composed of two dissimilar metal wires that are joined at one end and attached to a voltmeter at the other end; the measured thermal voltage can be correlated with the temperature at the junction, as shown in Fig. 1.7. Although any two different metals can work as a thermocouple in principle, there exist standardized thermocouple metals and alloys based on their applications and temperature measurement

range. The metal pairs of the most commonly used thermocouples and their operating temperature ranges are listed in Table 1.1.

A significant advantage of thermocouples versus other thermal measurement techniques is their relatively low cost. In addition, thermocouples are straightforward to use and can have a response frequency greater than 10MHz. To enhance the signal-to-noise ratio of a thermocouple, one can modulate the bias of an electronic or optoelectronic device to be measured and use a lock-in-amplifier to detect the component of the thermal voltage induced in the thermocouple at this bias frequency [20]. However, thermocouples also have certain disadvantages that limit their applications. Due to material impurities, the accuracy of most commercial thermocouples is typically not better than 1 K, although some can resolve 0.01 K or better. Another issue that limits the application of thermocouples in micro- or nano-scale electronics is the thermal mass of the thermocouple. The smallest commercially available microthermocouple has a tip diameter of approximately 30μm. If the sample region of interest is much smaller than the size of the thermocouple (such as a laser active region or carbon nanotube), the thermocouple itself will act as an external heat sink, and the measured temperature will be lower than the actual unperturbed temperature. A schematic of the thermal mass effect is shown in Fig. 1.8.

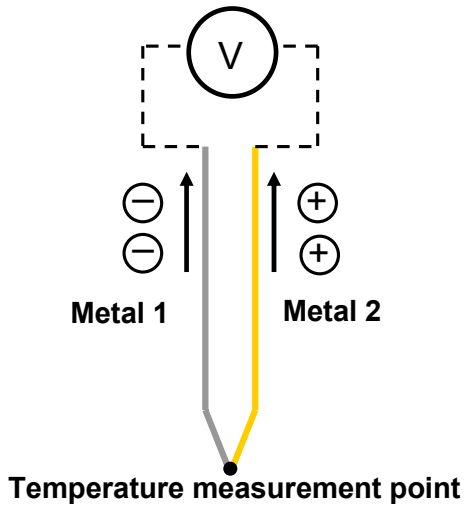

Fig. 1.7: Schematic of the working principle of a thermocouple. Metal 1 (Metal 2) is an n-type (p-type) material, and electrons (holes) diffuse from the high temperature measurement point to the low temperature reference point. The resulting thermal voltage is measured by a voltmeter.

Thermocouple type	Positive electrode (*p*-type)	Negative electrode (*n*-type)	Temperature range (^{o}C)
Type B	Pt (30%) Rh (70%)	Pt (94%) Rb (6%)	0 to 1820
Type E	Ni/Cr alloy	Cu/Ni alloy	-270 to 1000
Type J	Fe	Cu/Ni alloy	-210 to 1200
Type K	Ni/Cr alloy	Ni/Al alloy	-270 to 1372
Type N	Ni/Cr/Si alloy	Ni/Si alloy	-270 to 1260
Type R	Pt (87%) Rh (13%)	Pt	-50 to 1767
Type S	Pt (90%) Rh (10%)	Pt	-50 to 1767
Type T	Cu	Cu/Ni alloy	-270 to 400

Table 1.1: Commonly used thermocouple metal pairs and their operating temperature ranges.

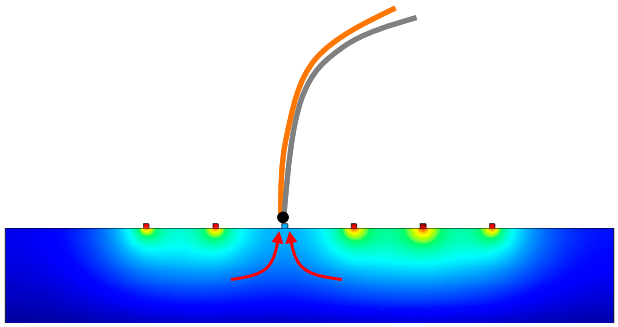

Fig. 1.8: If the thermal mass of the thermocouple is larger than the device under measurement, the thermocouple behaves as an external heat sink and cools down the device (the color map here represents a temperature scale).

1.3.2 Scanning Thermal Microscopy

Scanning Thermal Microscopy (SThM) is a scanning probe technique similar to Atomic Force Microscopy (AFM) that is designed for nanoscale temperature measurement. SThM has the highest spatial resolution of all current temperature detection approaches, with the best reported resolution being approximately 50nm [21]. The resolution is primarily limited by a water bridge which forms between the SThM probe tip and the sample [21]. Researchers have used SThM to study devices such as vertical cavity surface emitting lasers (VCSELs) [22], carbon nanotube devices [23], and diodes [24]. The fundamental working principle of SThM is very similar to thermocouple and thermistor approaches: the temperature at the contact point of the probe tip is evaluated by measuring either a thermally induced voltage in an integrated thermocouple or a change in resistance in an integrated resistor.

SThM probes based on these two ideas are shown in Fig. 1.9 [25,26]. The main drawback of using SThM to measure the temperature of nanoscale objects is again the action of the probe tip as a heat sink, which perturbs the temperature of the measured object in a similar fashion to Fig. 1.9. A further issue with SThM is the relatively expensive AFM hardware required. In addition, the applications of SThM for light emitting devices such as laser diodes or light emitting diodes are limited. Because most SThM probe tips are made of metal films (such as nickel/chromium or aluminum/chromium alloys), the light emitted from such devices will be absorbed in the probe and create heating, causing the measured temperature to be higher than the actual

device temperature. Calibration in such circumstances is theoretically possible but difficult in practice.

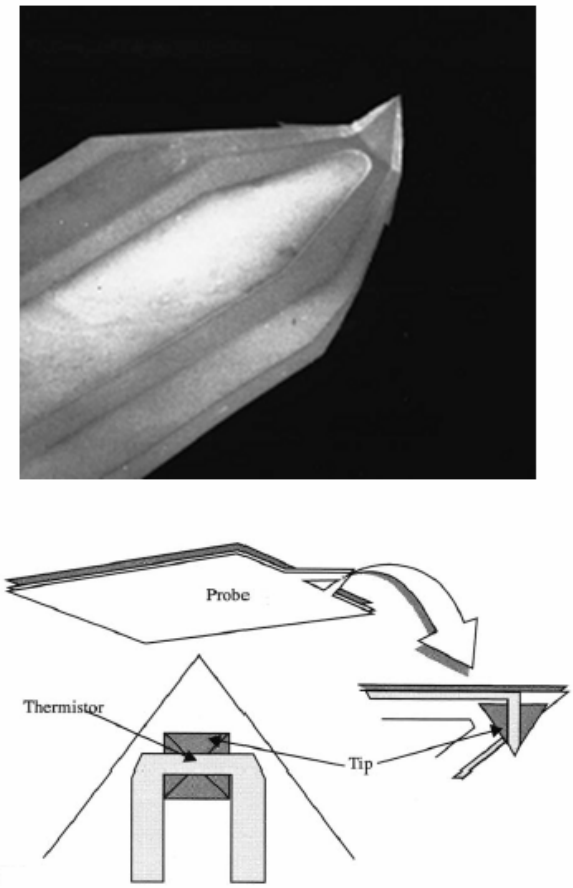

Fig. 1.9: (Top) Au/Pd thermocouple probes for scanning thermal microscopy made by electron beam lithography and silicon micromachining. (Bottom) Schematic of a thermistor-based scanning thermal probe. [25,26]

1.3.3 Infrared radiation thermometry

The working principle of the infrared radiation thermometer, which can be a single point detector or an area scanner, is to detect the infrared radiation spectrum emitted by a target and derive the target temperature using a calibration algorithm. The electromagnetic radiation intensity, *I(λ,T)*, of a blackbody is given by Planck's law:

$$I(\lambda,T)=\frac{2hc^2}{\lambda^5\left(e^{\frac{hc}{\lambda kT}}-1\right)} \tag{2.1}$$

where *h* is the Planck constant (6.626 × 10-34 J s), *k* is the Boltzmann constant (1.381 × 10-23 J K-1), *c* is the speed of light in vacuum (2.998 × 108 m s-1), *λ* is the electromagnetic radiation wavelength in meters, and *T* is the temperature in Kelvin. For a diffuse emitter that has a thermal radiation intensity independent of direction, the spectral emissive power is given by the Planck distribution:

$$E(\lambda,T)=\pi I(\lambda,T)=\frac{2\pi hc^2}{\lambda^5\left(e^{\frac{hc}{\lambda kT}}-1\right)} \tag{2.2}$$

The spectral emissive power of a blackbody as a function of temperature and wavelength is shown in Fig. 1.10. The peak emission shifts to lower wavelengths as the blackbody temperature increases. By measuring the infrared radiation intensity at a certain wavelength and correlating with Eq. 2.2, the target temperature can be derived. Modern infrared scanners allow for two-wavelength (4-5 μm and 8-9 μm) detection which can significantly enhance the signal to noise ratio [27]. Since the blackbody thermal radiation peak wavelength at room temperature is approximately 10 μm (mid-infrared regime), the

far field diffraction limit of λ/2 limits the spatial resolution to approximately 5 μm for measurement of temperatures near 300 K. This low spatial resolution is the main drawback in applying infrared radiation thermometry to electronic and optoelectronic devices, which often have characteristic lengths much less than 5 μm.

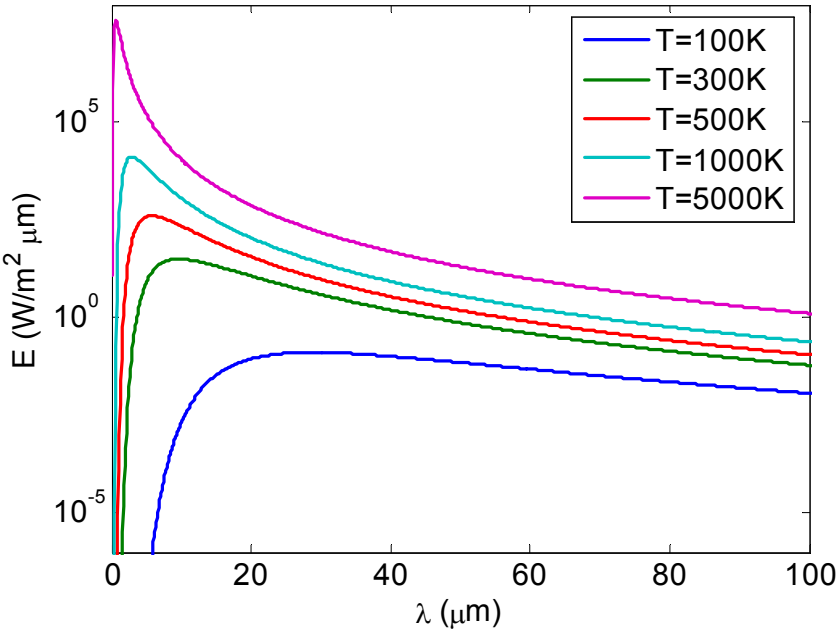

Fig. 1.10: The spectral emissive power of a blackbody at different temperatures.

1.3.4 Thermoreflectance

Thermoreflectance is the primary temperature measurement approach applied in this work. Its working principle is to detect a sample's surface temperature variation by measuring the induced change in surface reflectivity. The main advantage of this non-contact method in measuring optical devices such as laser diodes or LEDs is that the light emitted by the device can be filtered out and thus prevented from contaminating the

measurement. In addition, because the light source used to measure surface reflectivity can at a short (visible) wavelength, the technique can have higher spatial resolution due to a smaller diffraction limit than infrared radiation thermometry. The practical spatial resolution limit of thermoreflectace lies between scanning thermal microscopy and infrared thermometery, and one can modify the field of view easily by using a lower or higher magnification power objective.

1.4 Thermoelectric measurements used to characterize device-relevant material properties

In addition to providing a profile of device heating, thermal measurements can be used to derive fundamental properties of device materials. In the latter parts of this work, we will show how a measured temperature gradient applied across the channel of a pentacene-based organic thin film transistor (OTFT) can be combined with a measure of the induced thermoelectric voltage to provide a measure of the interface quality (trap density) and channel thickness.

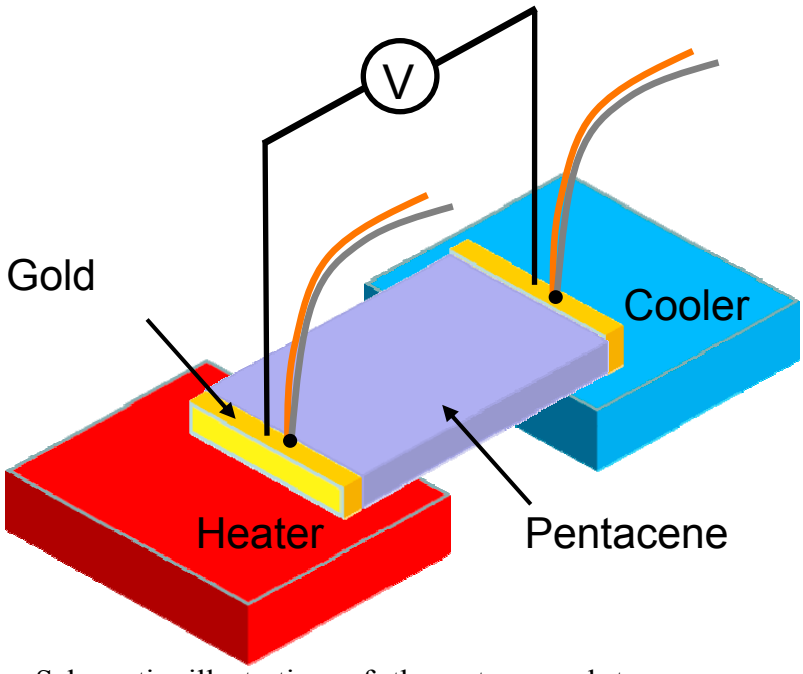

Fig. 1.11: Schematic illustration of the setup used to measure an applied temperature gradient and induced thermal voltage within a pentacene thin film.

1.5 Summary

Thermal issues represent a barrier to the future development of modern electronic and optoelectronic devices due to rapidly decreasing device size and increasing integration complexity. In order to study nanoscale heat generation and transfer experimentally, the first and the most important step is to have a temperature measurement method that is capable of quantifying temperatures accurately with submicron spatial resolution; therefore, the main objective of this thesis is to apply a high resolution two dimensional thermal imaging technique to characterize transistors and laser diodes. In the latter part of the thesis, we will discuss an application of temperature measurements to derive the interface material properties of a pentacene-based OTFT.

The outline of the remaining sections of this thesis is as follows:

In Chapter Two, the experimental technique of CCD-based thermoreflectance is introduced, first by discussing the background and previous applications of this technique and then by describing the detailed algorithm for obtaining the thermoreflectance signal from CCD images. Finally, we present the experimental setup used in the following measurements.

In Chapter Three, the fundamental working principles of heterojunction bipolar transistor (HBT) are presented, including specific problems that occur due to device self-heating. We show that high-resolution thermal imaging can differentiate the temperatures of two closely placed fingers (sub-transistors). By combining these thermal images with a thermal circuit model, we quantify the actual current carried by each sub-transistor at different bias levels and the critical bias condition at which the transistor becomes electrically asymmetric, demonstrating the potential application of this nondestructive technique for current mapping, quality control, and device reliability testing.

In Chapter Four, we present high resolution (<500nm) thermal images of a high-power edge-emitting laser diode facet. The images not only allow direct measurement of the active region temperature as a function of input current, but also can be further applied in a finite element model to simulate the refractive index change at different regions of the facet. The thermally-induced modulation of the refractive index causes optical mode size variation in an effect known as thermal lensing. We demonstrate that the simulated thermal lensing effect agrees well with direct beam measurements, and then consider the resulting change in fiber coupling efficiency.

In Chapter Five, the experimental setup is modified for a high bias frequency device, specifically a pulsed quantum dot laser. Such modification allows us to apply the thermal

imaging technique at a range of bias frequencies and duty cycles relevant to pulsed devices. We use the modified setup to measure the active region temperature and thermal relaxation time constant of the quantum dot laser, the latter being the main parameter that governs the transient temperature response of a device under an applied pulsed input current.

In Chapter Six, the Seebeck coefficient of a pentacene film deposited on silicon dioxide as part of an OTFT is measured experimentally. By knowing the Seebeck coefficient, the volumetric carrier density in the channel can be estimated. Since the areal carrier density induced by the gate insulator can also be evaluated as a function of gate voltage, we can derive the thickness of the pentacene channel. In addition, we can derive the trap density at the pentacene / silicon dioxide interface, an important material property that has a strong bearing on the performance of the device.

In Chapter Seven, a summary of the significance and impact of this work is given, and future research developments are suggested.

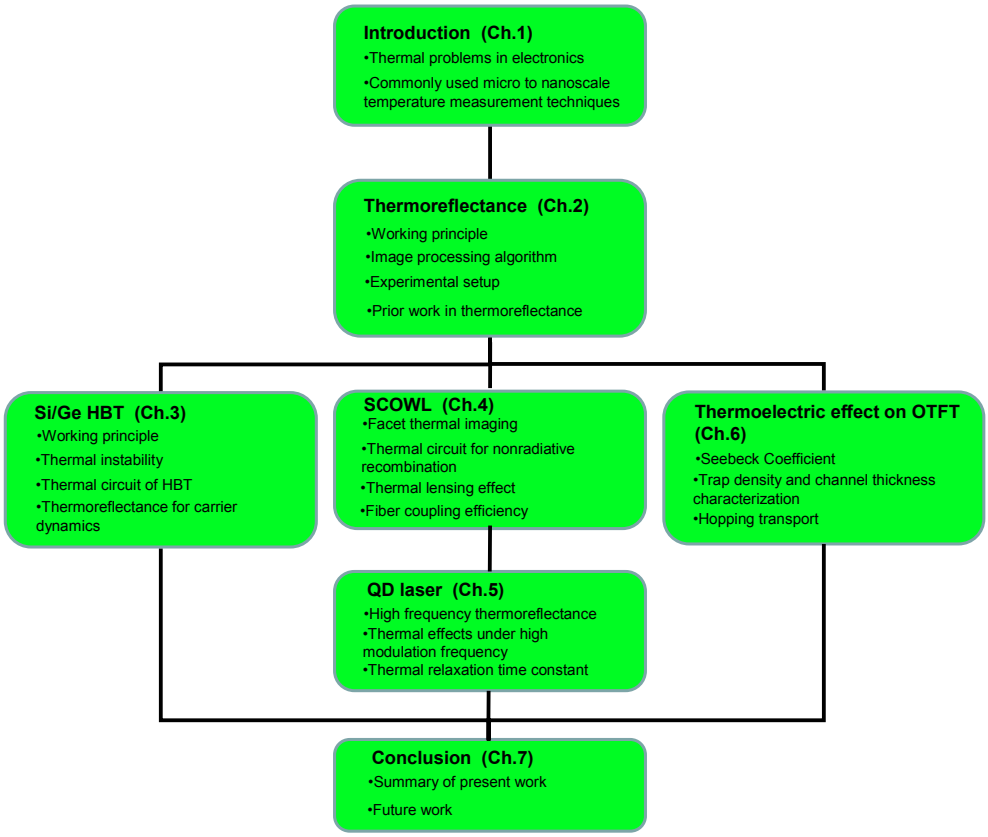

Fig. 1.12: An overview of the presented work.

Chapter 2

Thermoreflectance and microscale temperature measurement techniques

2.1 Introduction and background

Thermoreflectance is a non-contact, optical measurement technique that quantifies the temperature change of a material or device by correlating it with a temperature-induced optical reflectivity variation. In semiconductors, this variation of reflectivity is mainly due to the shrinkage of the bandgap with increasing temperature. A simple way to illustrate the effect of increasing temperature on the bandgap of a semiconductor material is to consider the thermal effect on the lattice constant. The bandgap can be considered as the energy required to break a bond and create a free electron which is the same as the energy required to excite an electron from the valence band to the conduction band in an energy band model [28]. When the temperature increases, the lattice constant increases, and the covalent bond in the semiconductor material is weakened, as a result, the energy required to break the bond drops and hence the bandgap decreases. The shrinkage of the bandgap could be due to the increase of the

valence band or the decrease of the conduction band, or both. These effects play a significant role in the current flow at a p-n heterojunction because they govern the built-in potentials that set the ratio of hole current to electron current. This ratio is a very important parameter in the operation of heterojunction bipolar transistors, as will be discussed in detail in Chapter 3. Furthermore, the scattering between electrons and phonons in the semiconductor is temperature-dependent; when the temperature of the semiconductor increases, both the electron distribution and the phonon occupation number change. This alters the electron-phonon scattering rate that is governed by the Fermi golden rule, and hence the resulting electron energies [29]. In general, the Varshni equation is typically used for an empirical fit to the decrease in bandgap with temperature [30].

The change of the refractive index (n) as a function of bandgap (E_g) in a semiconductor can be described by the Moss rule [31]:

$$n^4 E_g = constant \tag{2.3}$$

For light at normal incidence, assuming no absorption, the reflectivity can be written as

$$R = \frac{(n-1)^2}{(n+1)^2} \tag{2.4}$$

From Eqs. 2.3 and 2.4, it is apparent that as the band gap of the material varies due to heating, the reflectivity changes; this is the fundamental working principle of thermoreflectance.

Thermoreflectance has been successfully applied to study a variety of thermal phenomena in electronic devices and semiconductor materials. One can classify thermoreflectance techniques into two main groups: i) DC or quasi-steady

thermoreflectance and ii) transient thermoreflectance. In DC or quasi-steady state thermoreflectance, the detector is often a CCD camera; since the frames per second (fps) rate of the CCD camera must be quite low (~100 Hz) to practically achieve the bit depth required to measure small changes in brightness (12 bits), the CCD cannot be used to detect a high modulation frequency signal (>100Hz). However, since the CCD pixel array can image signals in parallel from a large field of view (rather than scanning a single point measurement across a surface), it is very useful for generating 2D profiles of temperature. Lüerßen *et al*. have applied this technique to profile the temperature profile of a vertical cavity surface emitting laser (VCSEL) [32] (Fig. 2.1) and have also demonstrated CCD-based thermoreflectance with temperature resolution of 10mK and spatial resolution of 250nm [33]. Tessier *et al.* have used ultraviolet illumination thermoreflectance on an integrated circuit [34]. Epperlein first performed thermoreflectance on a laser diode facet to study catastrophic optical damage (COD) and degradation processes [35]. Mayer *et al*. performed thermoreflectance to measure the Peltier heating/cooling and Joule heating of a polycrystalline Bi_2Te_3 thermoelectric element [36].

Transient thermoreflectance is often performed as a pump-probe technique with a picosecond pulsed source and a fast detector, and is typically a single-point measurement due to the limitations of CCD frame rates and the difficulties of scanning at high speed. It is commonly used to characterize material thermophysical properties such as thermal conductivity [37], thermal diffusivity [38], electron – phonon coupling [39] (Fig. 2.2), and thermal boundary resistance [40].

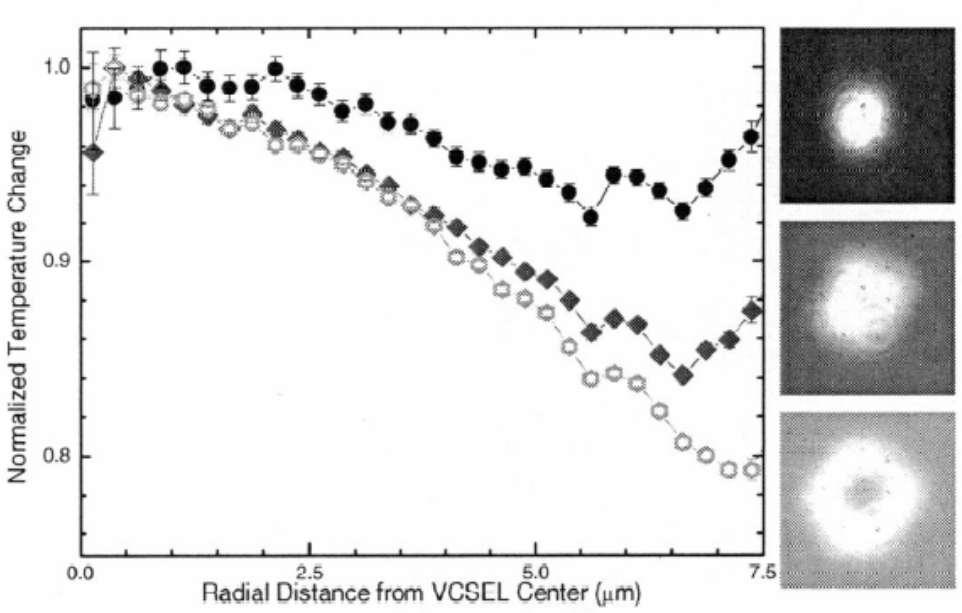

Fig. 2.1: (Left) Normalized radial temperature profile of a VCSEL at different lasing modes. (Right) Optical mode profiles of the VCSEL at different bias levels [32].

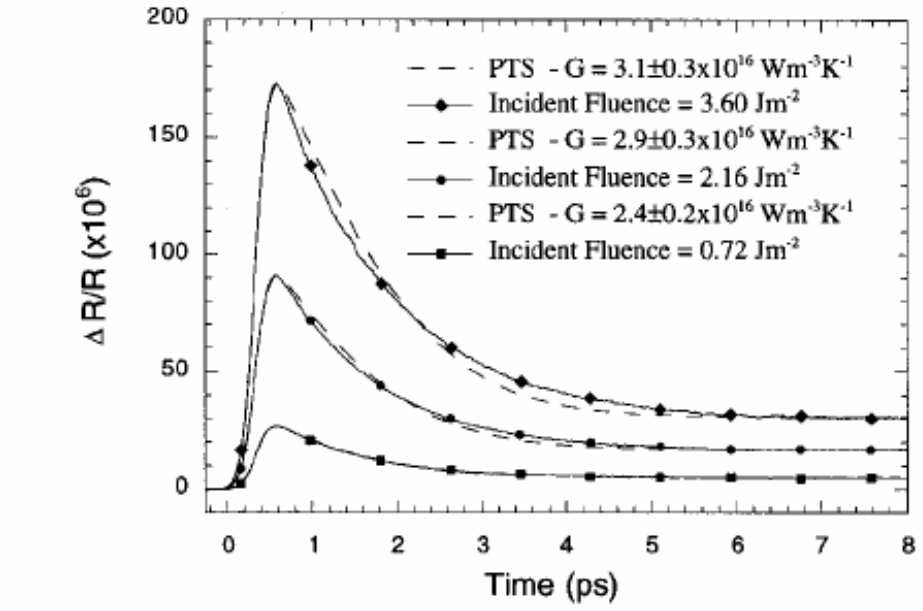

Fig. 2.2: Transient thermoreflectance response of a 23 nm Au film. G is the electron-phonon coupling factor [39].

2.2 Error due to carrier density induced index change

The refractive index and hence the reflectivity of a material surface can be varied mainly by changes in temperature and carrier density. In semiconductors, these two contributions have opposite effects on the refractive index of the material: $\frac{dn}{dT}$ is positive and $\frac{dn}{dN}$ is negative [41,42]. In the active region of a bipolar device such as a laser in which carrier injection leads to a large change in carrier density, the latter effect can be comparable to the thermal effect, leading to measurement error. For GaAs, a change of carrier density from 10^{15} to 10^{18} cm^{-3} (typical for a laser active region at zero bias vs. above threshold), will induce a refractive index variation of -0.02 [43]. The relation between the reflectivity and the refractive index is given by

$$\Delta R = \frac{4(n-1)}{(n+1)^3}\Delta n \tag{2.5}$$

which when combined with Eq. (2.4) yields a ΔR/R of -0.008. For comparison, the ΔR/R caused by a 10K temperature variation in GaAs at the illumination wavelength of our setup is only approximately 0.002. Such carrier-induced reflectivity variation will therefore certainly cause error in the temperature measurement. However, since for a laser the carrier density variation mainly occurs in the active region (i.e. the quantum wells), the measurement error has a spatial extent which is much smaller than the resolution of the instrument and only located in a small region of the device. Therefore, spatial averaging on the active region pixels will partially compensate for this error, as discussed in Section 4.5. Furthermore, experiments in which the laser is kept above

threshold will have much reduced carrier density induced error due to the clamping of active region carrier density above threshold.

2.3 Thermoreflectance equation

Since the temperature-induced reflectivity variation has a complicated relationship with band structure that is very material dependent, the relationship between change in temperature ΔT and change in reflectivity ΔR is usually approximated to be linear over small ranges of ΔT and given by the thermoreflectance equation,

$$\Delta T = \kappa^{-1} \frac{\Delta R}{R} \tag{2.6}$$

where $\Delta R/R$ is the normalized variation in reflectivity (thermoreflectance signal) and κ^{-1} is a proportionality constant known as the thermoreflectance coefficient. The value of the thermoreflectance coefficient is material and illuminating wavelength dependent, with typical values ranging between 10^{-3} and 10^{-6}.

2.4 Detection of thermoreflectance signal (ΔR/R)

In the following section, the algorithm for calculating the thermoreflectance signal *(ΔR/R)* based on the approach suggested by Grauby S. et al. [44] and Fournier D. et al. [45] will be described. The bias signal sent to the device (blue), the frame trigger signal sent to the camera (green), and the reflectance signal captured by the camera (red) are shown in Fig. 2.3. The bias signal sent to the device is in the form of an applied sinusoidal current with frequency f_1. The CCD camera is triggered to begin integrating at each detector pixel on each falling edge of the frame trigger signal. Note that the frame trigger signal is phase locked to the device bias signal at a frequency $4f_1$; i.e. four pictures are taken by the CCD camera during each cycle of device bias. The light emitting diode (LED) used for illumination is operated at constant input power, making the optical flux Φ a constant.

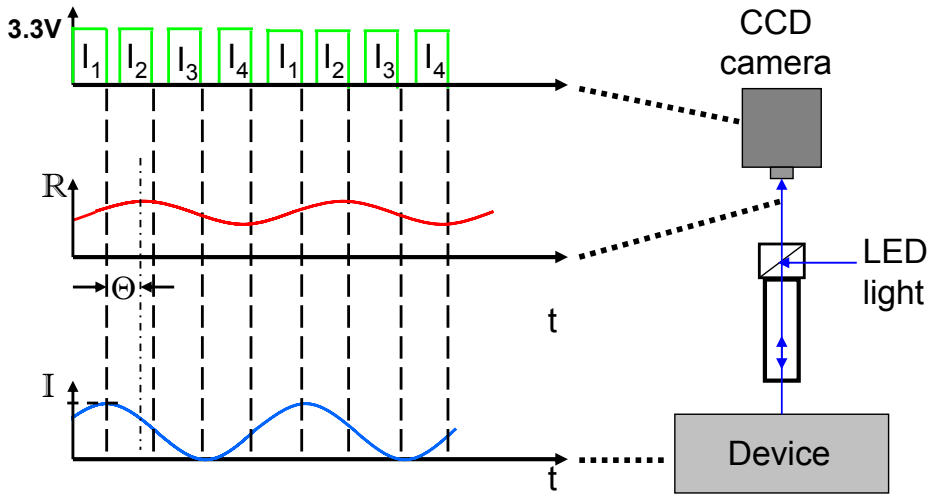

Fig. 2.3: Schematic of the bias signal sent to the device (blue), external frame trigger signal sent to the CCD camera (green), and reflectance signal captured by the CCD camera (red).

The device surface reflectivity variation due to device heating that is captured by the CCD camera will be a sinusoidal wave with frequency f_1, although there may be a phase difference (Θ) at each detector pixel between the device bias signal and the reflectivity signal due to the thermal relaxation time constant. This time constant is dependent on the thermal conductivity, density, and specific heat capacity of the materials.

The reflectivity of the device surface can be written as

$$R = R_0(x,y,t) + \Delta R(x,y,t)\cos(2\pi f_1 t + \Theta(x,y)) \tag{2.7}$$

where R_0 - ΔR is the reflectivity when the device is off (current = 0) and R + ΔR is the reflectivity when the device is on (current = I). Multiplying the optical flux from the LED with the reflectivity of the device surface, the signal seen by the CCD camera (S) can be written as

$$S(x,y,t) = \Phi R_0(x,y,t) + \Phi\Delta R(x,y,t)\cos(2\pi f_1 t + \Theta(x,y)) \tag{2.8}$$

The thermoreflectance signal (ΔR/R) is then evaluated as a function of the four images captured by the CCD camera during each bias cycle, each picture being integrated over approximately one quarter of the bias period T:

$$I_1 = \int_0^{T/4} S(x,y,t)dt = \Phi R_0\left(\frac{T}{4}\right) - \frac{\Phi\Delta R}{2\pi f_1}\cos(2\pi f_1 \frac{T}{4} + \Theta) + \frac{\Phi\Delta R}{2\pi f_1}\cos(\Theta) \tag{2.9}$$

$$I_2 = \int_{T/4}^{T/2} S(x,y,t)dt = \Phi R_0\left(\frac{T}{2}\right) - \frac{\Phi\Delta R}{2\pi f_1}\cos(2\pi f_1 \frac{T}{2} + \Theta) - \Phi R_0\left(\frac{T}{4}\right) + \frac{\Phi\Delta R}{2\pi f_1}\cos(2\pi f_1 \frac{T}{4} + \Theta) \tag{2.10}$$

$$I_3 = \int_{T/2}^{3T/4} S(x,y,t)dt = \Phi R_0\left(\frac{3T}{4}\right) - \frac{\Phi\Delta R}{2\pi f_1}\cos(2\pi f_1 \frac{3T}{4} + \Theta) - \Phi R_0\left(\frac{T}{2}\right) + \frac{\Phi\Delta R}{2\pi f_1}\cos(2\pi f_1 \frac{T}{2} + \Theta) \tag{2.11}$$

$$I_4 = \int_{3T/4}^{T} S(x,y,t)dt = \Phi R_0\left(T\right) - \frac{\Phi\Delta R}{2\pi f_1}\cos(2\pi f_1 T + \Theta) - \Phi R_0\left(\frac{3T}{4}\right) + \frac{\Phi\Delta R}{2\pi f_1}\cos(2\pi f_1 \frac{3T}{4} + \Theta) \tag{2.12}$$

By combining Eqs. 2.9 to 2.12, the temperature difference between the device on and off states can be written as

$$\Delta T = \kappa^{-1}\frac{2\Delta R}{R - \Delta R} \approx \kappa^{-1}\frac{2\Delta R}{R} = \sqrt{2}\pi\frac{\sqrt{(I_1 - I_3)^2 + (I_2 - I_4)^2}}{I_1 + I_2 + I_3 + I_4} \tag{2.13}$$

with the phase difference Θ between the device bias and reflectance signals given by

$$\tan(\Theta) = \frac{I_1 + I_2 - I_3 - I_4}{I_1 - I_2 - I_3 + I_4} \tag{2.14}$$

During the experiment, there will be a certain amount of readout noise in the CCD camera which will cause uncertainty and error. An effective approach to enhance the signal-to-noise ratio is to average over a large number of device bias cycles, a software-based method analogous to hardware-based lock-in amplification methods. As shown in Fig. 2.9 the value of I_1 used in Eqs. 2.13 and 2.14 is obtained by cumulative averaging of a number of I_1 images taken over many device bias cycles; the same holds for I_2, I_3, and I_4. The LabVIEW program used for this averaging was based on a program originally developed by Dr. Dietrich Lüerßen at the Massachusetts Institute of Technology. In addition to the number of averaged images, the uncertainty of the signal is also affected by any change in the brightness of the LED light (i.e. the readout counts

of the CCD camera). Fig. 2.4 shows the uncertainty signal, which is defined as the standard deviation of ΔR divided by the counts, for the 12-bit Opteon CCD camera used in this experiment. The counts variable quantifies the strength of the signal received by the CCD camera. For a 12 bit camera, the maximum count is $2^{12} = 4096$.

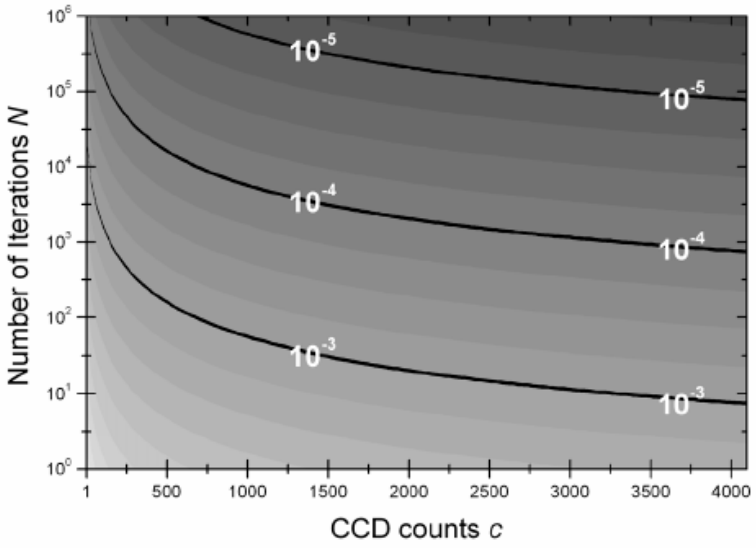

Fig. 2.4: The uncertainty (standand deviation of ΔR/count) of the Opteon 12-bit CCD camera as a function of counts and number of iterations [33].

2.5 Measurement setup

The CCD-based thermoreflectance setup used here is built around a far field optical microscope as shown in Fig. 2.5. The microscope used is a Mitutoyo FS-70 equipped with 10x, 50x and 100x super long working distance objectives (M Plan Apo SL Series). The long working distance objectives are extremely important for most of the semiconductor device measurements (described in later chapters) in order to leave room for device bias probes. A 12-bit CCD camera (Opteon) is C-mounted on the microscope for image capture. The CCD camera is connected by Ethernet cable to a workstation computer equipped with an NxN PCI-X card. The PCI-X card runs at 66MHz, 64 bits for fast data transfer. For illumination, a high power LED (16 lumen Luxeon Star/O) emitting at 470nm with FWHM of approximately 50nm is used. An external rectangular fin heat sink and a 50mm fan are used to cool down the LED and prevent optical flux variation due to heating, which can contaminate the thermoreflectance signal. The device under study sits on a copper block stage, under which lies a feedback-controlled thermoelectric cooler (Newport 3040 Temperature Controller). The maximum amount of heat load on the cold side of the thermoelectric cooler is approximately 20W (Melcor, Inc).

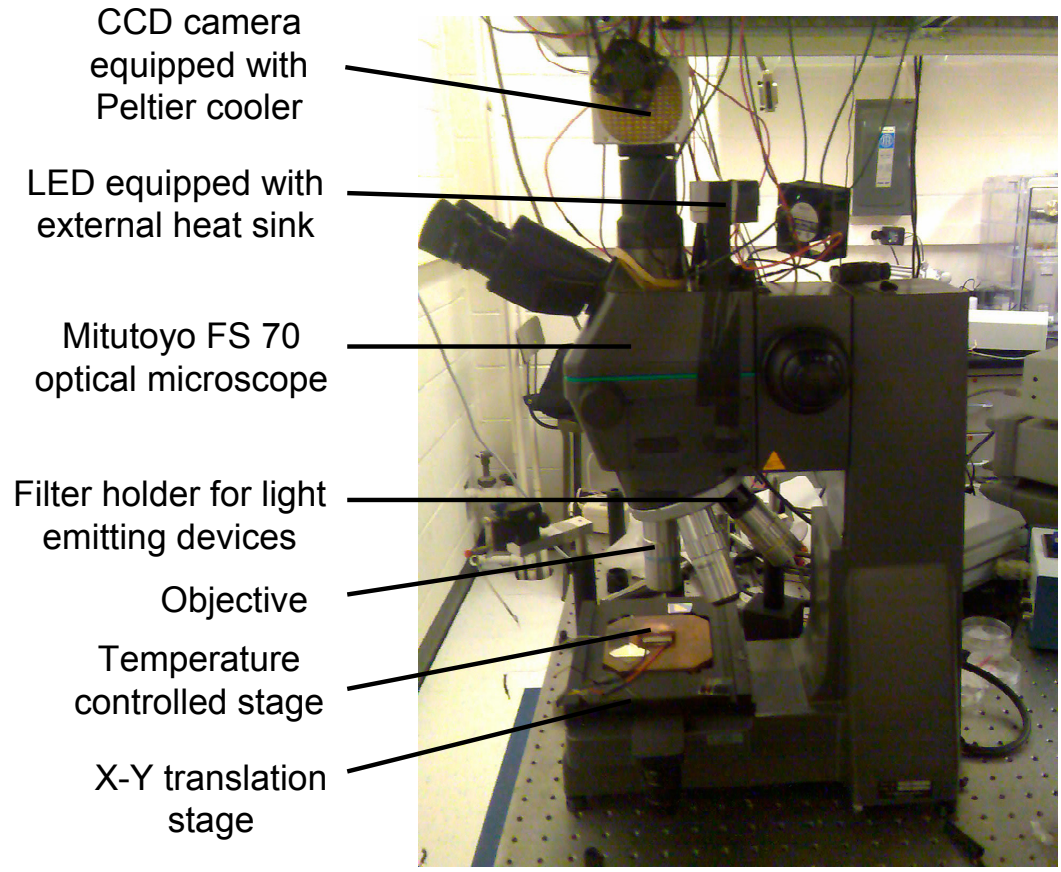

Fig. 2.5: CCD-based thermoreflectance experiment setup.

2.6 Calibration of the thermoreflectance coefficient (κ)

As discussed in Section 2.5, the working principle of thermoreflectance is based on the thermoreflectance equation (Eq. 2.6). In addition to the thermoreflectance signal $\Delta R/R$ obtained by cumulative averaging of CCD images, the thermoreflectance coefficient (κ) is required in order to calculate the temperature profile of the device. Since the thermoreflectance coefficient is dependent on both device material and illuminating wavelength, it should be measured *in-situ*.

There are two approaches to calibrate the thermoreflectance coefficient. In the first method, a microthermocouple (~30μm measurement area) is placed on top of the device during a thermoreflectance experiment. The directly measured temperature variation (ΔT) is then compared with the thermoreflectance signal $\Delta R/R$ in the region near the thermocouple. The main advantages of this approach are its relative ease and short experiment time; however, the most significant drawback is that this approach cannot be used to calibrate materials with surface area smaller than the thermocouple (such as most layers within an electronic device). We therefore in most cases prefer the second calibration method. For this technique, a 0.5 Hz sinusoid generated by a function generator (Agilent 33120A) is applied as an input to a high-voltage, high-current dual operational amplifier (Texas Instruments OPA2544). The output of the operational amplifier is connected to the Peltier cooler stage that sits under the device. Peak-to-peak temperature variation amplitude of 1.5 K in the device can be achieved by this method. By triggering the CCD camera at 2Hz to obtain the thermoreflectance image, the thermoreflectance coefficients of the different device layers (all of which are experiencing nearly the same ΔT as measured by a thermocouple on the device surface) can then be directly obtained by taking a ratio of $\Delta R/R$ and 1.5 K at each location on the device. The measured thermoreflectance coefficients of several common electronic and optoelectronic device materials of interest for the present work are shown in Table 2.1.

Material (illuminating wavelength)	$\kappa(K^{-1})$
Gold (470nm)	6.2×10^{-4}
Silicon (470nm)	1.2×10^{-4}
GaAs (470nm)	1.9×10^{-4}
InP (470nm)	2.2×10^{-4}

Table 2.1 Thermoreflectance coefficients of different semiconductor materials used in this work.

2.7 Summary

In this chapter, several commonly used micro- to nano-scale temperature measurement techniques are introduced. We can mainly divide these techniques into two categories: contact measurement and non-contact measurement. For contact measurement techniques, the working principles primarily rely on thermally induced voltage (thermocouple) or thermally induced resistance variation (thermistor). Non-contact measurement techniques are usually performed optically and include infrared radiation thermometry and thermoreflectance. The present work is focused on CCD-based thermoreflectance and its application to electronic and optoelectronic devices. In Section 2.5.2, we introduced the thermoreflectance equation and showed how the thermoreflectance signal ($\Delta R/R$) can be determined as a function of four reflectance images taken by a CCD camera during a device bias cycle. We also discussed the detailed

experiment setup and the calibration procedure for obtaining the thermoreflectance coefficient.

Chapter 3

Profiling carrier dynamics in a high power heterojunction bipolar transistor (HBT) by CCD-based thermoreflectance

3.1 Introduction

Transistors are commonly used semiconductor devices that can be found in a variety of electronics, such as cell phones, computer CPUs, and displays. In general, they may be divided into two categories: 1) Field Effect Transistors (FETs) and 2) Bipolar Junction Transistors (BJTs). In a FET, a carrier channel is formed between a dielectric material and a semiconductor by applying voltage at the gate contact. The current flowing through the channel is controlled by voltage applied between the drain and source. On the other hand, a BJT does not rely on a channel but instead is composed of two *p*-*n* junctions in series that share the same base region; the bias on this base region controls current between the collector and emitter.

A cross-sectional view of an *npn* bipolar junction transistor is shown in Fig. 3.1 [46]. Current flow in an *npn* BJT is due to the movement of injected electron from the

emitter through the base to the collector. The arrows in Fig. 3.1 indicate the current directions (note that the direction of current flow is defined to be opposite that of electron flow). The current paths and band diagrams for the BJT under both zero bias and active mode bias (i.e. forward bias at the base-emitter junction and reverse bias at the collector-emitter junction) are shown in Fig 3.2 [46] The n^+ regions in the emitter and collector are sufficiently highly doped that the Fermi level can be assumed to be located at the conduction band edge. When the device is under zero bias (equilibrium), the Fermi level is flat throughout the device as shown in Fig, 3.2, and no net current flows. When the device is under active bias, the applied forward bias at the base-emitter junction decreases the built-in potential barrier and causes electron injection from the emitter to the base and hole injection from the base to the emitter. While the base-emitter junction is under forward bias, the base-collector junction is under reverse bias; as a result, most of the electrons injected from the emitter are collected by the collector and contribute to the collector current (although some electrons recombine with the holes in the base region).

In order to quantify the performance of the BJT in the common emitter configuration (i.e. the emitter grounded and the base and collector under positive bias), we typically consider the current gain (β) which defines the current amplification power of the HBT:

$$\beta = \frac{I_{collector}}{I_{base}} \tag{3.1}$$

For most HBTs, β has a value on the order of 100.

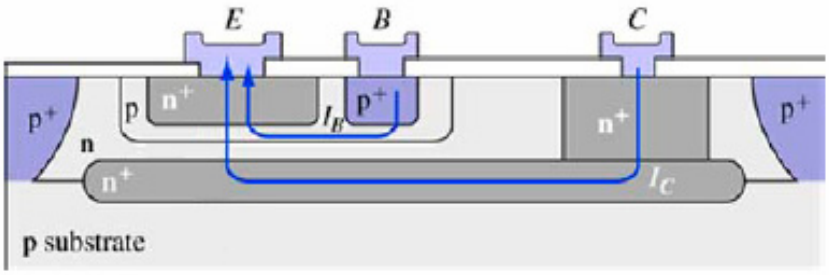

Fig. 3.1. Cross-sectional view of an *npn* bipolar junction transistor. E, B, C represent the contact pads for emitter, base, and collector respectively. The arrows represent the direction of current. [46]

In the rest of chapter, we will focus on a particular kind of bipolar transistor known as the heterojunction bipolar transistor (HBT). The primary feature of the HBT is that the base and collector materials are different from the emitter materials; i.e. a heterojunction is made intentionally between the emitter and the base. By appropriately choosing these materials, the potential barrier seen by electrons flowing from the emitter to the base can be made to be lower than that seen by the holes flowing from the base to the emitter, resulting in lower power consumption and increased injection efficiency. In addition, the base semiconductor material of an HBT is usually heavily doped, allowing high electron mobility without compromising the gain; hence the HBT can operate at higher frequencies than a homojunction BJT for the same gain (a heavy doped base will strongly degrade the gain of a homojunction BJT [47]).

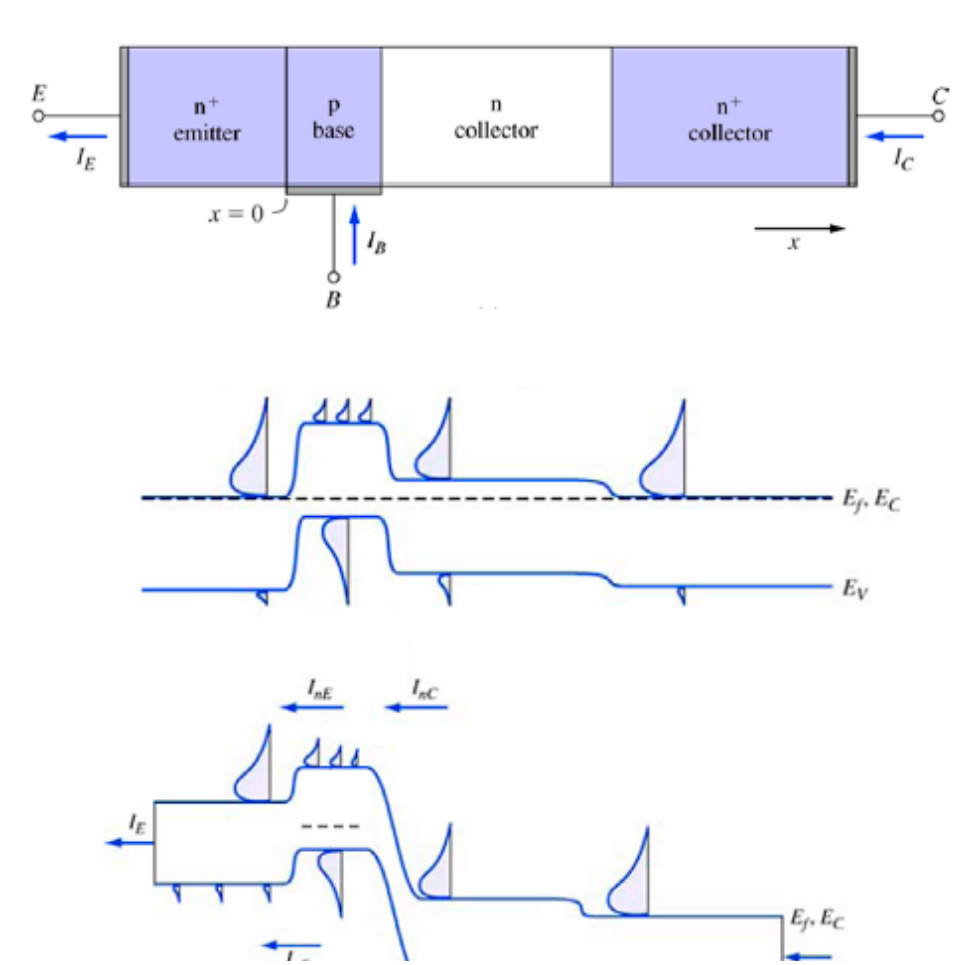

Fig. 3.2. (Top) Current paths for the bipolar junction transistor when biased in active mode. (Middle) Band diagram of the BJT under zero bias (equilibrium condition). (Bottom) Band diagram of the BJT under an active mode bias in a common emitter configuration with the base-emitter junction under forward bias and the collector-emitter junction under reverse bias. [46]

3.2 Qualitative analysis of thermal instability in HBTs

The performance of a heterojunction bipolar transistor (or any BJT) is very sensitive to the operating temperature of the device. Heating of the HBT causes variation in current gain (β) and output collector current [47,48,49]. Such change in current gain can be illustrated by a band diagram (Fig. 3.3). The injection efficiency (γ) is given by

$$\gamma = \frac{I_{nE}}{I_{nE} + I_{pE}} \tag{3.2}$$

where I_{nE} is the electron current injected from the emitter to the base and I_{pE} is the hole current injected from the base to the emitter as shown in Fig. (3.3). For an HBT, only I_{nE} contributes to the collector current (output current). A significant advantage of the HBT over the homojunction BJT is that the potential barrier for electrons is smaller than the potential barrier for holes, leading to an HBT injection efficiency that is close to unity. However, when the HBT is heated up, the bandgaps of the materials become smaller, and hence the potential barriers for both electrons and holes decrease. Depending on whether the conduction band offset (ΔE_c) or valence band offset (ΔE_v) between the emitter and the base has a larger drop, more electrons or holes can surmount the base-emitter junction [Fig. 3.3]. Furthermore, the carrier distributions extend to higher energy when temperature increases, leading to more flow over the barriers. Depending on the relative changes of ΔE_C and ΔE_V, increase or decrease of the injection efficiency can occur.

This change in injection efficiency with temperature is particularly relevant to multifinger HBTs. As shown in Fig. 3.4, one can consider a multifinger HBT as having a number of individual transistors in which the emitters, bases, and collectors are connected

in parallel. The measured collector current (I_C) as a function of base current (I_B) is therefore the sum of the individual transistor collector currents.

For simplicity, let us consider the case of a two-finger HBT. If a constant current bias is applied between the emitter and the base, and if one finger has a slightly higher temperature than the other due to intrinsic defects or processing variability, the potential barrier at its base-emitter junction decreases and its base current increases, causing further heating. As shown in Fig. 3.3 (middle and bottom), this increase of the base current can be due to two factors which depend on the properties of the constituent materials: 1) more electrons are injected from the emitter into the base, or 2) more holes are injected from the base into the emitter. Since the base-emitter junction is biased by a constant current source, the total base current of the two-finger device is fixed: if one finger carries more current, the other finger has to transmit less current. Eventually, the hot finger carries all of the current, and the cool finger becomes inactive; this phenomenon is known as current hogging and becomes more serious as the base-emitter bias current increases. When current hogging occurs in an HBT, the total collector current of the HBT will be changed. If the conduction band offset (ΔE_c) between the emitter and collector drops more than the valence band offset (ΔE_v), more electrons are injected from the emitter to the base, the injection efficiency (γ) and the current gain (β) both increase, and hence the total output collector current increases for a given V_{CE}. On the other hand, if ΔE_v drops more than ΔE_c when temperature increases, more holes are injected from the base to the emitter when the base current increases. As a result, the injection efficiency, current gain, and collector current all decrease. The relative magnitudes. of the ΔE_c and ΔE_v drops as a function of temperature are material dependent.

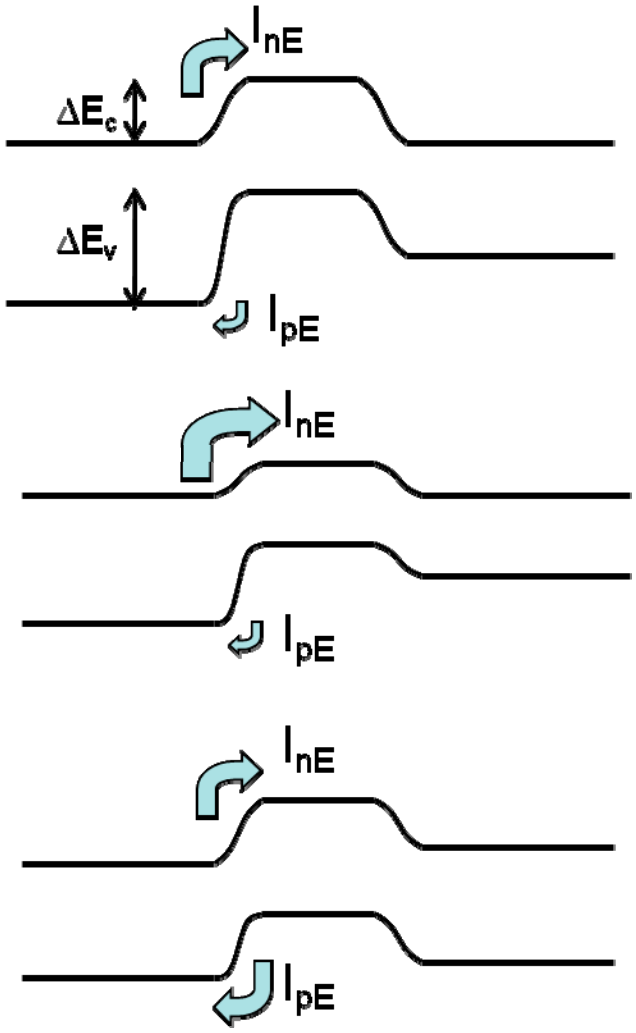

Fig. 3.3: (Top) Band diagram of a heterojunction bipolar transistor under normal operation without heating. (Middle) Increase or (Bottom) decrease of injection efficiency due to heating, depending on the relative decrease in ΔE_C vs. ΔE_V.

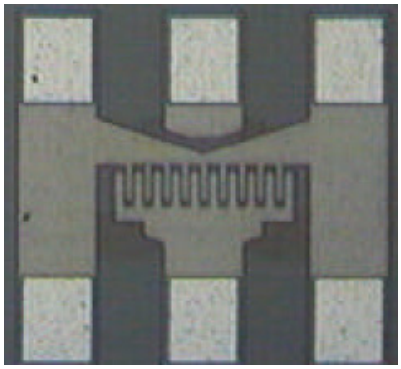

Fig. 3.4: Optical image of a multifinger heterojunction bipolar transistor with a total of nine emitter fingers.

For InGaAs/InGaAsP HBT, the temperature increase causes positive feedback on the current gain as shown in Fig. 3.5 [51]. On the other hand, for GaAsP/GaAs [52], SiGe [53], and AlGaAs/GaAs HBTs [48], the temperature increase causes negative feedback on the current gain as shown in Fig. 3.6. In Fig. 3.6, the drop of the collector current can be divided into two regions, the negative differential resistance (NDR) region and the collapse region. In the NDR, the temperatures of both fingers increase gradually with V_{CE} without current hogging, and the total collector current drops linearly. As the applied collector-emitter voltage continues to increase, one particular finger significantly heats up due to intrinsic defects and carries most of the current, the other finger becoming inactive. This marks the transition from the NDR region to collapse region. The combined effect of this current hogging and the decrease of injection efficiency upon increasing temperature is that the total collector current of the HBT drops dramatically in a phenomenon known as current collapse.

For some applications, the base-emitter of an HBT is biased by voltage source rather than a current source. The fundamental difference between constant voltage bias and constant current bias is that for the former the base current (I_B) is not a constant and can increase significantly when the device heats up.

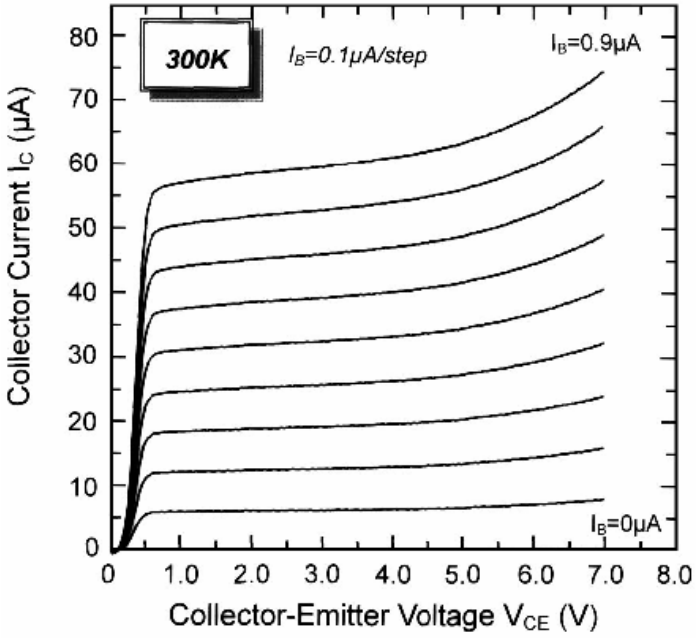

Fig. 3.5: The collector current of an InGaAs/InGaAsP HBT as a function of base current and collector-emitter voltage. [51]

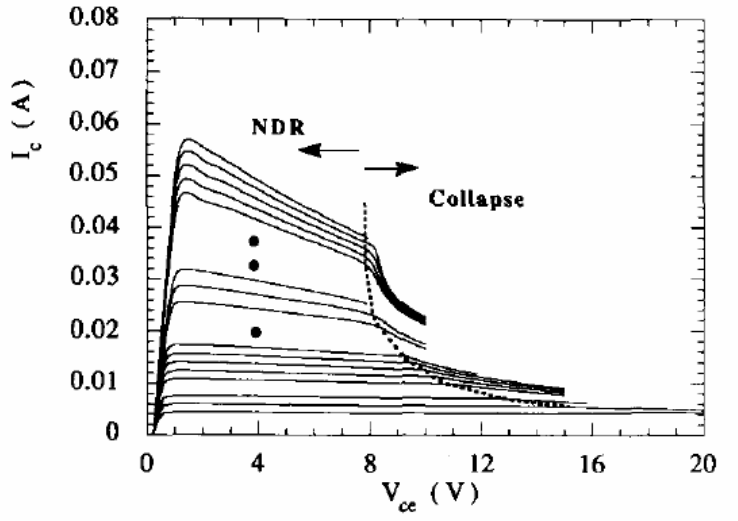

Fig. 3.6: The collector current of an AlGaAs HBT as a function of collector-emitter bias and base current. Two separate region of collector current decrease can be observed. [50]

When the total base-emitter voltage keeps on increasing, the probe resistance in the base lead will become important and it will cause significant amount of voltage drop across that series resistance [54]. To illustrate this idea, a simplified circuit which considers the transistors as resistors shown in Fig. 3.7. When the HBT is under low bias, thermal effects are not significant and both fingers carry the same current I_c. However, when a larger V_{BE} bias is applied, the total current of the HBT increases and one finger may become slightly hotter than the other due to intrinsic material defects or processing variability. In the hotter finger, the resistance decreases and allows more and more current flow. Since the parallel base-emitter resistance for both fingers decreases, more voltage is dropped across the series resistance (R_S) and less across the base-emitter fingers ($V_{BE} > V'_{BE}$ in Fig. 3.7). The current flowing in the colder finger therefore decreases. Fig. 3.8 shows the total collector current of a multifinger HBT bias under

constant voltage across base and emitter. It can be seen that the total collector current increases up to a point and then is clamped. This clamping is due to the fact that the increase of current in the hotter finger is cancelled out by the decrease of current in the colder finger. At that critical bias point, the two fingers of the HBT start to carry different currents as shown from the experimental results in Fig. 3.9 [54]. The dotted line is the measured collector current of the hotter finger, and the solid line is the measured collector current of the colder finger. The electrical isolation of the two fingers is accomplished by ion implantation, as discussed in the next section.

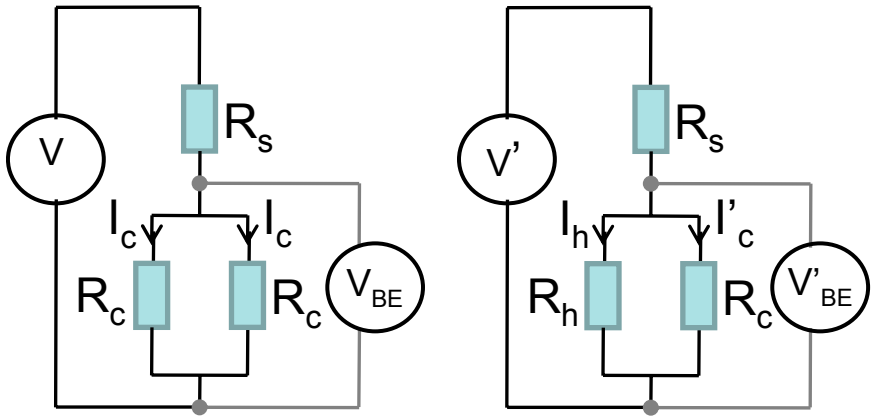

Fig. 3.7: (Left) The simplified circuit represents the normal operation of a two finger transistor. (Right) The circuit represents the same transistor under current hogging when the voltage increases. I_h is the current passing through the hot finger and I_c is the current passing through the cold finger. Under current hogging, I_h is larger than I_c and I'_c is smaller than I_c.

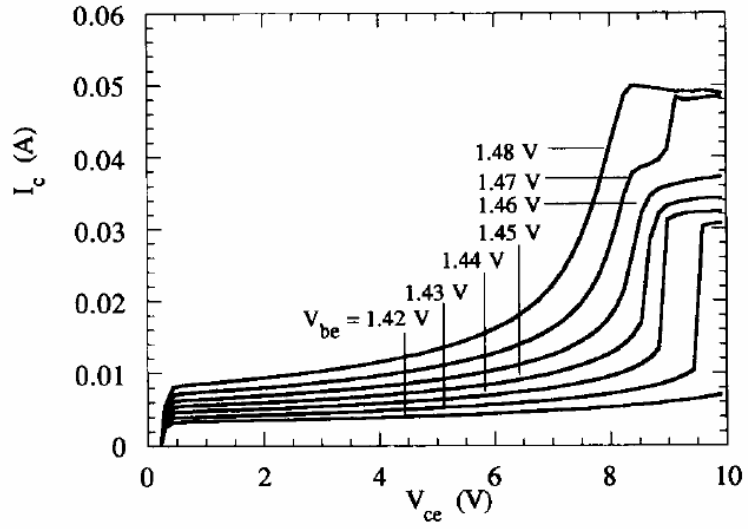

Fig. 3.8: Total collector current of an HBT biased by a constant voltage source across its base-emitter junction. [54]

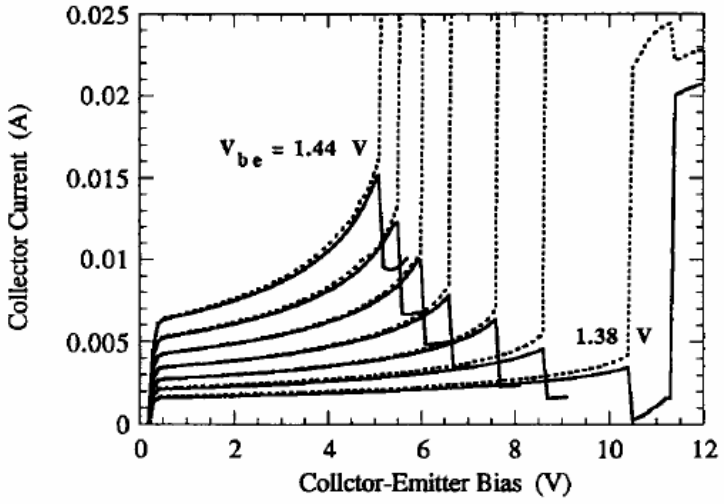

Fig. 3.9: Individual collector currents of a 2-finger HBT biased under constant V_{BE}. The dotted line is the collector current of the hot finger, and the solid line is the collector current of the cold finger, isolated by means of ion implantation [54].

3.3 Prior simulation and experimental work on temperature and current mapping of HBTs

Analytical models have been developed to examine the critical bias conditions that cause current collapse and thermal runaway. In addition, circuit designs incorporating emitter and base ballast resistors have been used to stabilize device performance by achieving a zero feedback loop gain on the total collector current [55]. Further models have been used to study current crowding and simulate the current in each emitter finger; these models suggest that the current density in one finger of a multi-finger HBT under high bias can be as high as four times that of the other fingers. Such an uneven distribution of current density can lead to thermal breakdown of the device [56]. Prior work on directly measuring the collector current in each finger has used ion implantation to electrically isolate the fingers from each other [54]. Separate collector contacts are then used for the different fingers to allow individual current measurement. However, this method is impractical for highly integrated circuits and also requires significant extra fabrication steps for the ion implantation process. In addition, the ion-implanted structures can deviate in performance from the original structures. As a result, a simple and non-destructive approach is needed to measure the current carried by each finger independently and without device modification.

The technique employed here is to measure the temperatures of the fingers and consequently generate a map of current density, providing understanding of the current collapse phenomenon and the critical bias condition at which current hogging between fingers occur. In prior work, micro-Raman spectroscopy has been applied to obtain a 2D temperature map with 10 K resolution of a multi-fingered AlGaN/GaN heterostructure

field-effect transistor, in order to study how device defects affect self-heating [57,58]. However, the temperature resolution of micro-Raman spectroscopy is not sufficient to allow derivation of current density in separate fingers. Here we instead apply CCD-based thermoreflectance, which has both high spatial resolution and high temperature resolution, to study current hogging in a multifinger HBT.

3.4 Thermoreflectance imaging of a SiGe HBT

To demonstrate the use of CCD-based thermoreflectance for imaging current dynamics in a multifinger HBT, we consider a two-finger SiGe HBT (provided by Prof. Zhenqiang Ma at University of Wisconsin-Madison and Jazz Semiconductor) as shown in Fig. 3.10. No ballast resistors are connected to any of the emitter fingers. The HBT is placed on a Peltier heat sink with a feedback-controlled temperature of 20 ^{o}C, and is biased in a common-emitter configuration with the collector-emitter voltage (V_{CE}) varied from 1V to 5V. The heat generated in each finger is therefore given by $I_C \times V_{CE}$. Using the calibration procedure described in Section 2.5, we determine the thermoreflectance coefficient of the device metal alloy contact surface to be 8.2×10^{-4} K^{-1}. In what follows, we primarily discuss $\Delta R/$R profiles and often do not convert to temperature, since we will at all times only be comparing contact regions that have the same thermoreflectance coefficient κ.

Thermoreflectance images of the device at different bias points are shown in Fig. 3.11. These images were taken while modulating the base-emitter voltage (V_{BE}) with a square-wave signal of amplitude 1.52V and frequency 10Hz, varying the collector-

emitter bias (V_{CE}) from 1V to 5V under DC mode, and operating the CCD camera at 40Hz. The approach to obtain the thermoreflectance signal was discussed in Chapter 2. At low V_{CE}, no significant heating is observed in the device, and the normalized thermoreflectance signals ($\Delta R/R$) within each emitter finger are nearly the same. At V_{CE} = 4V, it can be observed that the thermoreflectance signal (i.e. temperature) is roughly the same for both emitter fingers (spatially averaged over each finger, the left one has $\Delta R/R$ = 0.0103 and the right one has $\Delta R/R$ = 0.0108) although both have heated up to a temperature of 33^{o}C. This even temperature distribution suggests that the current density is also quite evenly distributed between the fingers. However, at V_{CE} = 5V, the thermoreflectance signals of the left and right fingers diverge, with the right one having $\Delta R/R$ = 0.0167 (40^{o}C) and the left one having $\Delta R/R$ = 0.0069 (28^{o}C). The temperature variation (ΔT) of the right emitter finger is 2.4 times that of the left finger.

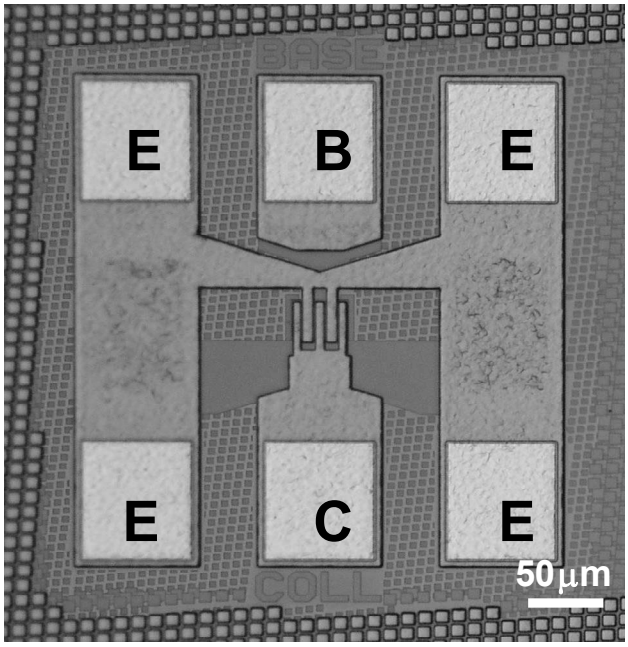

Fig. 3.10: Two-finger high-power SiGe HBT used for thermoreflectance measurement of current dynamics.

It is important to note that the left finger has a lower temperature at V_{CE} = 5V than at V_{CE} = 4V, even though the total collector current (to both fingers) has increased. This is direct evidence that current is being pulled from the left finger into the right finger (which gets much hotter) and is in agreement with the current hogging phenomenon discussed earlier for an HBT biased with constant base-emitter voltage.

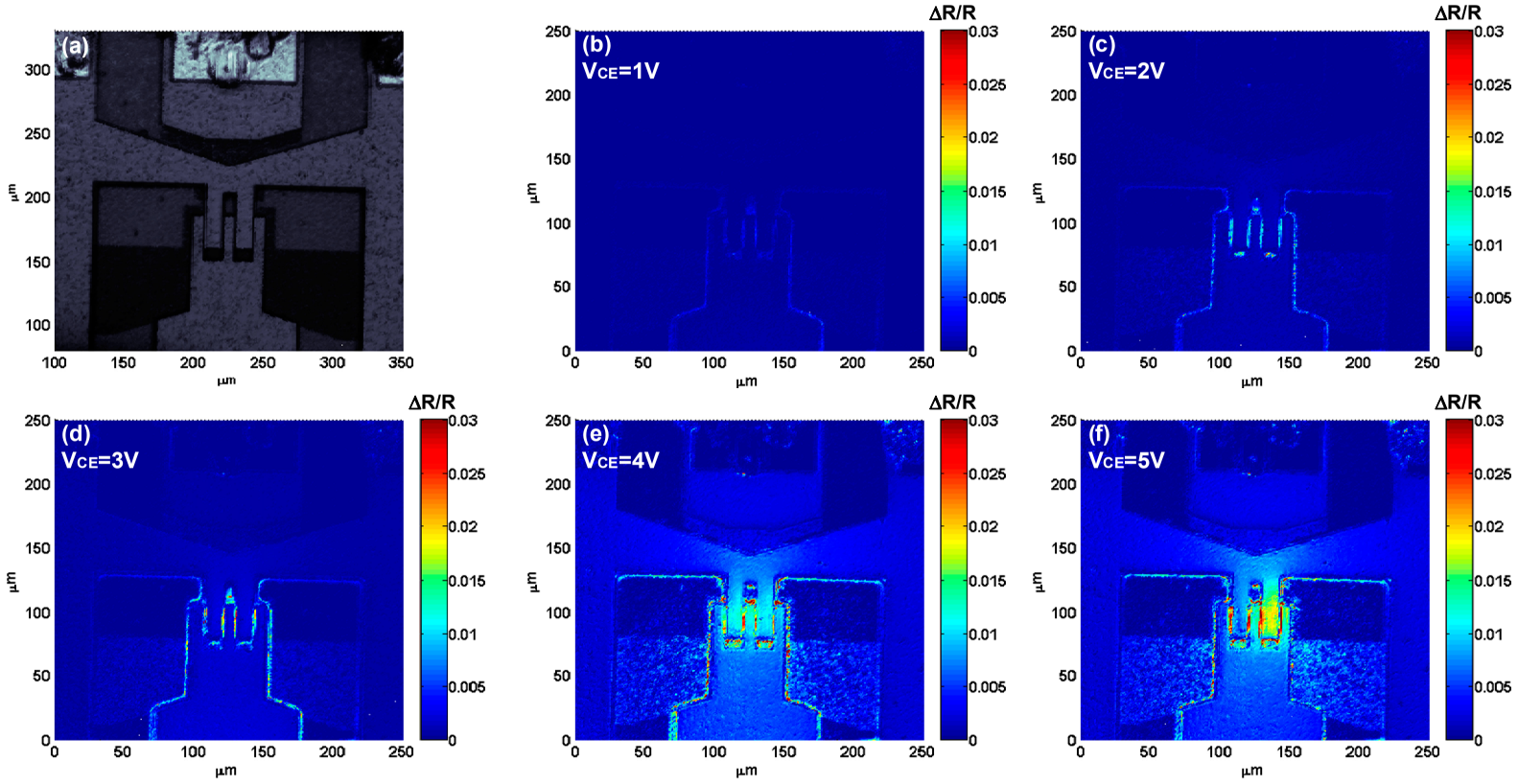

Fig. 3.11: (a) Optical image (R). (b)-(f) Normalized thermoreflectance images ($\Delta R/R$) of the SiGe HBT at different V_{CE} biases for V_{BE} =1.52V.

3.5 Thermal circuit of two-finger HBT for profiling current

Knowing the temperature variation between the fingers as a function of bias is not sufficient to calculate the current in each finger. In this section, we discuss a thermal resistance circuit which can be used to derive the current ratio between two fingers based on a measured temperature ratio. As shown in Fig. 3.12, we assume that the left and right fingers are generating two heat sources q_1 and q_2 respectively. From the thermal circuit, q_1 and q_2 can be written as

$$q_1 = \frac{T_1 - T_2}{R_{12}} + \frac{T_1 - T_0}{R_{th}} \tag{3.3}$$

and

$$q_2 = \frac{T_2 - T_1}{R_{12}} + \frac{T_2 - T_0}{R_{th}} \tag{3.4}$$

where T_1 and T_2 are the temperatures of the fingers and T_0 is the temperature of the substrate (which is here set by the Peltier cooler underneath). R_{th} is the thermal resistance between the fingers and the bottom substrate, and R_{12} is the coupling thermal resistance between the fingers. This latter parameter is very important because it reflects the strength of thermal interaction between the two fingers and is the reason that the current ratio between the fingers is not directly proportional to the temperature ratio.

Equations (3.3) and (3.4) can be solved simultaneously, remembering that the heat source generation in each finger is equal to the power consumption (i.e. $q_1 = I_1 V_{CE}$), to yield

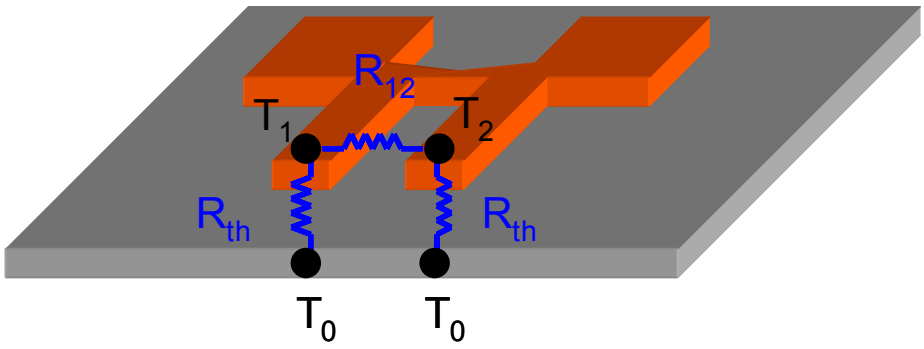

Fig. 3.12: Thermal circuit of the two-finger HBT. R_{th} is the thermal resistance from the finger to the substrate, R_{12} is the coupling thermal resistance between the fingers, and T_1, T_2, and T_0 are the left/right finger temperatures and heat sink temperature, respectively.

$$T_1 = R_a I_1 V_{CE} + R_b I_2 V_{CE} + T_0 \tag{3.5}$$

and

$$T_2 = R_b I_1 V_{CE} + R_a I_2 V_{CE} + T_0 \tag{3.6}$$

where $R_a = \frac{(R_{th} + R_{12}) R_{th}}{2R_{th} + R_{12}}$ and $R_b = \frac{R_{th}^{\ 2}}{2R_{th} + R_{12}}$ respectively. By dividing Eq. (3.5) by Eq. (3.6), the current ratio between the two fingers can then be written as

$$\frac{I_1}{I_2} = \frac{\frac{R_b}{R_a} - \frac{T_1 - T_0}{T_2 - T_0}}{\frac{T_1 - T_0}{T_2 - T_0}\frac{R_b}{R_a} - 1} \tag{3.7}$$

As shown in Eq. (3.7), in addition to the temperature ratio between the hot and cold fingers, the value $\frac{R_b}{R_a}$ is needed in order to evaluate the current ratio. It has been shown that for typical HBTs the ratio of R_{12} to R_{th} is approximately [59],

$$\frac{R_b}{R_a} = \delta\left(\frac{10}{D_f}\right)^{1.5} \tag{3.8}$$

where $\delta \approx 0.25$ and D_f is the distance between the heat sources (fingers) in μm. For the device under test, $D_f \approx 11.3$ μm and the thermal resistance ratio is therefore 0.2. Having thus taken inter-finger heat flow into account, we plot the current ratio relative to the total collector current for each finger in Fig. 3.13(a). The total current through each finger is shown in Fig. 3.13(b). It can be observed that the current is almost evenly distributed between the two emitter cells up to $V_{CE} = 4$V. At $V_{CE} = 5$V, current crowding causes 81% (182.1 mA) of the total collector current to flow through the right finger, while the left finger carries only 19% (42.3 mA) of the total current. This hogging effect is indicative of non-identical characteristics (always a practical issue in fabrication) for the two fingers that trigger thermal runaway at high bias.

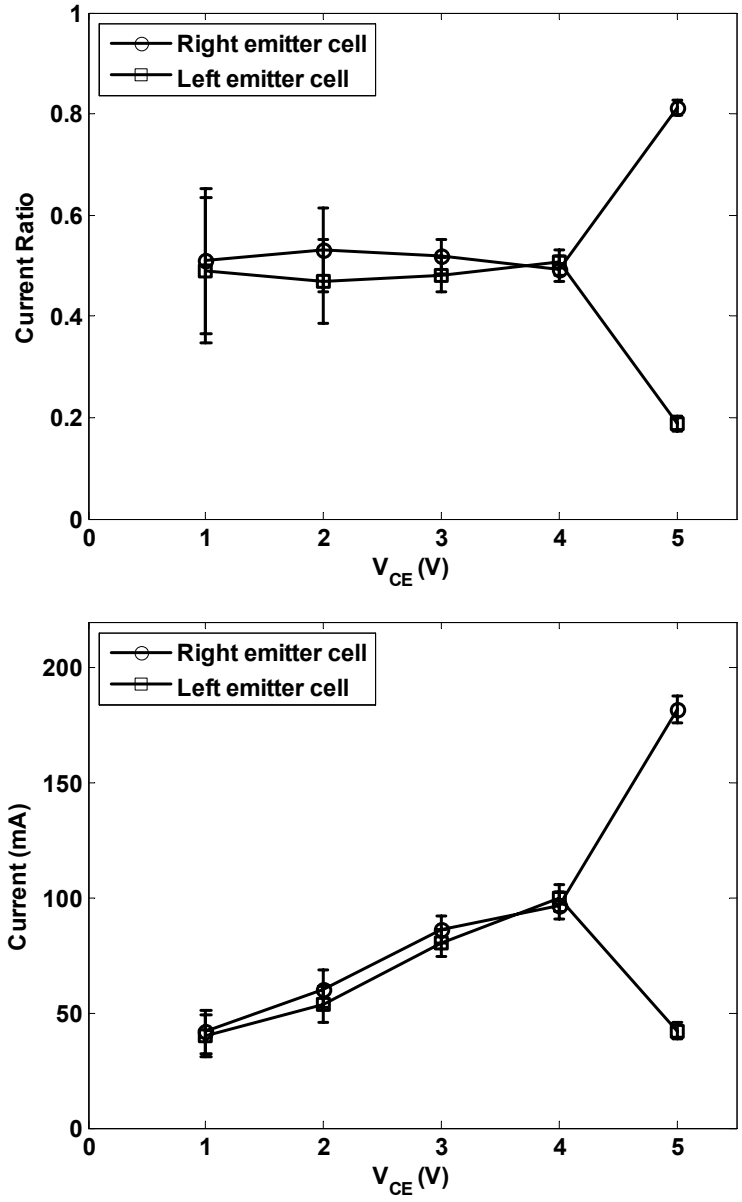

Fig. 3.13: (a) Current ratios and (b) total currents for the left and right emitter cells, derived from thermoreflectance imaging.

3.6 Summary

In this chapter, we have considered thermal instability in a multifinger HBT that can cause thermal runaway and eventual current collapse or device failure. Techniques such as ion implantation have been used previously to isolate individual finger currents under different bias conditions in an effort to measure the critical bias conditions under which the device becomes unstable. The main drawback of this technique is the extra fabrication steps which are impractical to apply for highly integrated circuits. In addition, the ion implantation process is a destructive and non-reversible process which may also cause the performance of the HBT to deviate from its normal state. We have shown that CCD-based thermoreflectance can instead be used to profile the individual finger currents of a high-power HBT in a nondestructive manner. Because of the high temperature resolution achieved (0.3K), thermal deviation between the fingers can be precisely quantified. Based on a thermal circuit model which considers the inter-finger thermal coupling, we can derive the current flowing in each sub-transistor. For the SiGe-based HBT under test, current hogging occurs at V_{CE} =5V for V_{BE} = 1.52V. At this bias point, we show that the colder finger carries only 19% of the total HBT current. These measurements indicate the overall advantages of using CCD-based thermoreflectance as a nondestructive tool for profiling current density in electronic devices and circuits.

Chapter 4

High resolution temperature mapping and thermal lensing in high-power laser diodes

4.1 Introduction

Thermal management is a major issue in the operation of high power lasers. A number of key parameters such as threshold current, device efficiency, lasing wavelength, and device lifetime are closely related to operating temperature. However, complex relationships between these parameters and temperature make it difficult to develop a comprehensive model of the influence of heating. Several theoretical models targeting only certain parameters have been proposed and successfully applied to laser diodes. Dutta *et al.* considered the carrier leakage effect on the threshold current of a $GaAs/Al_xGa_{1-x}As$ double heterostructure laser [60]. Uji *et al.* compared the non-radiative and radiative recombination components of the bias current in an InGaAsP/InP laser at different temperatures and associated the increase in threshold current at elevated temperature with stronger non-radiative recombination [61]. Recently, Fathpour *et al.*

demonstrated a high quality *p*-doped quantum dot laser at λ=1.3 μm that has a threshold current density independent of temperature from 278K to 323K [62]. Recognizing that thermal effects play an important role in laser performance, several different temperature measurement techniques have been applied for thermal characterization. Hayakawa applied single-spot thermoreflectance with an XYZ translation stage to measure the facet temperature distribution of a broad stripe InGaAsP quantum well laser [63]. Dilhaire *et al.* applied single-spot thermreflectance to an AlGaAs laser and measured how the temperature of a particular location on the facet changed with bias [64]. In this work, we perform high-resolution thermal imaging of a high-power laser diode facet, deriving the non-radiative recombination power by combining the facet temperature image with a thermal circuit model. Considering the effect of temperature on refractive index, we predict the optical mode variation due to thermal lensing and compare our prediction with direct beam measurements.

4.2 Slab coupled optical waveguide laser (SCOWL)

The high-power laser diode under study here is a slab-coupled optical waveguide laser (SCOWL) developed at Lincoln Laboratory (Massachusetts Institute of Technology). In 1974, Marcatili performed the first detailed analysis of slab-coupled waveguides [65], examining the effects of slab height, rib height, and rib width on guiding optical modes. In 2002, Walpole *et al.* at Lincoln Laboratory first combined diode lasing with a slab-coupled waveguide [66]. Since then, 980-, 915-, 1330-, and 1550-nm SCOWLs have been successfully demonstrated [67,68,69]. In addition, slab

coupled optical waveguide amplifiers (SCOWAs) [70] and passively mode-locked SCOWLs at λ=1.5 μm have been demonstrated recently [71].

The InP-based SCOWL generates large optical modes (>5×5μm^2) with nearly circular diffraction-limited beam quality by filtering higher-order modes from an otherwise multimode InGaAsP rib waveguide to an adjacent slab region and tailoring the quantum wells (QWs) such that the fundamental mode is the only mode with net gain [69]. The two most significant advantages of SCOWLs over other high-power laser diodes are that 1) their large, round, single-mode optical output allows direct coupling into single-mode fiber without any optical lenses, and 2) their large output mode reduces the power density at the facet, leading to a lower temperature.

The device under test is a 1-cm-long InGaAsP/InP SCOWL fabricated on an *n*-InP substrate. A 5-μm-thick lightly doped InGaAsP waveguide is grown on top of the substrate, and five 8-nm quantum wells (QWs) with 1% compressive strain and tensile-strain InGaAsP barriers are then deposited on the waveguide. Finally, a *p*-InP cladding layer (1.0 μm) with a graded doping profile and a *p*-InP cap (0.6 μm) are deposited on top of the barrier layer. The device with detailed dimensions is shown in Fig. 4.1. The laser emits at λ=1.55μm and has a threshold current of I_{th} = 500mA.

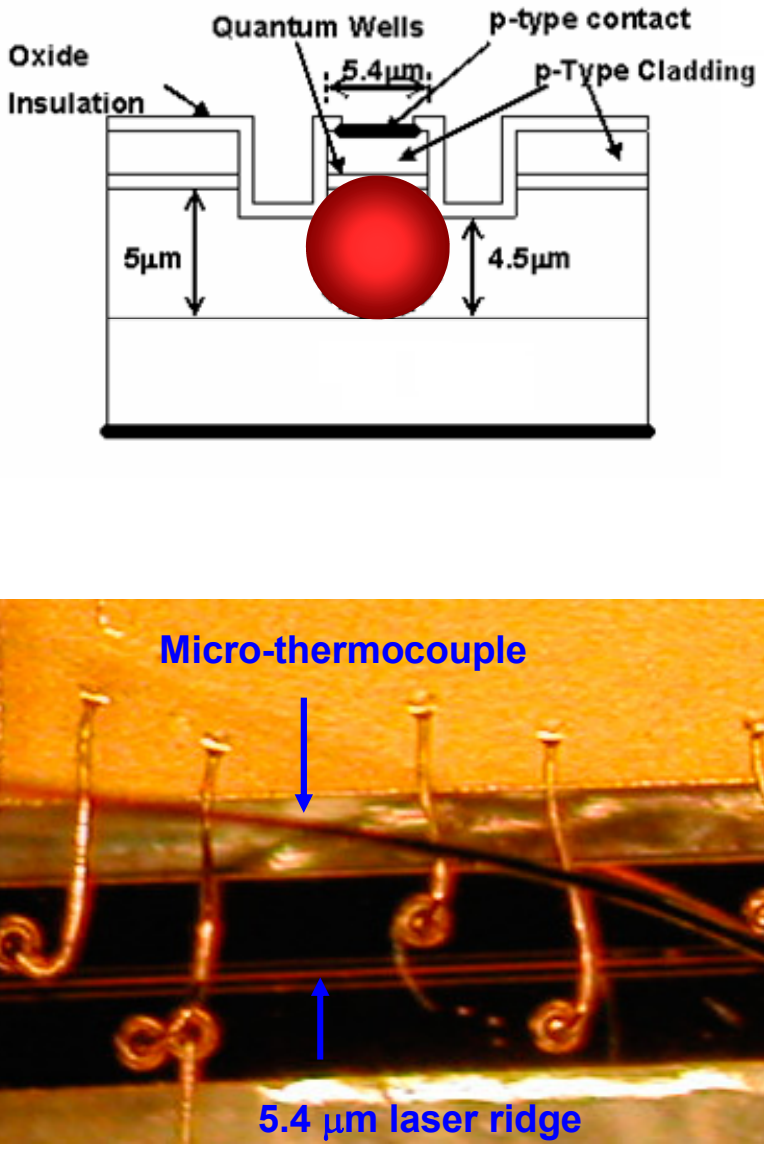

Fig. 4.1: (Top) Schematic of the slab-coupled optical waveguide laser (SCOWL) structure. (Bottom) Top view of a SCOWL device, with wirebonds for current injection. A micro-thermocouple was used as shown for thermoreflectance coefficient calibration.

4.3 Temperature measurement of SCOWL facet

In order to study the thermal properties of the SCOWL, CCD-based thermoreflectance is applied to measure the facet temperature distribution. The experimental setup is very similar to the one described in Chapter 2, with the exception of an angled mirror used to redirect the light onto the facet. The laser is placed on the edge of the Peltier temperature-controlled stage, and a silver-coated mirror (Thorlabs) is placed at a 45-degree angle next to the laser facet as shown in Fig. 4.2. The LED light is focused on the facet by passing through the objective and reflecting off of the mirror.

An important issue relevant to high-resolution thermoreflectancing imaging of high-power devices is thermal expansion. Since profiling the active region requires a high power objective (Mitotoyo 100X, NA=0.62), small movements of the sample or the X-Y stage on which it sits can easily blur the thermoreflectance image. In order to minimize device thermal expansion, high thermal conductivity epoxy (Melcor) is used to ensure good heat dissipation from the device to the Peltier cooler. A further issue, especially relevant to high-power lasers, is that the laser light may contaminate the thermoreflectance signal. In order to eliminate such contamination, we place an OD 6 filter (Omega Optical, Inc.) between the objective and the CCD camera to filter out the light from the laser diode and pass through the light from the blue LED. We can verify that the measured thermoreflectance signal is not contaminated by performing a reference experiment with the LED light turned off to determine if any spurious "thermoreflectance" signal is detected. In the case of our SCOWL measurements (and all other laser measurements in this work), no such contamination signal was detected.

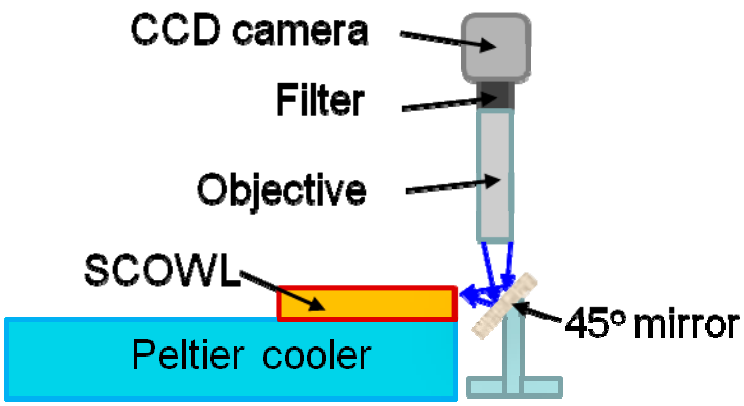

Fig. 4.2: Setup for CCD-based thermoreflectance measurements of a SCOWL. A 45-degree silver-coated mirror is used to redirect the LED light onto the laser facet.

Optical and thermal images of the SCOWL at different bias levels are shown in Fig. 4.3 [72]. In order to better display the active region temperature at low bias levels (<1200mA), the first 3 thermal images, i.e. 100mA, 600mA and 1200mA, are shown with a smaller temperature range scale bar than the high-bias images.

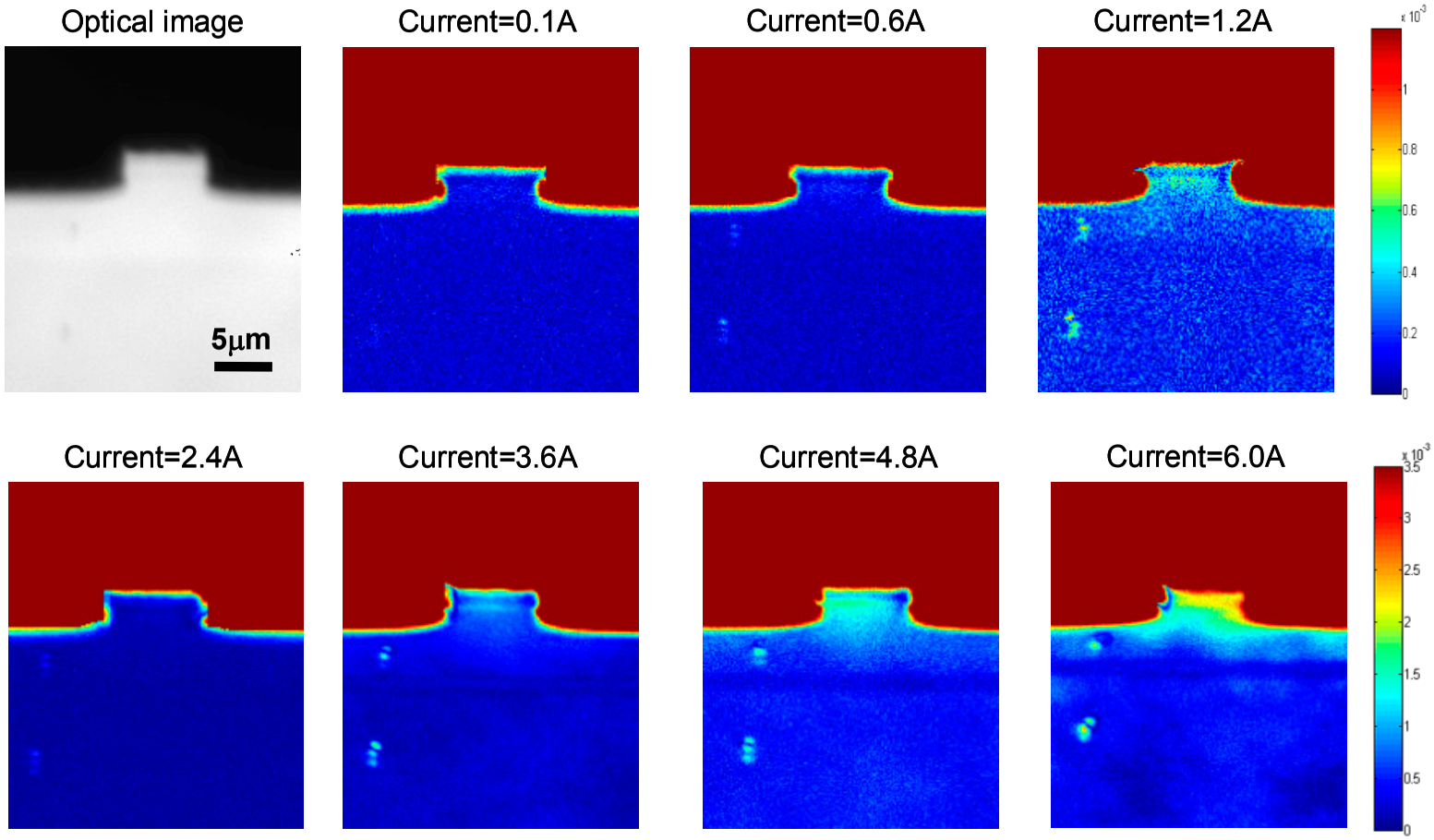

Fig. 4.3: Optical and thermoreflectance images of the SCOWL at different bias levels.

4.4 SCOWL thermal circuit and heat transfer mechanisms

A thermal circuit model can be used in conjunction with the above thermoreflectance images at different bias currents to derive the heat source distribution on the SCOWL facet. The heat transfer mechanisms of laser diodes in different material systems have been studied intensively in the past decades [73,74,75] because of the close relationships between key device parameters and device temperature. These dependencies are especially important for the operation of high-power lasers, in which device heating is the main cause of decreased performance and failure [76].

In a laser diode, most of the heat generated near the active region is due to the non-radiative recombination of injected carriers (electrons and holes) by the Auger process or by trapping at surface defects or deep levels [77]. Hot carriers then couple to the lattice near the quantum wells and increase its temperature. Another heating mechanism is optical absorption (followed by non-radiative decay) in the waveguide. While the bulk waveguide has a larger bandgap energy than the light generated in the quantum wells, waveguide optical absorption can take place due to thermally-induced bandgap shrinkage (especially relevant at the facets), defect absorption, or intervalence band absorption. However, as shown in Fig. 4.3, the temperature profile of the SCOWL exhibits a continuous temperature drop along the waveguide, suggesting that the optical absorption in the waveguide of the SCOWL can be neglected.

There are two main mechanisms by which heat can be removed from a device: convection at the device top surface and conduction through the substrate to a heat sink.

A thermal circuit model of the SCOWL structure provides a basis for understanding this heat dissipation. As shown in Fig. 4.4, the heat convected from the top surface of the device first conducts through the *p*-cladding layer and is given by

$$q_{up} = \frac{(T_{active} - T_{p-cladding})}{Z_{up}} \tag{4.1}$$

where T_{active} is the active region temperature, $T_{p\text{-}cladding}$ is the *p*-cladding temperature, and Z_{up} is the thermal resistance for the upward flowing heat flux.

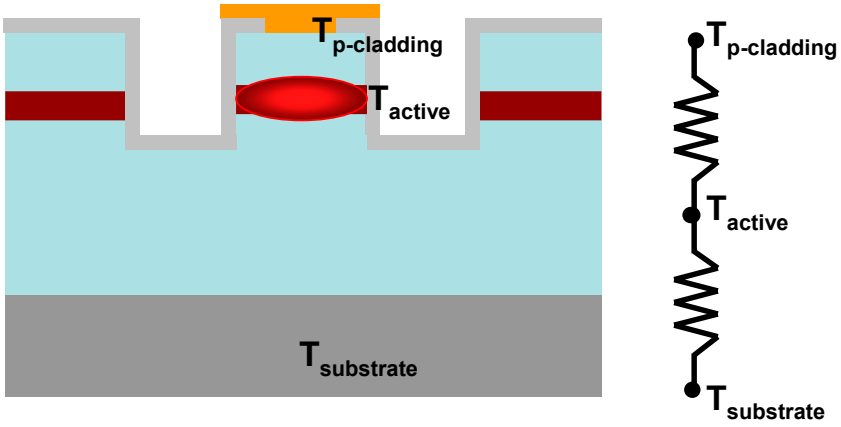

Fig. 4.4: (Right) Thermal circuit of the SCOWL. (Left) SCOWL temperature distribution illustration, where $T_{p\text{-}cladding}$, T_{active}, and $T_{substrate}$ represent the *p*-type cladding, active region, and substrate temperatures.

The value of Z_{up} can be evaluated by

$$Z_{up} = \frac{L_{p-cladding}}{k_{p-cladding} A} \tag{4.2}$$

where $L_{p\text{-}cladding}$, $k_{p\text{-}cladding}$, and A are the thickness, thermal conductivity, and cross-sectional area of the cladding layer, respectively. The heat dissipated through the substrate to the Peltier heat sink can be written as [78]

$$q_{down} = \frac{T_{active} - T_{substrate}}{Z_{down}} \tag{4.3}$$

where the downward thermal resistance is given by

$$Z_{down} = \frac{\ln(4h/w)}{\pi k_s l} \tag{4.4}$$

with h, w, and l being the thickness, width, and length of the laser diode [79].

Based on known device geometric factors and literature values for layer thermal conductivities, the values of Z_{up} and Z_{down} are calculated to be 0.333 K/W and 2.325K/W, respectively. It is important to notice that in order to apply Eqs. (4.1) and (4.3), a high resolution thermal image that can differentiate the temperature variation at different regions of the facet is necessary; the temperature map measured by CCD-based thremoreflectance is very suitable for this purpose. Substituting the measured temperatures at the active region, *p*-cladding, and substrate at different current bias levels into Eqs. (4.1) and (4.3), the total non-radiative recombination power as a function of bias can be derived. As shown in Fig. 4.5, the nonradiative power dissipation increases as expected with increasing input current. It is also clear that there is a significant temperature difference between the active region and the p-cladding cap layer as shown in Fig. 4.5. This suggests that the nonradiative recombination power will be underestimated if only the heat flux downward from the active region is considered. In order to obtain an accurate estimate of the nonradiative heating within the active region of the device, it is necessary to also account for the convective heat flux from the device

top surface. In addition, Fig. 4.5 indicates that the surface temperature of the top metal contact is lower than the true active region temperature by a significant amount (>20%), especially at high bias levels. This contrasts with the commonly used approximation in which the laser active region temperature (which sets the performance characteristics of the device) is assumed to be same as the top surface temperature [80].

It is therefore clear that the temperature profile of the laser is significantly affected by heat dissipation through surface convection. For our experimental setup, since no air is forced to flow along the device surface, the surface experiences natural convection, i.e. air movement as a result of buoyant force rather than external forces. In order to determine the fraction of heat leaving the device by convection versus conduction, we can evaluate the heat transfer coefficient given by

$$h = \frac{q_{up}}{\Delta T \cdot A} \tag{4.5}$$

where ΔT is the temperature difference between the top metal layer and the ambient and A is the surface area from which convection takes place. By taking A as the top contact area (1×10^{-4} m^2) and assuming the room temperature is at 20°C, we find that the heat transfer coefficient is approximately 3200 W/m^2-K, which coincides with prior measurements on a similar laser structure [81].

In order to verify that Joule heating is not significant at the active region, the device bias frequency f is lowered to 5Hz and the camera is set to take pictures at 40Hz. In this way, the measurement can isolate heating components that are proportional to I (approximately true for nonradiative recombination) from those that vary as I^2. Joule heating (I^2R) is expected to

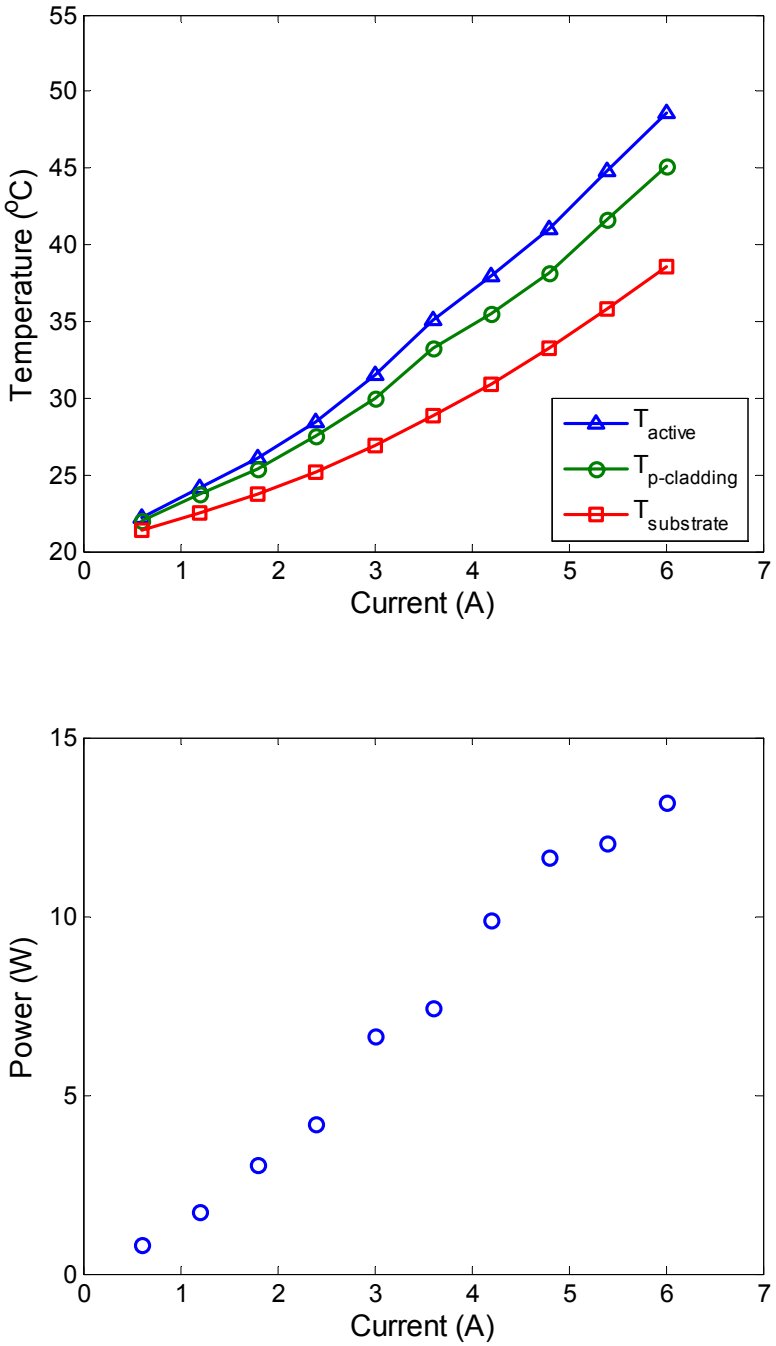

Fig. 4.5: (Top) The average temperature measured by thermoreflectance at different regions of the SCOWL. (Bottom) The total non-radiative recombination power in the SCOWL active region calculated using the thermal circuit model and the measured temperatures at the active region, *p*-cladding, and substrate.

have a component at $2f$ (2×5Hz=10Hz). The center line temperature of the SCOWL at I = 2.4A is shown in Fig. 4.6. The first harmonic thermoreflectance signal at 5Hz (which contains both non-radiative recombination and Joule heating components) is considerably stronger than the second harmonic signal (which only contains I^2R components). This suggests that Joule heating plays a minor role in the heating [82].

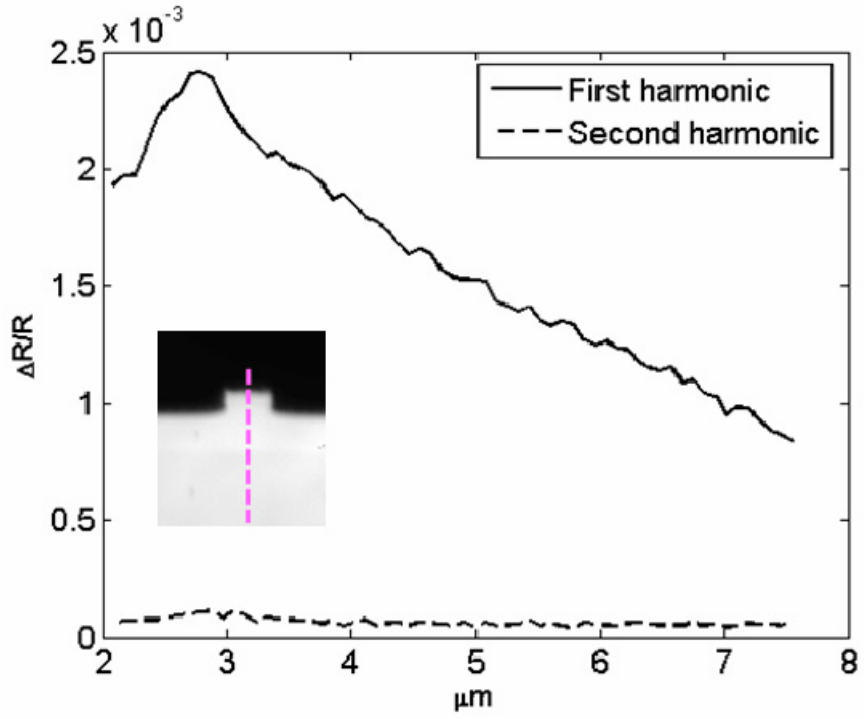

Fig. 4.6: First and second harmonics of the thermoreflectance signal at I=2.4A. The second harmonic thermoreflectance signal is much weaker than the first harmonic, suggesting that Joule heating is negligible at the facet. Inset shows the location of the center line.[82]

4.5 Thermal lensing in high power edge emitting laser diodes

The refractive index (n_r) profile of a device is an important factor that governs its optical output mode size and shape. The electric field (E) at the facet is given by the Helmholtz equation,

$$\nabla^2 E(x,y) + n_r^2 k_0^2 E(x,y) = 0 \tag{4.6}$$

where $k_0 = 2\pi/\lambda$ is the free space wave number and n_r is the refractive index profile of the device materials. The electric field (E) solution to Eq. (4.6) will give the optical output mode. Variation in refractive index will change this solution and will therefore vary the optical mode size and shape. There are two main factors that, when changed, cause such alteration of the refractive index: carrier density and temperature. As discussed in Section 2.2, the carrier concentration effect is only important in regions where large variation of carrier density occurs, i.e. the active region, and is compensated by spatial averaging due to the small size of the active region with respect to the CCD-based thermoreflectance instrument's spatial resolution. In contrast, the temperature variation affects a broader range of areas because of the large thermal diffusion length ($L_{thermal}$) compared to the device thickness. $L_{thermal}$ can be written as

$$L_{thermal} = \sqrt{\frac{\alpha}{\pi f}} \tag{4.7}$$

where α is the thermal diffusivity and f is the device bias frequency. For III-semiconductor materials, the thermal diffusivity ranges in the order of 0.1cm^2/s to 1cm^2/s [83], and the bias frequency is 10Hz, making for a thermal diffusion length $L_{thermal}$ in the range of 500-1800μm. Since the thermal diffusion length is larger than the total thickness

of the device and substrate, it is reasonable to assume that the refractive index change due to temperature variation occurs over a much larger area than the index change due to carrier concentration variation. A typical InGaAsP QW high-bias carrier concentration of 10^{18} cm^{-3} will yield a refractive index variation Δn_r of −0.02 and $\Delta R/R$ of −0.008. At I=6 A, we measure $\Delta R/R$ to be approximately 0.0058 in the QW region for the SCOWL and use this as a typical value. Accounting for spatial averaging (the QW region is only 40 nm of the 500 nm resolution), this translates to an error in temperature measurement of 15% for the line of pixels directly on the QWs. It is worth noting that the SCOWL has very little carrier leakage and thus we do not expect significant carrier-induced index modulation in the regions near the active region.

Since the value of dn_r/dT is usually positive for semiconductors, an increase in temperature will lead to an increase in n_r, which will then result in a decrease of the optical mode size [Eq. (4.6)]. This thermally-induced variation in optical mode size is known as thermal lensing and can greatly affect the light coupling efficiency into optical fiber. From the temperature profile at the facet measured by CCD-based thermoreflectance, a map of temperature-induced refractive index change can be derived and can then be used as an input to a finite-element optical modesolver that solves the Helmholtz equation. In this way, we can predict thermal lensing effects as well as check the validity of our thermal measurements by comparing our predictions to direct beam measurements.

The temperature-induced refractive index variations for InP and InGaAsP are given by

$$\Delta n_{InP} = \frac{dn_{InP}}{dT} \Delta T_{InP} \tag{4.8}$$

and

$$\Delta n_{InGaAsP} = \frac{dn_{InGaAsP}}{dT} \Delta T_{InGaAsP} \tag{4.9}$$

where the literature values for dn_{InP}/dT and $dn_{InGaAsP}/dT$ used in the finite element modesolver are 1.9×10^{-4} K^{-1} and 5.0×10^{-4} K^{-1} respectively [84,85]. Fig. 4.7 shows direct laser optical beam measurements taken at various bias levels by a phosphor-coated Si CCD camera, and Fig 4.8 shows finite element simulation results. A noticeable mode contraction can be observed at high bias levels in both experiment and simulation, which we attribute to thermal lensing. Fig. 4.9 shows the normalized mode size in *x* and *y* directions as a function of bias current. It can be observed that the mode size drops 20% when the current increases from 1A to 5A. Such a large decrease in mode size will greatly affect the SCOWL's coupling to single mode optical fiber, as discussed in the next section.

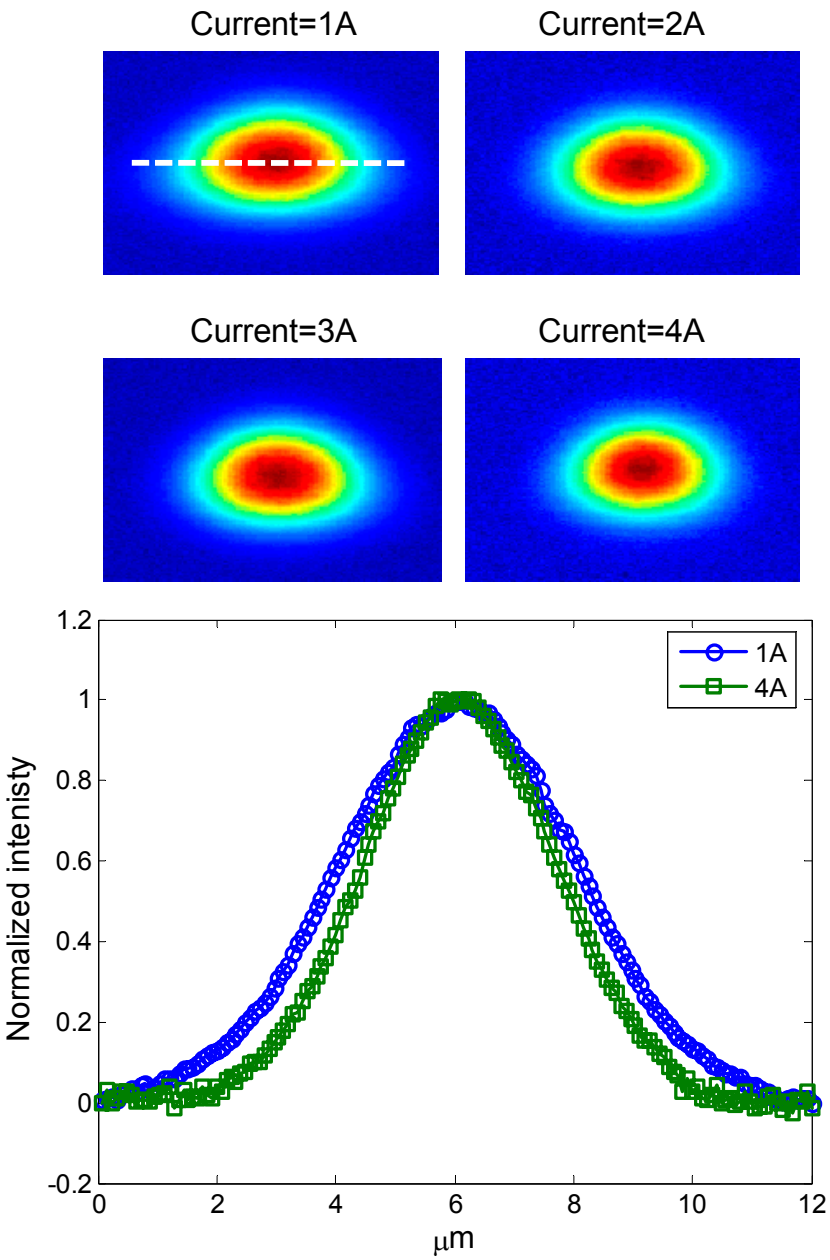

Fig. 4.7: (Top) Experimental results of the SCOWL optical mode intensity measured by a phosphor-coated Si CCD camera focused through an attenuator on the facet (courtesy of J. Plant, MIT Lincoln Lab). (Bottom) Horizontal mode profiles taken at the dotted lines shown in the top figure, demonstrating thermal lensing.

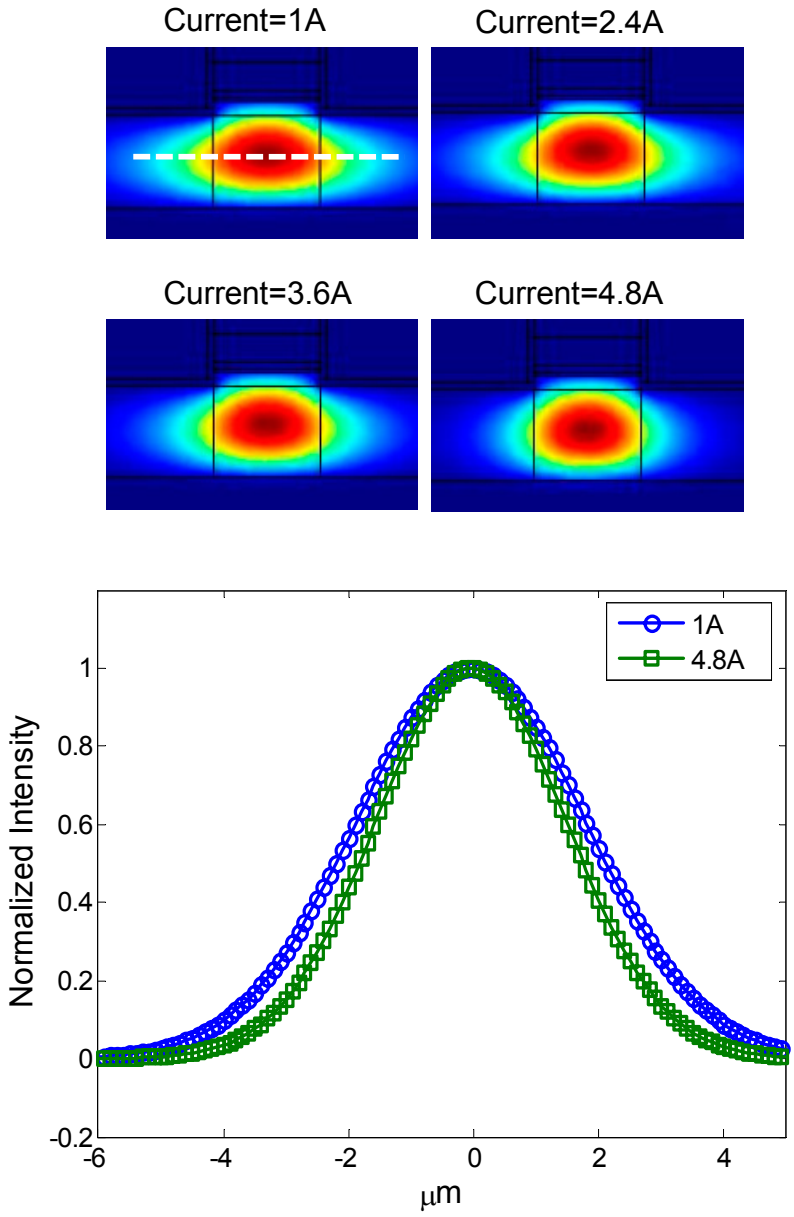

Fig. 4.8: Finite-element simulation of the optical mode size as a function of bias. The measured two-dimensional temperature maps are used in the finite element model as input parameters. (Bottom) Horizontal mode profiles taken at the dotted lines shown in the top figure.

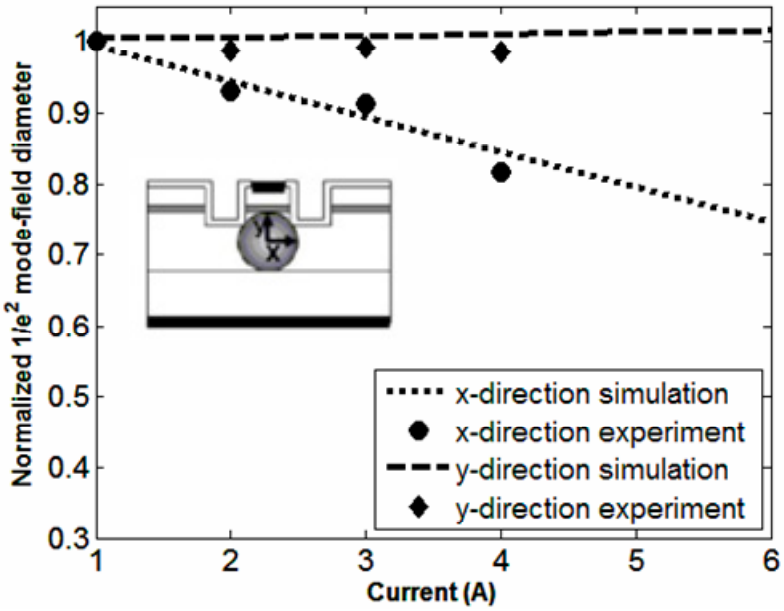

Fig. 4.9: Normalized $1/e^2$ mode-field diameter of the optical mode in the x and y directions. The x direction has an 18% drop as the current increases from 1 to 4 A.

4.6 Optical coupling efficiency between the SCOWL and single mode optical fiber

Assuming that a laser diode and the end of a single mode fiber are in close proximity without any tilting angle with respect to each other, their coupling efficiency can be approximated by that of two Gaussian beams and can be written as [86]

$$\eta = \frac{4 w_x w_b w_{fiber}^2}{\left(w_x^2 + w_{fiber}^2\right)\left(w_y^2 + w_{fiber}^2\right)} \tag{4.10}$$

where w_x and w_y are the beam waists at the laser facet in the x and y directions and w_{fiber} is the beam waist in the fiber. This maximum coupling efficiency is plotted at various SCOWL bias levels in Fig. 4.10, accounting for thermal lensing as measured in the previous section, with the assumption that the core diameter of the fiber is 3.1 μm. As shown in Fig. 4.10, the coupling coefficient increases in a linear fashion with the bias current due to thermal lensing of the optical mode (which at low bias is approximately 5 μm in diameter, significantly larger than the fiber diameter). At I = 5A, the coupling coefficient between the laser diode and the single mode optical fiber has a 10% increase above the low-bias value. Such an increase in the coupling efficiency at high bias is promising for implementing the SCOWL as a high-power light source in optical communication systems.

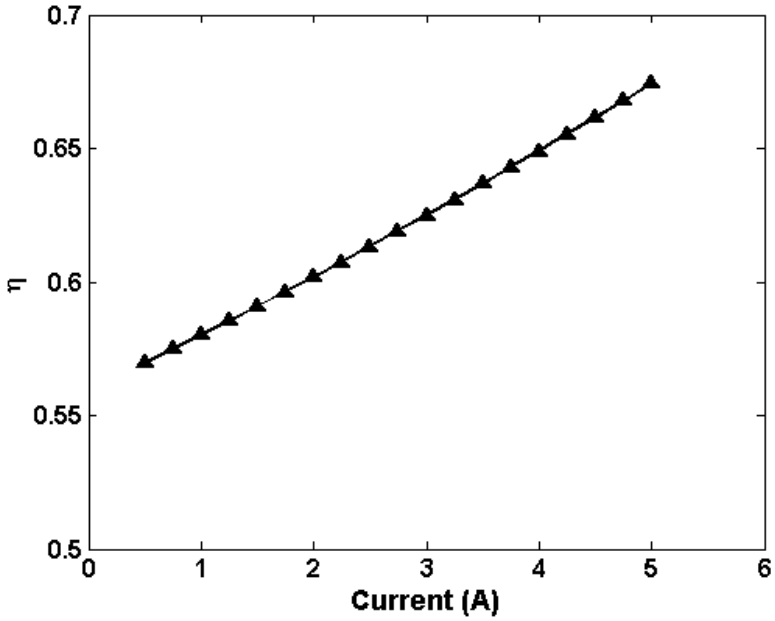

Fig. 4.10: The predicted coupling efficiency between a SCOWL and single mode optical fiber, assuming thermal lensing as measured in Section 4.5. The core diameter of the fiber is assumed to be 3.1 μm.

4.7 Summary

Thermal management is one of the main challenges in high power laser diode operation. Thermally induced problems include increased threshold current, wavelength drift, and decreased reliability. Although advanced heat sinks have been implemented to regulate the temperature at a device boundary, most high-power lasers exhibit large temperature gradients internal to the device due to highly localized heat sources. This is important because it is the temperatures at different device layers (not the device boundary) that govern the performance of the device. The average temperature increase of the active region can be determined indirectly by relating it to peak wavelength drift;

however this does not yield any spatially-resolved information about the location of device-internal heat sources. A high spatial and temperature resolution measurement technique is therefore called for to characterize high-power laser diodes. By performing CCD-based thermoreflectance on a SCOWL facet, we show that the active region temperature, *p*-cladding temperature, and substrate temperature can be measured directly and independently. Using the temperature map as the input to a thermal circuit, we demonstrate a direct evaluation of the non-radiative recombination power. In addition, we use the two-dimensional thermal image obtained by CCD-based thermoreflectance to predict thermal lensing. The comparison of direct beam measurements with predicted mode size based on thermal measurements shows good agreement, further validating the thermoreflectance measurements.

Chapter 5

Temperature measurements of a pulsed InGaAs/GaAs quantum dot laser

5.1 Introduction

Many modern electronics do not operate at continuous (DC) bias, but rather operate in pulsed mode. The switching properties of transistors, for example, are integral to most of their applications, and vary based on material composition and other components of device design [87]. Similarly, pulsed mode is often used in communications applications of laser diodes; the laser is turned on and off through direct modulation of the input current to achieve transfer of information. A reliable laser diode for communications therefore requires high bandwidth and small linewidth enhancement factor, i.e. large modulation frequency range and small signal dispersion [88]. Fathpour *et al*. showed that InGaAs p-doped λ=1.3μm quantum dot (QD) lasers can have a modulation bandwidth of 8 GHz [89]. Subsequently, Mi *et al*. demonstrated tunnel-

injection λ=1.3μm InGaAs quantum dot lasers with a modulation bandwidth of 11GHz and zero linewidth enhancement factor [90].

The self heating of a laser diode can limit its operable range of duty cycle and modulation frequency. Under continuous-wave (CW) operation, the device temperature is higher than in pulsed operation [91]. Such high temperature causes a lower optical output power because of increased carrier leakage and (in most cases) increased Auger recombination. For temperatures above a certain point, the laser has zero optical output. In fact, many laser diodes can only operate in pulsed mode rather than CW because the operating temperature is too high in the CW mode, preventing population inversion.

Profiling the temperature of lasers in pulsed mode using CCD-based thermoreflectance is complicated by the typically high pulse rate. Most pulsed lasers are designed to operate at frequencies (GHz) much higher than the frame rate of a CCD camera (~100Hz). While single-point measurements during pulsed operation are possible, they do not yield spatially-resolved information about device temperature, as discussed in Chapters 2 and 4. Here we will explore a new mode of high resolution CCD-based thermoreflectance that can be used to measure pulsed devices, applying it in this case to profile the active region temperature and contact heating of a λ=1.1μm InGaAs quantum dot laser. In addition, we will demonstrate how to use this technique to measure the thermal relaxation time constant of the laser diode.

5.2 λ=1.1μm InGaAs quantum dot laser

The device under test is a λ=1.1μm tunnel-injection *p*-doped quantum well laser provided by Prof. Pallab Bhattacharya at the University of Michigan [89]. The heterostructure design and a scanning electron microscope image of the device are shown in Figs. 5.1 and 5.2 respectively. The active region of the device consists of a 95Å $In_{025}Ga_{0.75}As$ injector wall, a 2Å $In_{055}Ga_{0.45}As$ tunnel barrier, and three $In_{05}Ga_{0.5}As$ quantum dot layers. Such a structure allows the conduction band energy difference between the injector layer and the quantum dot ground state to be 36meV (which is the longitudinal optical phonon energy of GaAs), enabling phonon-assisted tunnel injection of electrons [92]. In addition, in order to reduce the thermal broadening of holes in the quantum dot, a heavily *p*-doped layer ($N_a = 5\times10^{17}$ cm^{-3}) is used to provide extra holes for the quantum dots and enhance gain.

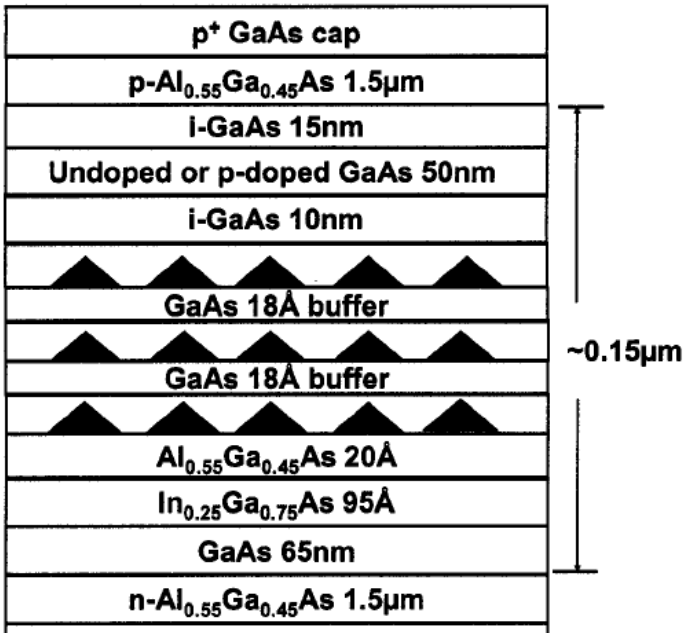

Fig. 5.1: Heterostructure design of the λ=1.1μm quantum dot laser under test.

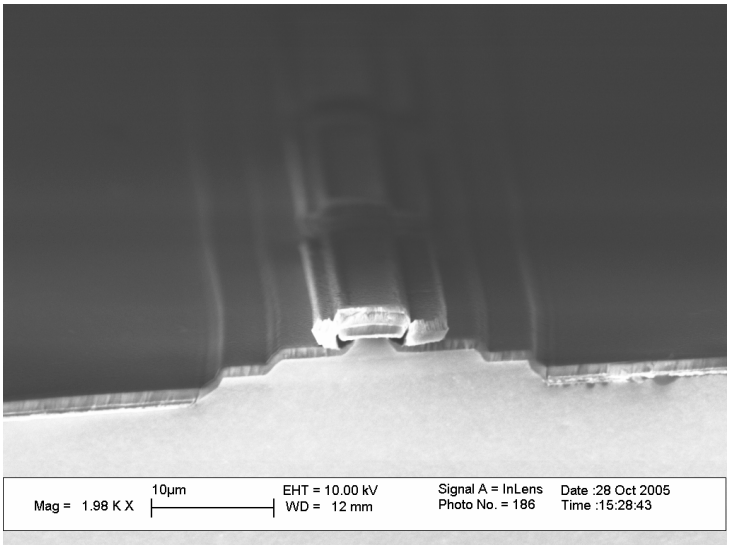

Fig. 5.2: Scanning electron microscope image of the laser facet.

5.3 CCD-based thermoreflectance for pulsed devices

The CCD camera we use for thermoreflectance measurements has a maximum frame rate of 80 frames per second (fps). As discussed in Section 2.4, during each device bias cycle, four images (I_1, I_2, I_3 and I_4) are required to obtain the thermoreflectance signal ($\Delta R/R$). With this method, therefore, the maximum bias frequency of the device is 20Hz. Most pulsed devices, however, operate at frequencies much greater than this. In addition, the duty cycle (percentage of the bias cycle period for which the bias is nonzero) must often be restricted to a small range of the pulse period.

In order to overcome the limitation of the CCD camera frame rate, a modified CCD-based thermoreflectance experiment setup is designed for high frequency modulation devices. The schematic of the setup is shown in Fig. 5.3 The CCD camera remains triggered by the 40Hz signal, which is now phased lock to a 20Hz envelope signal. Within the envelope signal, a high-frequency square wave (at the desired duty cycle) is generated and sent to the current source to bias the device. As shown in Fig. 5.3, I_1 and I_2 are the images taken during the "on" and "off" envelopes, respectively. In the specific experiment performed here, I_1 is an averaged image taken while the InGaAs quantum dot laser is biased at 10kHz, 120mA, and I_2 is an image taken when the device is off. Since the envelope is at 20Hz and the width of the "on" envelope is 25ms (half of the actual period of the envelope), there are a total of 250 10kHz cycles within the "on" envelope. The normalized reflectivity variation, i.e. the thermoreflectance signal, can be obtained by using the two images I_1 and I_2:

$$\frac{\Delta R}{R} = \frac{I_1 - I_2}{I_2} \tag{5.1}$$

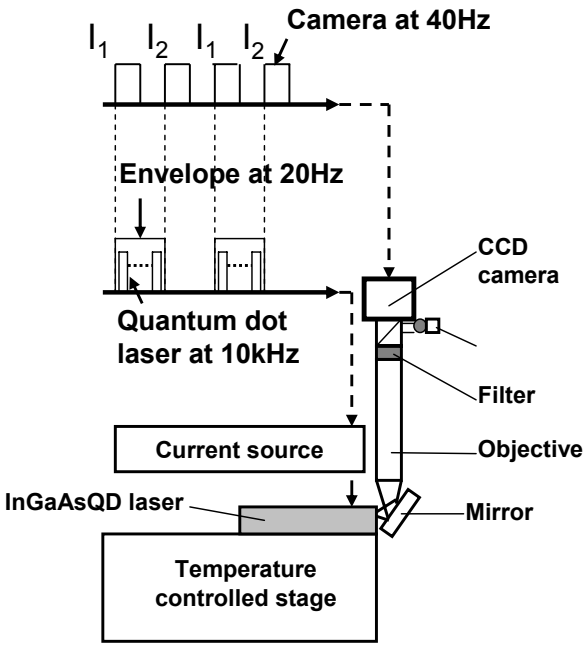

Fig. 5.3: Experimental setup for high frequency CCD-based thermoreflectance.

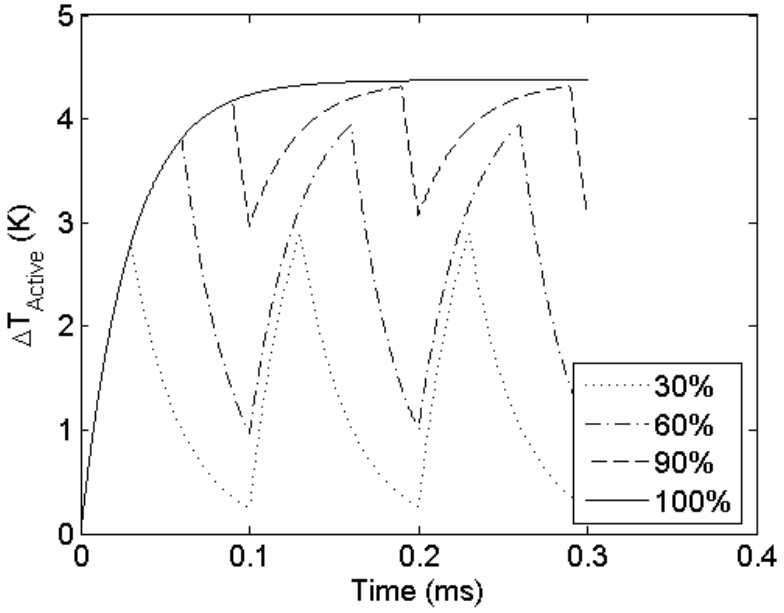

Fig. 5.4: Simulated active region temperature response to 120mA current pulses at 10kHz with 30%, 60%, 90%, and 100% duty cycles.

The duty cycle of the laser (which we vary from 30% to 90%) can be adjusted by changing the pulse width of the signal being sent to the laser diode. This does not, however, change the number of laser pulses per trigger pulse. In order to measure the very small variation in reflection between consecutive half periods, we average the reflectance signal of each pixel over more than 10000 periods. By setting the exposure time of the camera to be 24.5ms (98% of the envelope half period), we can maximize the integrated thermoreflectance signal and thus enhance the signal-to-noise ratio. An OD-6 filter (Omega Optical 450DF100) is installed on the microscope to filter out the (λ=1.1 μm) light generated by the laser under bias, and the Peltier temperature controller is used to maintain the temperature under the laser at 20 °C. As with the high-power lasers tested

in Chapter 4, no laser light signal is observed on the CCD when the LED is turned off, verifying that the laser light does not contaminate the thermoreflectance measurement.

A further thermal issue arises when biasing devices at high frequencies. In previous chapters, we have discussed the use of CCD-based thermoreflectance to measure the temperature variation of devices biased at low frequency (less than 10Hz). For micoscale devices such as transistors and laser diodes, such a low frequency approaches DC conditions because the thermal relaxation time is typically in the range of 10-100μs, much shorter than 1/10 = 0.1s. In other words, when the device is modulated with a 10Hz square wave to achieve the signal variation needed for software-based lock-in (i.e. averaging over many samples), it achieves steady state temperature much more quickly than the rate at which the signal varies. Consequently, given a constant peak-to-peak current input range, the measured temperature will remain the same regardless if the device is biased at 10Hz, 5Hz or 1Hz. However, this is not the case if the device under test is modulated at a frequency faster than its thermal relaxation time; in this case, the device never reaches a steady-state temperature, and as a result the temperature variation amplitude decreases. This is illustrated in Fig. 5.4 which plots the time-varying temperature of the QD laser active region under 10 kHz bias at various duty cycles and the details of the calculation will be discussed in section 5.5. For a 30% duty cycle, it can be seen that the maximum active region temperature is significantly lower than for a 100% duty cycle (i.e. CW operation), hence the use of pulsed operation at small duty cycles for devices that cannot operate at high temperature.

5.4 Thermoreflectance images of a pulsed InGaAs quantum dot laser

A CCD-based thermoreflectance image of the λ=1.1μm InGaAs laser diode at 120mA, 10kHz, and 90% duty cycle, using the modified setup for pulsed devices described above, is shown in Fig. 5.5. Two significant heat sources can be differentiated in the high resolution temperature map: 1) the contact heating and 2) the active region heating. Contact heating happens when the carriers are injected from the metal into the p-doped region, while active region heating is due to non-radiative recombination in the quantum dot and wetting layers [93,94]. Vertical and horizontal cross-sections of the thermoreflectance profile at 90% duty cycle are plotted in Fig. 5.6 [95].

It is important to note that the measured thermoreflectance value cannot be immediately converted into temperature variation by Eq. (2.6). Because the CCD integrates over the course of taking each image frame, the measured signal during each "on" envelope represents a time-averaged (flat) function with the same cumulative area as the peaks. As a result, the measured reflectivity variation between the "on" and "off" envelopes is lower than the actual variation between the peak value during the "on" envelope and the "off" value. This is illustrated in Fig. 5.7, in which the top image shows the pulsed signal to the device and the bottom image shows both the actual peaked response of the laser and the time-averaged quantity measured by the CCD during the capture of the I_1 frame. The actual peak value (here 2.75 K) is typically the temperature of interest, while the

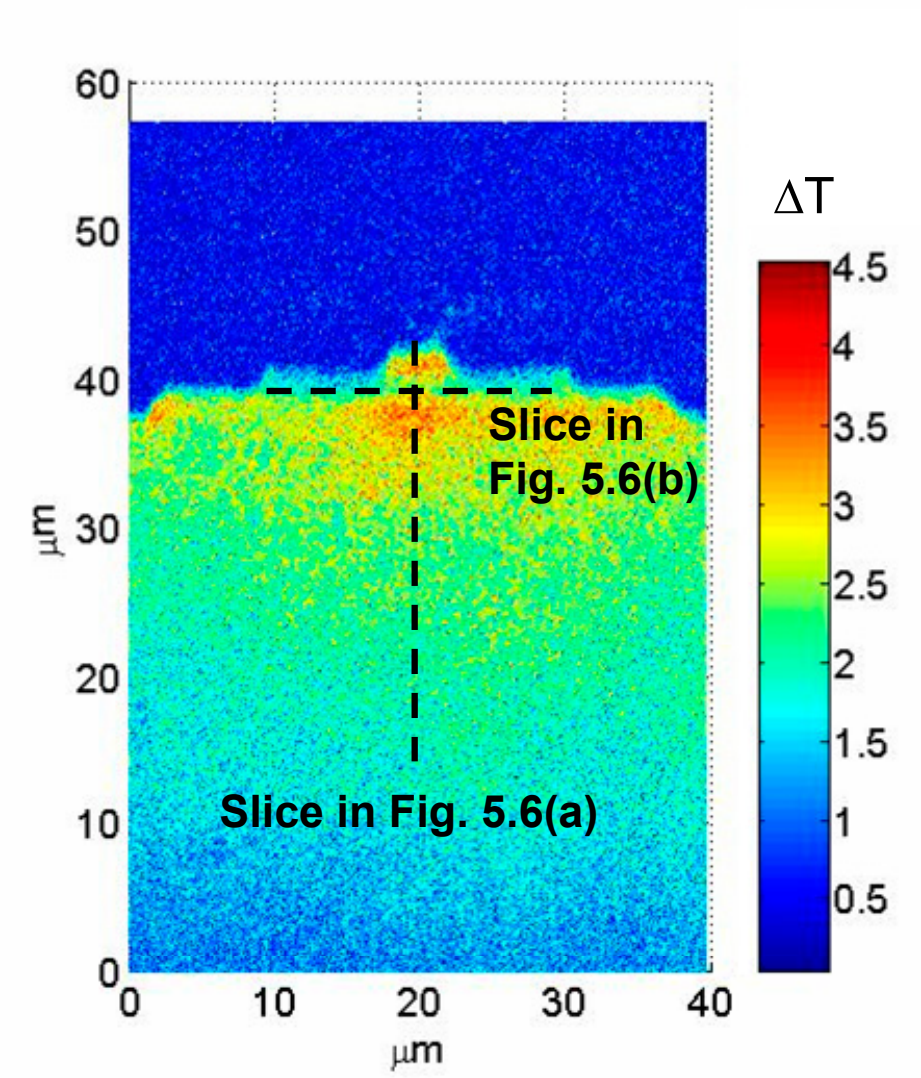

Fig. 5.5: Thermoreflectance image of the peak temperature of a InGaAs QD laser under bias at 120 mA, 10 kHz, and 90% duty cycle.

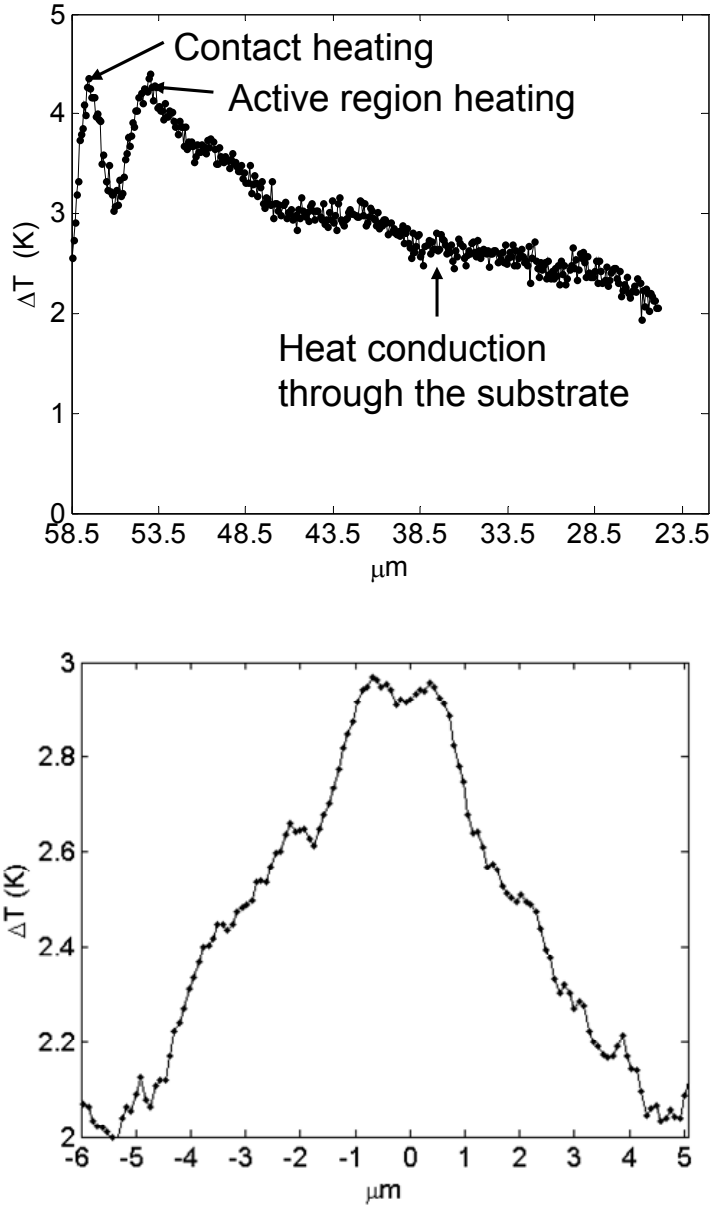

Fig. 5.6: Vertical (top) and horizontal (bottom) cross-sections of the peak temperature for bias at 10 kHz, 90% duty cycle, and 120 mA.

measured temperature is 1.4K, an error of almost 50%. In order to eliminate this error, a conversion factor which is based on the area ratio of the gray and red regions in Fig. 5.7 is used to convert the measured signal into the actual value. This conversion factor has been applied to calculate the peak temperature during pulsed operation for Figures 5.5 and 5.6.

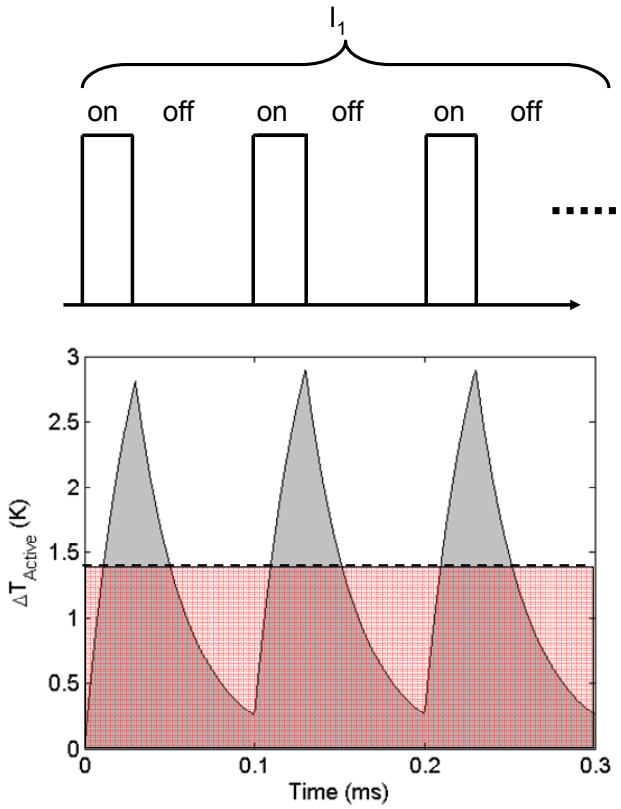

Fig. 5.7: (Top) Current pulse train sent to the laser diode. (Bottom) Actual temperature response of the active region (gray) and the measured time-averaged response (red-shaded).

5.5 Thermal relaxation time constant

The active region temperature of the laser diode during the on and off periods of pulsed operation can be written (respectively) as

$$T = (T_{on} - T_{off})(1 - e^{-t/\tau_{th}}) + T_{off} \tag{5.2}$$

and

$$T = (T_{on} - T_{off})e^{-t/\tau_{th}} + T_{off} \tag{5.3}$$

As conveyed in Eq. (5.2), while the device is turned on by the current pulse, the temperature increases and approaches T_{on}, the steady state "on" temperature under DC operation. T_{off} is the temperature while the laser is off (typically the heat sink temperature). The thermal relaxation time constant τ governs the temperature response to the current pulse and therefore can set the range of duty cycles and frequencies for which a device is able to operate. The smaller the value of τ, the smaller the amount of time required for the laser diode to achieve the steady state temperatures T_{on} and T_{off}. Fig. 5.8 shows the laser diode active region temperature at 10kHz bias obtained by Eqs. (5.3) and (5.4) assuming two different thermal relaxation time constants and apply in Eq. (5.2) and Eq. (5.3). T_{on} was measured using low frequency thermoreflectance; since the laser light power is in this case a small fraction of the total bias power, the fact that the laser does not turn on for low bias measurements is not expected to impact the measured value of T_{on}. As shown in Fig. 5.9, the value of τ for this device can be derived as approximately 30 μs by fitting at various duty cycles.

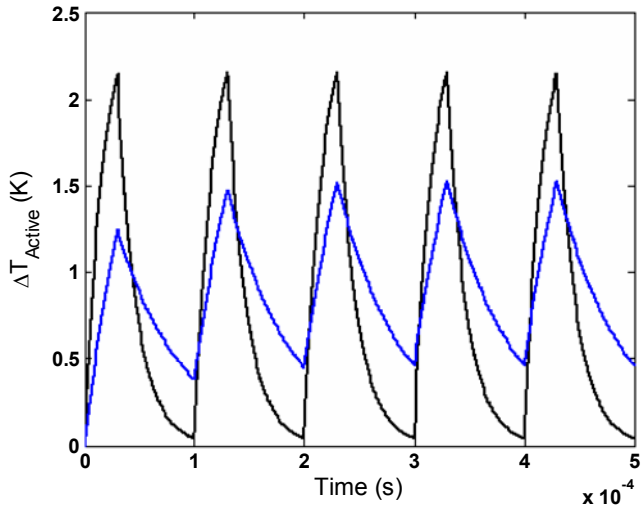

Fig. 5.8: Active region temperature at 10kHz bias with different assumed thermal relaxation time constants. The dark line is the thermal response assuming a τ of 4 μs, and the blue line is the thermal response assuming a 40 of μs.

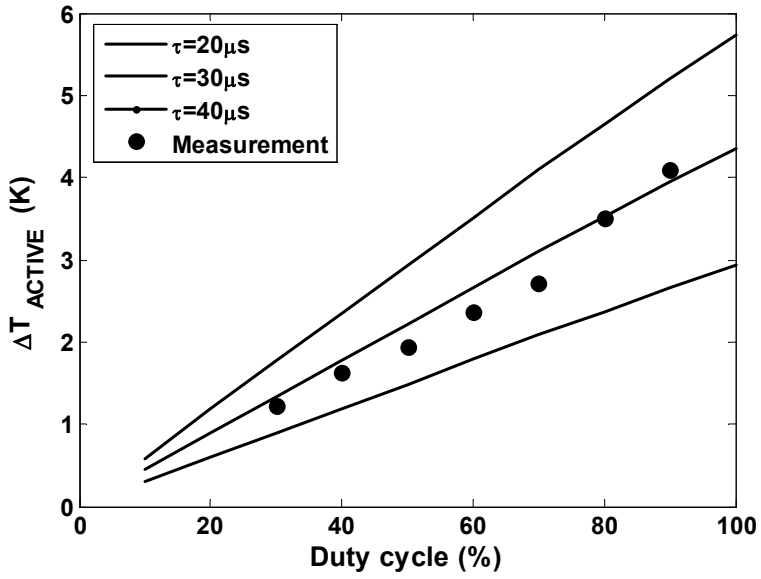

Fig. 5.9: Experimental and simulated results of active region temperature at different thermal relaxation time constants as a function of duty cycle. The thermal relaxation time of the device is observed to be approximately 30μs.

5.6 Summary

Modern communications electronics require devices to be modulated at high frequencies that may vary from kHz to GHz. Since the capability of a typical commercial-grade CCD camera is only approximately 100 frames per second, the thermoreflectance setup described in Chapter 2 cannot measure temperature variation at the bias frequencies relevant for pulsed device operation. In this chapter we have described a modified thermoreflectance measurement that enables CCD-based thermoreflectance to be applied directly at high modulation frequencies and at different duty cycles, applying this modified setup to a λ=1.1μm InGaAs quantum dot laser biased at 10kHz. A time-dependent temperature model was used to translate the measured time-averaged thermoreflectance signal into the peak value during modulation (a quantity more relevant for device characterization), and also to derive the thermal relaxation time constant.

Chapter 6

Pentacene thin film transistor characterization by microscale thermal measurement

6.1 Introduction

Since the first demonstration of low voltage organic light emitting devices (OLEDs) by Tang et al. in 1987 [96], organic electronics have received considerable research attention. Devices such as organic photovoltaics (OPVs) [97], organic bistable memories [98], organic bimolecular sensors [99] and organic thin film transistors (OTFTs) [100] have been successfully fabricated and realized. Most of the advantages of organic devices over inorganic devices stem from manufacturing concerns such as board area fabrication, lower vacuum requirements, lower production cost, and the ability to fabricate devices on flexible or nonplanar substrates such as cyclic olefin copolymer (COC) [101], polymer fibers [102], and scanning cantilever probes [103].

Among organic devices, OTFTs play a very important role analogous to MOSFETs in inorganic integrated circuits, i.e. as amplifiers, current sources, or logic elements. Below, we demonstrate how to use thermal and thermoelectric measurements to evaluate the material properties of a pentacene-based OTFT, specifically characteristics such as channel thickness and trap density that are critical to its carrier mobility and overall performance.

6.2 Carrier transport in pentacene

Although transport models in organic materials are not as developed as in inorganic materials, it has been suggested that hopping mechanisms can also be used to describe carrier transport in small-molecule amorphous organic thin films. [104-107]. Using the Miller-Abraham model of the hopping processes, the carriers (electrons and holes) of the organic semiconductor are transported from initial to final states by absorbing or releasing phonons [107]. Fig. 6.1 illustrates the hopping mechanism in organic amorphous materials. Once a carrier absorbs a phonon to move to an energy level (escape energy) that favors tunneling, it will tunnel to a final state, emitting phonons to release excess energy. Since the amorphous film does not have crystalline structure, it does not have a well-defined reciprocal lattice and reciprocal primitive vectors; hence the traditional (inorganic) density of states expression and band structure description are no longer valid. However, the film does have electronic structure

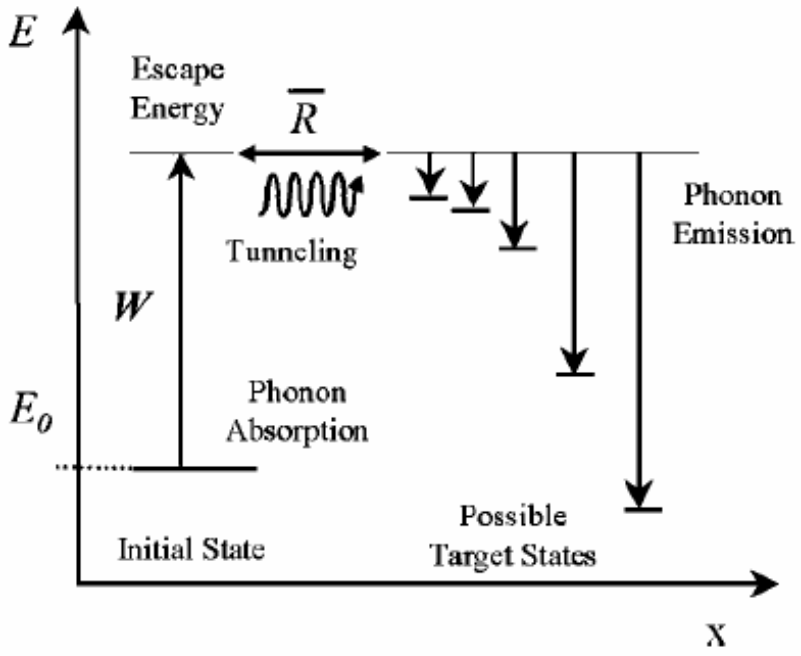

Fig. 6.1: Hopping transport mechanism in organic materials, according to the Miller – Abraham model [101].

similar to the valence and conduction bands in inorganic semiconductors; here the energy levels are distributed near the highest occupied molecular orbital (HOMO) and lowest unoccupied molecular orbital (LUMO) according to a Gaussian-like function, [108,109],

$$D(E) = \frac{\rho_0}{\sqrt{2\pi\sigma_0^2}} e^{-\frac{E^2}{2\sigma_0^2}} \tag{6.1}$$

where ρ_0 is the density of molecules and σ_0 is the standard deviation of the distribution. The carrier density of states distributions near the HOMO and LUMO are shown in Fig. 6.2. The total carrier concentration can then be written familiarly as

$$n = \int_{-\infty}^{+\infty} D(E) \frac{1}{1 + e^{\frac{E - E_F}{kT}}} dE \tag{6.2}$$

where E_F is the Fermi level of the carriers. Similarly, if the mobility (μ) as a function of energy is known, the electrical conductivity of the carriers can be obtained by

$$\sigma = \int_{-\infty}^{+\infty} qn(E)\mu(E)dE \tag{6.3}$$

where $\mu(E)$ is the carrier mobility and q is the fundamental electric charge. The average energy transported by carriers participating in conduction can then be written as

$$E_{trans} = \frac{\int_{-\infty}^{+\infty} E\sigma(E)dE}{\int_{-\infty}^{+\infty} \sigma(E)dE} \tag{6.4}$$

The density of states (DOS), carrier concentration, mobility, and conductivity as a function of energy are shown in Fig. 6.3. The thermoelectric Peltier coefficient (in units of volts) is defined by the energy transported by conducting carriers with respect to the Fermi energy; from Eq. (6.4) we obtain the Peltier coefficient (Π) [110]:

$$\Pi = -\frac{1}{q}\int_{-\infty}^{+\infty} \left(E - E_f\right)\frac{\sigma(E)}{\sigma}dE \tag{6.5}$$

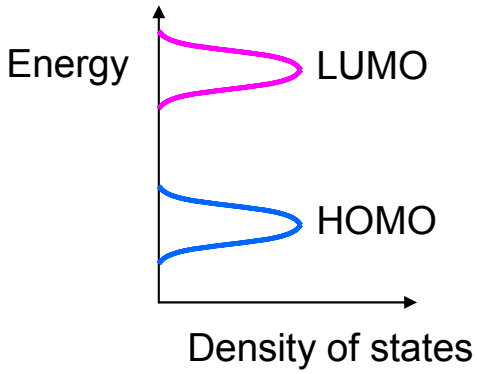

Fig. 6.2: The carrier density of states at the HOMO and LUMO levels of an organic semiconductor.

The thermoelectric Seebeck coefficient is then defined as the Peltier coefficient divided by the absolute temperature:

$$S = \frac{\Pi}{T} = \frac{E_F - E_{trans}}{qT} \tag{6.6}$$

In the following section, we will discuss how to use the thermoelectric effect (Seebeck coefficient) to characterize the material properties of an organic thin film.

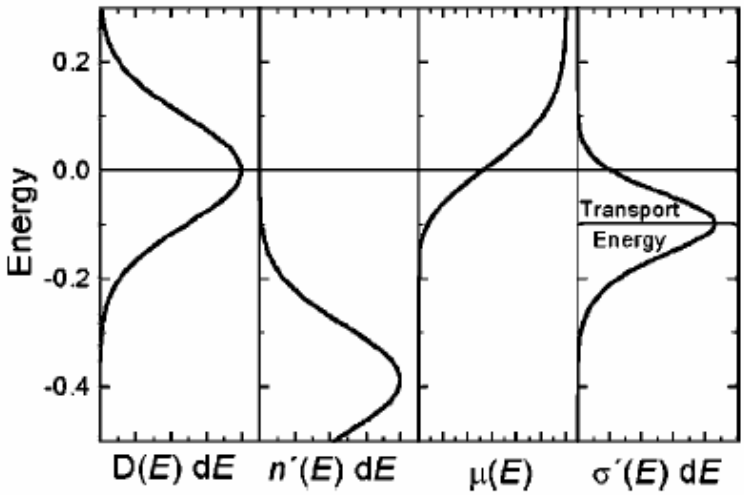

Fig. 6.3: Density of states (DOS), carrier concentration, mobility, and conductivity as a function of energy [107].

6.3 Derivation of transistor channel thickness and carrier concentration

Pentacene organic thin film transistors have been the subject of much study in the last decade, during which time several different type of substrates (such as silicon, plastic, and metal) and dielectric materials have been successfully applied [111,112,113]. The highest mobility attained is on the order of 1 cm^2/Vs for polycrystalline pentacene [114].

In general, the mobility has been shown to depend a number of parameters, including the dielectric treatment [115], pentacene film thickness [116], deposition temperature, electrodes, and operating environment. It is also believed that only first several monolayers of pentacene deposited on top of the dielectric material actually contribute to transistor operation. Measurements by Ruiz *et al.* indicate that the field effect mobility does not vary once the pentacene thickness becomes larger than 6 monolayers (MLs) [117]. Similarly, Muck et al verified that the mobility of an OTFT based on dihexylquaterthiophene (DH4T) clamped after the DH4T thickness became more than 2 ML [118]. These measurements indicate that the mobility of an organic thin film is critically dependent on the material properties directly at the interface to the dielectric.

Silicon dioxide is a commonly used gate dielectric in OTFTs [119]. When a pentacene film is deposited on SiO_2, the hydroxyl group on the SiO_2 induces charges at the interface, resulting in a large positive threshold voltage for the OTFT [120].The linear operating region of the transistor is modeled by:

$$I_{DS} = \frac{W}{L} C_i \mu_0 V_{DS} \left(V_G - V_{th} - \frac{V_{DS}}{2} \right) \tag{6.7}$$

where W and L are the channel width and length respectively, C_i is the capacitance per unit area of the insulating layer, μ_0 is the carrier mobility (the upper limit of the field effect mobility when all the carriers induced by the gate bias are free carriers), V_{DS} is the drain source voltage, V_G is the gate voltage, and V_{th} is the threshold voltage. When V_{DS} is much smaller than $V_G - V_{th}$, Eq. (6.7) can be approximated by

$$\frac{I_{DS}}{V_{DS}} \frac{L}{W} = qP\mu_0 \tag{6.8}$$

where P is the areal free carrier density [cm^{-2}] induced by the gate bias and is given by $P=(V_G-V_{th})C_i/q$ [121]. The left hand side of Eq. (6.8) can be further simplified to yield

$$\sigma t_{ch} = qP\mu_0 \tag{6.9}$$

where t_{ch} is the thickness of the channel in which carrier transport occurs. The mobility μ_0 obtained in Eq. (6.9) is also known as the Seebeck mobility, which is the highest mobility that the transistor can achieve given that all the induced carriers are mobile and drifting at the transport energy level [122]. However, due to the presence of traps along the channel, the measured field effect mobility (μ_{FE}) in the linear region is lower than the Seebeck mobility:

$$\sigma t_{ch} = q(P + P_{tr})\mu_{FE} = qP\mu_0 \tag{6.10}$$

where P_{tr} is the trap density in the channel and can be written as [115]

$$P_{tr} = \frac{(V_{th} - V_{turn-on})C_i}{q} \tag{6.11}$$

Next we show that the density of free carriers P can be obtained by a measurement of the Seebeck coefficient. Since the free carriers are assumed to be at the transport energy level E_{trans} defined by Eq. (6.4), and the effective density of states can be assumed to be the molecular density of pentacene (assuming each molecule is contributing to one transport state), the volumetric carrier density in the channel can be written using Maxwell-Boltzmann statistics as [123]

$$\frac{P}{t_{ch}} = N_m e^{-\frac{E_F - E_{trans}}{kT}} = N_m e^{-\frac{qS}{k}} \tag{6.12}$$

where N_m is the molecular density (2.9×10^{21} cm^{-3} for pentacene). By measuring the Seebeck coefficient (S), field effect mobility (μ_{FE}), and trap density (P_{tr}) of the device,

Eqs. (6.10) and (6.12) can be solved simultaneously to evaluate the transistor channel thickness and the free carrier density. The next sections will describe how we fabricate an OTFT and measure these quantities.

6.4 OTFT fabrication

The OTFT under study uses a heavily doped n-type silicon substrate (<0.005 Ω cm) and 200nm thermal silicon dioxide as gate and gate insulator respectively. The susbtrate is prepared by a regular solvent cleaning procedure: 10 minutes DI water, 10 minutes acetone, 10 minutes tricholoroethylene, 10 minutes methanol, 5 minutes boiling methanol, and finally 20 minutes oxygen plasma cleaning. Substrates are then loaded into a thermal evaporation chamber, and pentacene deposition is performed at 5×10^{-7} Torr. The pentacene used in the experiment is purchased from Aldrich Inc. and purified by a temperature gradient sublimation approach [124]. The deposition rate of the pentacene is in the range of 0.1Å/s to 0.3Å/s. The gold source and drain top contacts are deposited using a shadow mask at a rate of 0.5Å/s. The channel length (L) and width (W) defined by the shadow mask are 75μm and 1000μm respectively.

6.5 Method and results for measurement of Seebeck coefficient, trap density, and channel thickness

Electrical measurements including I_{DS} vs. V_{DS} and I_{DS} vs. V_G are measured by an HP semiconductor parameter analyzer (4146B). All the measurements are performed

under dark and ambient conditions. The drain current vs. drain source voltage at different gate biases is plotted in Fig. 6.4. It can be noticed that the channel does not become completely depleted at zero gate bias voltage. Similar phenomena have been reported by other groups [125,126,127] and it is believed that the electron-trapping hydroxyl group attracts the electrons of the pentacene and leaves holes (the primary conducting carrier in pentacene) in the channel even when the gate bias is zero [120].

The Seebeck coefficient of the device is measured by placing the transistor on a homemade temperature controlled stage having one thermoelectric heater and one thermoelectric cooler as described in Section 1.4. The temperature differences across the heater and cooler are monitored by microthermocouples; a measured temperature difference of $\Delta T = 1.5K$ generated by the heater and cooler is used for the Seebeck coefficient measurement. Fig. 6.5 shows the thermal voltage response of the pentacene when the heater and cooler are switched on. The thermal voltage is plotted as a histogram and fit by two Gaussian curves as shown in Fig. 6.6. The Seebeck coefficient at different thicknesses is plotted in Fig. 6.7. The error is evaluated based on the standard deviation of the Gaussian fit.

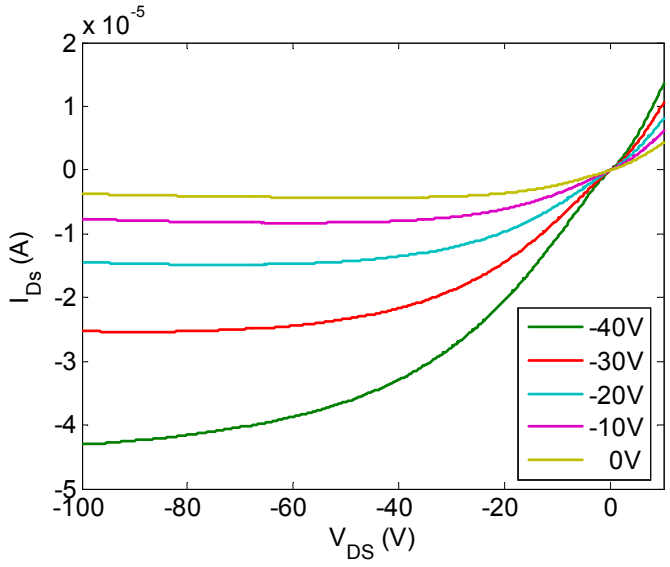

Fig. 6.4: I_D vs. V_{DS} at different gate voltage biases (-40V to 0V).

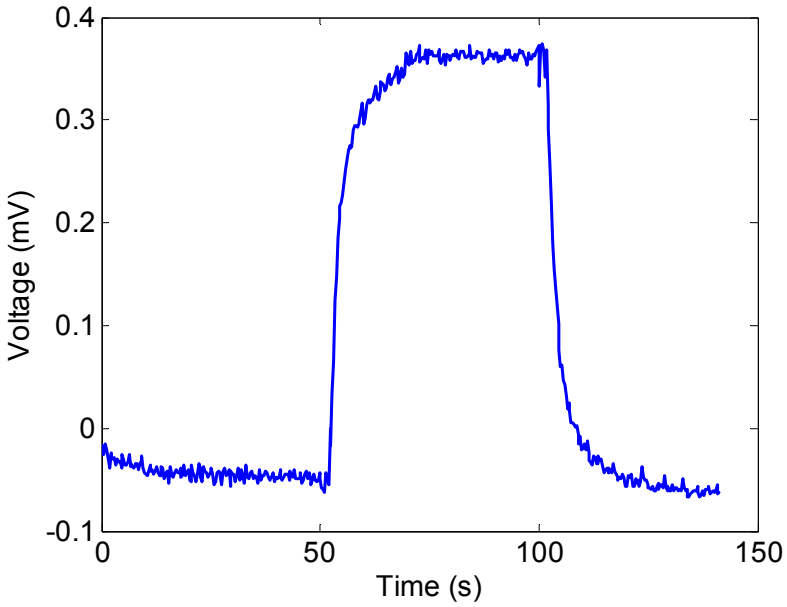

Fig. 6.5: Measured thermal voltage response of a 50nm pentacene thin film transistor to a ΔT of 1.5K.

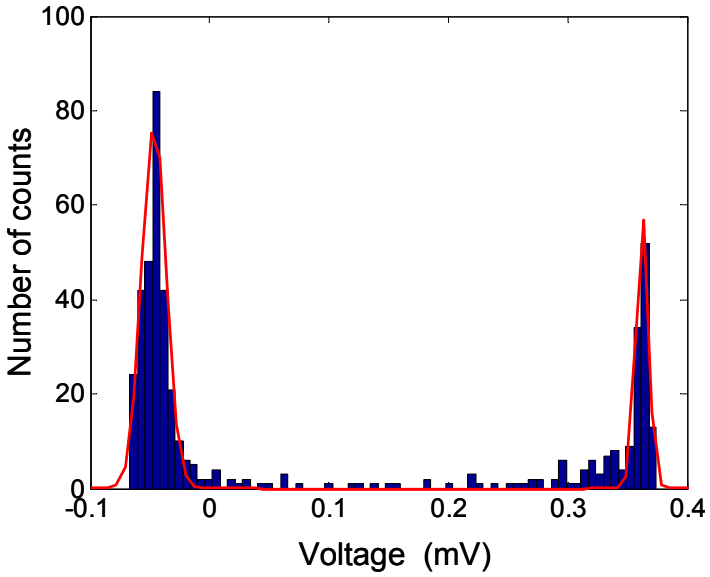

Fig. 6.6: Histogram plot of the thermal voltage in Fig. 6.5 measured over time. The red line represents the two best fit Gaussian curves.

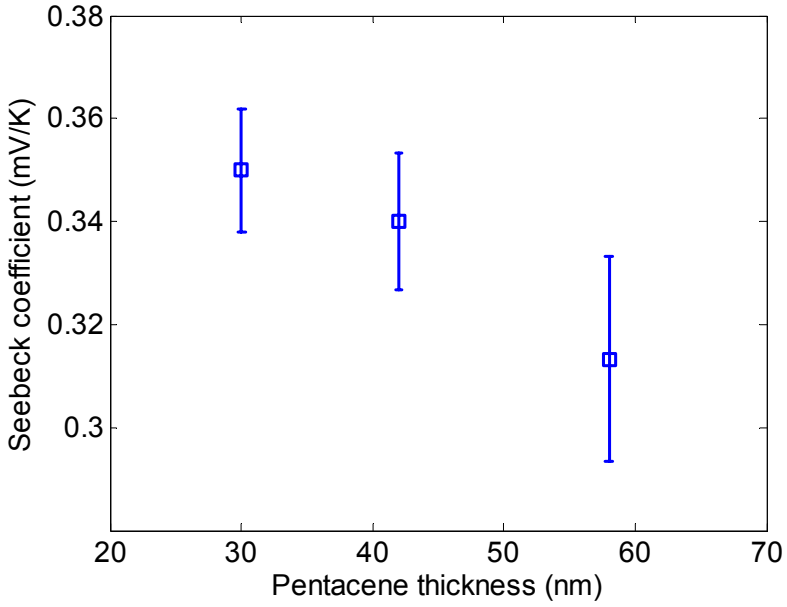

Fig. 6.7: Measured Seebeck coefficient of the pentacene thin films at different thicknesses. The error bars represent the standard deviation values obtained in the Gaussian fitting of Fig. 6.6.

By plotting $\sqrt{I_d}$ against Vg, the threshold voltage (V_{th}) can be obtained as the x-axis intercept. Similarly, the turn on voltage can be obtained by plotting I_D against V_G on a log scale and locating the voltage at which the source-drain current starts to show exponential behavior. Knowing the threshold voltage, turn on voltage, and capacitance per unit area of the 200Å silicon dioxide ($C_i = 2\times10^{-8}$F/cm^2) , the trap density P_{trap} can be estimated by Eq. (6.11). The measured/derived values of σ, V_{th}, $V_{turn\ on}$, S, P_{trap} and μ_{FE} are shown in Table 6.1. By solving Eqs. (6.10) and (6.12), the channel thickness of the transistor can be obtained (Fig. 6.18).

Pentacene thickness	16nm	30nm	58nm
Threshold voltage (V_{th})	89.1 V	83.3 V	53.2 V
Turn on voltage ($V_{turn\ on}$)	93.8 V	92.4 V	70.6 V
Trap density (N_{trap})	5.0×10^{11} cm^{-2}	9.7×10^{12} cm^{-2}	1.8×10^{12} cm^{-2}
Seebeck coefficient (S)	0.36 mV/K	0.35 mV/K	0.31mV/K
Mobility	0.09 cm^2/Vs	0.07 cm^2/Vs	0.02 cm^2/Vs

Table 6.1: Threshold voltage, turn on voltage, trap density, Seebeck coefficient and mobility of the pentacene OTFT at different pentacene film thicknesses.

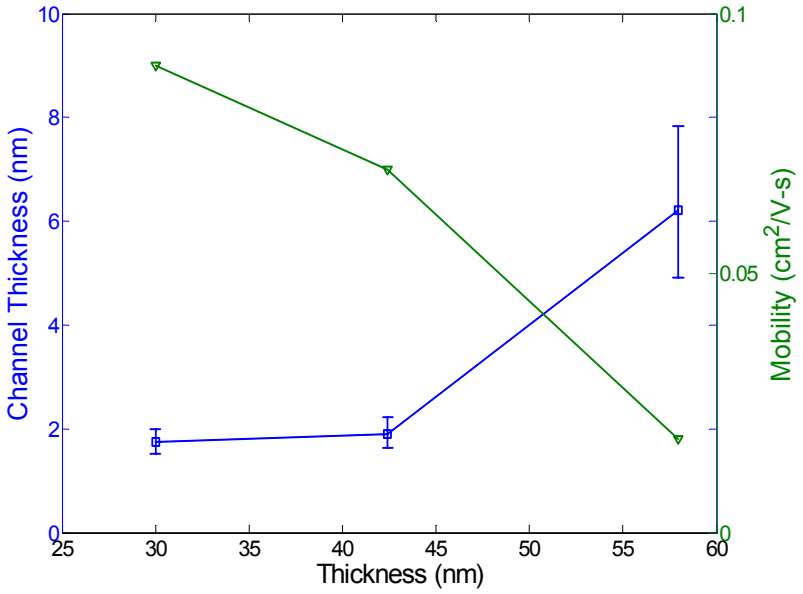

Fig. 6.8: Field effect mobility and transistor channel thickness as a function of pentacene film thickness.

6.6 Summary

Transport in OTFTs is critically dependent on carrier transport in the channel that lies at the interface to the gate dielectric. Here we have shown that thermal and thermoelectric measurements can be applied to characterize the channel thickness of a pentacene OTFT. The measured transistor channel thickness shows a linear relation with film thickness and suggests that only the first 3 monolayers (1 monolayer = 15nm) contribute to the transport properties of the transistor. The demonstrated thermoelectric Seebeck measurement technique allows direct and non-destructive elevation of channel thickness without any extra fabrication steps or modification of the device.

Chapter 7

Conclusion and suggestions for future work

7.1 Summary of present work

The objective of the work presented in this thesis is to develop a high resolution thermal imaging technique that is suitable for noninvasive temperature measurements on electronic devices including laser diodes and transistors. These two devices in particular are commonly used in modern processors and communication systems, and both face challenges due to heat generation. For transistors, thermal problems arise due to the ever-shrinking size of the device, which must dissipate heat into a smaller and smaller volume. For lasers, thermal problems often arise due to high-power operation and may catastrophically destroy the device. In order to study and understand these problems, an important step is to measure temperature at small size scales. Here we have shown how CCD-based thermoreflectance temperature measurement can be successfully applied to heterojunction bipolar transistors,

quantum well lasers, and quantum dot lasers for device thermal characterization. Indeed, the high spatial resolution of this technique allows one to resolve separate heat sources within a device itself, rather than viewing the entire device as a monolithic heat source, thus enabling study of the separate heat transport mechanisms that often exist within a device.

Specifically, in applying CCD-based thermoreflectance to SiGe-based heterojunction bipolar transistors, we showed how temperature mapping can be used to spatially profile device current, including asymmetric behavior such as current hogging. In examining a type of high-power laser (a slab coupled optical waveguide lasers), we showed how (with proper light filtering) 2D temperature profiles of the facet can be measured. Such profiles are important for studying laser reliability and potentially examining defects that may later trigger COD. Because the spatial resolution of the technique allows us to image the temperature gradients within the device itself, we were able to translate the temperature profile to a map of refractive index change, using a finite element optical mode solver to predict thermal lensing behavior. The predicted behavior correlated well with direct beam measurements, providing support for the accuracy of the thermal measurement technique. We then described how we modified the CCD-based thermoreflectance setup to accommodate pulsed devices, demonstrating the technique on pulsed InGaAs quantum dot lasers. Imaging the facets of these lasers, we could identify separate temperature peaks due to active region heating and contact heating, as well as a gradual temperature decline into the substrate representing heat conduction. With these measurements, we were

able to derive the thermal time constant of the device, an important parameter that can in some cases determine a laser's maximum pulse rate and duty cycle.

Finally, we discussed how the measurement of thermal and thermoelectric properties in organic thin films can be used to derive fundamental and device-relevant electrical properties related to interface transport. By measuring the Seebeck coefficient of an OTFT, we showed that one can successfully evaluate the channel thickness in non-destructive fashion without further fabrication processes.

7.2 Future work

Below we discuss several directions in which the current work could be extended.

Thermotransmittance for transparent materials

One limitation of the thermoreflectance technique is that it requires the material itself to be reflective, i.e. it can only be applied on opaque materials such as semiconductors and metals. To make the setup applicable to transparent materials such as fluids, small molecular weight organic materials, and bio-materials, the experimental setup has to be modified to perform a thermotransmittance measurement. In such as setup, the CCD camera which captures the four images is placed on the opposite side of the sample from the illuminating light source. Fig. 7.1 illustrates the setup and thermotransmittance signal detection.

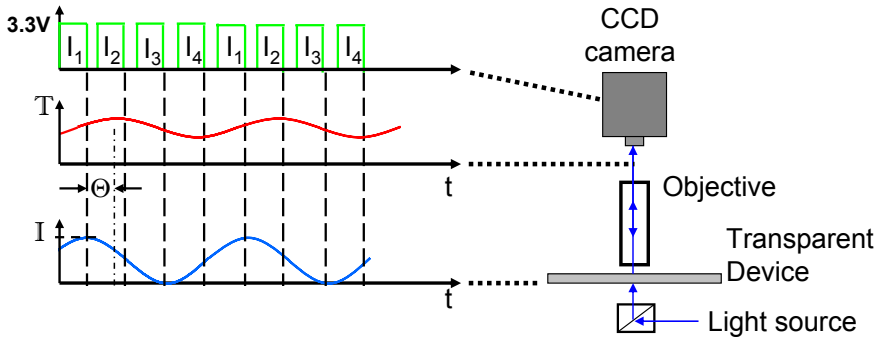

Fig. 7.1: Schematic of the thermotransimattance working principle. In similar fashion to thermoreflectance, the bias signal is sent to the device (blue), the external trigger signal is sent to the CCD camera (green), and the transmittance signal is captured by the CCD camera (red).

Monochromator light source thermoreflectance

The devices under study here, as well as many others, are composed of a number of different semiconductors and metals that 1) have different thermoreflectance coefficients for the same wavelength illumination, and 2) have their peak thermoreflectance signals at different wavelengths. By using a monochromator, one could sweep through a range of illumination wavelengths and more easily examine different materials within a given device.

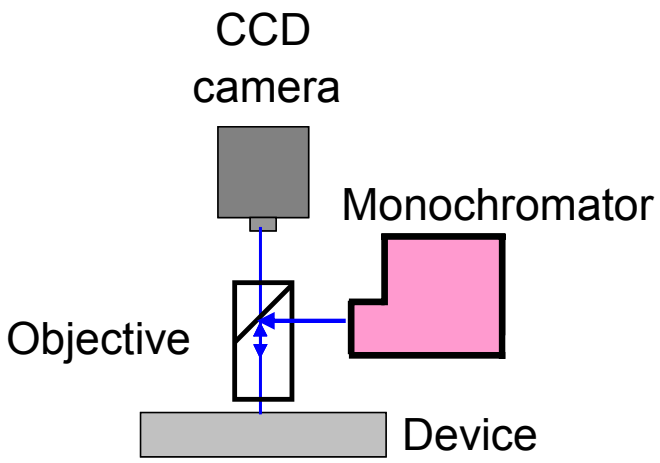

Fig. 7.2: A schematic of a CCD-based thermoreflectance setup using a monochromatic filter on a broad-band light source.

Ultraviolet light source thermoreflectance

Since the spatial resolution of the CCD-based thermoreflectance setup is limited by the far field diffraction limit, the spatial resolution limit can be improved by using smaller wavelength illumination such as ultraviolet (UV) light. This improved thermoreflectance setup could allow accurate measurement of thermal boundary resistances across smaller feature sizes such as found in superlattices. For performing CCD thermoreflectance with UV light, a number of experimental components have to be modified, although commercial parts do exist for a high power UV objective (Mitutoyo UV series), a UV CCD camera (JAI Inc) and a UV laser at 266nm (CrystaLaser).

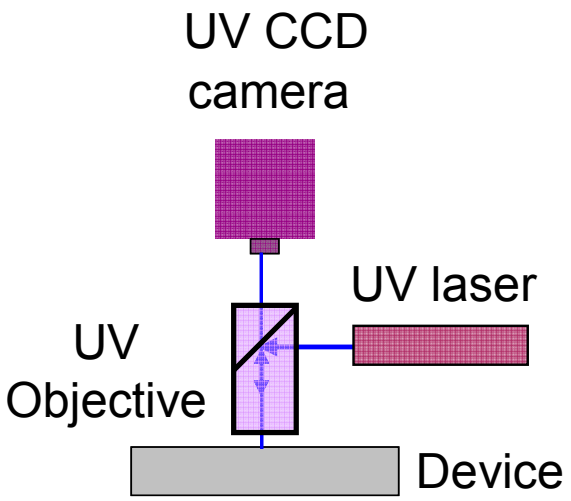

Fig. 7.3: A schematic drawing of a UV CCD-based experimental setup.

Bibliography

[1] International Technology Roadmap for Semiconductors (ITRS)

[2] Pop, E. and Goodson, K. E., 2006. "Thermal phenomena in nanoscale transistors", *J. Electron. Packaging,* **128**, pp. 102 - 108.

[3] Kaviany, M.,Heat transfer physics, unpublished.

[4] Jhon, M. S., Escobar, R. A., Ghai, S. S. and Amon, C. H., 2006. "Multi-length and time scale thermal transport using the lattice Boltzmann method with application to electronics cooling", *J. Heat Mass Transfer,* **49**, pp.97 – 107.

[5] Yang, R. and Chen, G., 2004. "Thermal conductivity modeling of periodic two-dimensional nanocomposites", *Phys. Rev. B*, **69**, 195316-1 – 195316- 10.

[6] Brozak, G., Helm, M., DeRosa, F., Perry, C. H., Koza, M., Bhat, R. and Allen Jr., S. J., 1990. "Thermal saturation of band transport in a superlattice", *Phys. Rev. Lett*., **64**, pp. 3163 -3166.

[7] E. Pop, S. Sinha, K. E. Goodson, 2006. " Heat Generation and Transport in Sub-90 nm Transistors", *Proceeding of IEEE*, **94**, pp. 1587 – 1601.

[8] Walker, C.L.; Bryce, A.C. and Marsh, J.H., 2002. "Improved catastrophic optical damage level from laser with nonabsorbing mirrors". *IEEE Photonic. Technol. Lett*., **14**, 1394-1396.

[9] Shingaya Y., Nakayamaa T. and Aono M., 2002. "Carbon nanotube tip for scanning tunneling microscopy", *Physica B: Condensed Matter*, **323**, pp. 153-155.

[10] Cheung C. L., Hafner J. H. and Lieber C. M., 2000. "Carbon nanotube atomic force microscopy tips: Direct growth by chemical vapor deposition and application to high-resolution imaging". *PNAS*, **97**, pp. 3809 – 3813.

[11] She J.C., Xu N. S., Deng S.Z., Chen J., Bishop H., Huq S. E., Wang, L., Zhong D.Y. and Wang E.G., 2003. "Vacuum breakdown of carbon-nanotube field emitters on a Silicon tip". *Appl. Phys. Lett*., **87**, pp. 2671 – 2673.

[12] Huang N. Y., She J. C., Chen J., Deng S. Z., Xu N. S., Bishop H., Huq S. E., Wang L., Zhong D. Y., Wang E. G. and Chen D. M., 2004. "Mechanism Responsible for Initiating Carbon Nanotube Vacuum Breakdown". *Phys. Rev. Lett*., **93**, 075501-1 – 075501-4.

[13] Zhou, X., He, J., Liao, L. S., Lu, M., Ding, X. M., Hou, X. Y., Zhang, X. M., He, X. Q. and Lee, S.T., 2000. "Real-time observation of temperature rise and thermal breakdown processes in organic LEDs using an IR imaging and analysis system", *Adv. Mat*., **12**, pp. 265 – 659.

[14] Pipe K. P. and Ram R. J., 2003. "Comprehensive heat exchange model for a semiconductor laser diode", *IEEE Photon. Technol. Lett*., **15**, pp. 504-506.

[15] Saafi M. and Romine P., 2005. "Preliminary evaluation of MEMS devices for early age concrete property monitoring". *Cem. Concr. Res*., **35**, 2158-2164

[16] Shi L., Plyasunov S., Bachtold A. and McEuen P. L., 2000. “Scanning thermal microscopy of carbon nanotubes using batch-fabricated probes”. *Appl. Phys. Lett*., **77**, pp. 4295-4297.

[17] Chan P. K. L., Pipe K. P., Qin G. and Ma Z., 2006. “Thermoreflectance imaging of current dynamics in high power SiGe heterojunction bipolar transistors”, *Appl. Phys. Lett.,* **89**, pp. 233521-1 - 233521-3.

[18] Nenna G., Flaminio G., Fasolino T., Minarini C., Miscioscia R., Palumbo D. and Pellegrino M., 2007. “A Study on Thermal Degradation of Organic LEDs Using IR Imaging”. *Macromol. Symp.*, **247**, pp. 326 – 332.

[19] Tan H., Kamath, K. K., Mi, Z., Bhattacharya P. and Klotzkin D., 2006. “Analysis of the reduced thermal conductivity in InGaAs/GaAs quantum dot lasers from chirp characteristics”. *Appl. Phys. Lett*., **89**, pp. 121116-1 – 121116-3.

[20] Marone, M.J. and Payne, J.E., 1997. “An ac microcalorimeter employing a diode laser as a heater”. *Rev. Sci. Inst*., **68**, pp. 4516-4520.

[21] Shi, L., Kwon, O., Miner, A., and Majumdar, A., 2001. "Design and Batch Fabrication of Probes for Sub-100 nm Scanning Thermal Microscopy," *J. Microelectromechanical Systems*., **10**, pp. 370 – 378.

[22] Luo, K., Herrick, R.W., Majumdar A. and Petroff, P., 1997. “Scanning thermal microscopy of a vertical-cavity surface-emitting laser”. *App. Phys. Lett*., **71**, 1604-1606.

[23] Zhou J. and Shi L., 2005. " Scanning Thermal Microscopy of Carbon Nanotube Electronic Devices", *2005 IEEE Twenty First Annual IEEE Semiconductor Thermal Measurement and Management Symposium*, pp. 303-306.

[24] Fiege G. B. M., Niedernostheide F. J., Schulze H. J., Barthelmeg R. and Balk L. J., 1999. "Thermal Characterization of Power Devices by Scanning Thermal Microscopy Techniques". *Microelectron. Reliab*. **39**, 1149-1152.

[25] Mills G., Zhou H., Midha A., Donaldson L., and Weaver J. M. R., 1998. "Scanning thermal microscopy using batch fabricated thermocouple probes". *App. Phys. Lett*., **72**, 2900-2902.

[26] Xie Z., Han L., Wei, Wang X., Gu Y. and Chen H., 2000. "An application of scanning thermal microscopy: mapping near field light-emission of a QW laser diode in operation*". Mater. Sci. Eng. A*, **292**, pp. 179-182.

[27] Bundasa J., Patnaudea K., Dennisa R., Burrowsa D., Cooka R., Reisingera A., Sundarama M., Bensonb R., Woolawayc J., Schlesselmannc J. and Petroni S., 2006. "Two-color quantum well infrared photodetector focal plane arrays". *Proc. of SPIE*, **6206**, pp. 62060G-1 - 62060G-11.

[28] Pierret, R. F., 1996. *Semiconductor device fundamentals*. Addison Wesley.

[29] Singh, J., 2003. *Electronic and Optoelectronic Properties of Semiconudctor Structures*, Cambridge.

[30] Varshni Y. P., 1967. "Temperature dependence of the energy gap in semiconductors", *Physcia*, **3**4, pp. 149-154.

[31] Pankove J. I., 1975. *Optical Processes in Semiconductor*, Dover, New York.

[32] Lüerßen D., Ram R and Hudgings J., 2005. "Radial Temperature Profiling of VCSELs*". Conference on Lasers & Electro-Optics (CLEO)*, **2**, pp. 1378-1380.

[33] Lüerßen D., Hudgings J. and Mayer P. and Ram R., 2005. "Nanoscale thermoreflectance with 10mK temperature resolution using stochastic resonance". *2005 IEEE Twenty First Semiconductor Thermal Measurement and Management Symposium*, pp. 253-258.

[34] Tessier G., Holé S. and Fournier D., 2003. "Ultraviolet illumination thermoreflectance for the temperature mapping of integrated circuits". *Opt. Lett.*, **28**, pp. 875-877.

[35] Epperlein P. W., 1993. "Micro-temperature measurements on semiconductor laser mirrors by reflectance modulation: A newly developed technique for laser characterization". *Jpn. J. Appl. Phys*., **32**, 5514 – 5522

[36] Mayer P. M., Ram R., 2006. "Cross-plane Thermoreflectance Imaging of Thermoelectric Elements", *Mater. Res. Sco. Symp. Proc.*, **886**, pp. F10-06.1-F10-06.6

[37] Ezzahri Y., Dilhaire S., Grauby S., Rampnoux J. M., Claeys W., Zhang Y., Zeng G., and Shakouri A., 2005. "Study of thermomechanical properties of Si/SiGe superlattices using femtosecond transient thermoreflectance technique". *Appl. Phys. Lett.*, **87**, pp. 103506-01 103506-03.

[38] Carolyn A. Paddock and Gary L. Eesley, 1986. "Transient thermoreflectance from thin metal films". *J. Appl. Phys*., **60**, 285-290.

[39] Smith A. N. and Norris P. M., 2001. "Influence of intraband transitions on the electron thermoreflectance response of metals". *Appl. Phys. Lett*., **78**, pp. 1240-1242.

[40] Stevens R. J., Smith A. N. and Norris P. M., 2005. "Measurement of thermal boundary conductance of a series of metal-dielectric interfaces by the transient thermoreflectance technique". *ASME J. Heat Trasnfer*, **127**, pp. 315-322.

[41] Dietzel, D., Röcken, H., Pelzl, J. and Bein, B. K., 2001. "Analysis of focused ion beam implantation of semiconductors by thermal microscopy", *Surf. Coat. Technol*. **142/144**. pp. 429 – 436.

[42] Brunner, M., Gulden, K., Hovel, R., Moser, M. and Ilegems, M., 2000. "Thermal lensing effects in small oxide confined vertical-cavity surface-emitting lasers", *Appl. Phys. Lett.*, **76**, pp. 7 – 9.

[43] Bennett, B. R., Soref, R. A., Del Alamo, J. A., 1990. "Carrier-induced change in refractive index of InP, GaAs, and InGaAsP", *IEEE J. Quantum Electron*., **23**, pp. 113 – 122.

[44] Grauby S., Forget B. C., Hole S. and Fournier D, 1999. "High resolution photothermal imaging of high frequency phenomena using a visible charge coupled device camera associated with a multichannel lock-in scheme". *Rev. Sci. Inst*., **70**, pp. 3603 – 3608.

[45] Fournier D., Forget B. C., Boue C. and Roger J. P., 2000. "Micron scale photothermal imaging". *International Journal of Thermal Sciences*, **39**, pp. 514-518.

[46] Anderson B. L. and Anderson R. L., 2005. *Fundamentals of Semiconductor Devices*, McGraw Hill.

[47] Wu X., Maimon S., Averett K. L., Koch M. W. and G. W. Wicks, 2003. "Emitter injection efficiency and base transport factor in InAs bipolar transistors", *Journal of Applied Physics*, **94**, pp. 5423-5425.

[48] Chand N., Fisher R., Henderson T., Klem J., Kopp W. and Morkoç H., 1984. "Temperature dependence of current gain in AlGaAs/GaAs heterojunction bipolar transistors", *Appl. Phys. Lett*., **45**, pp. 1086 – 1088.

[49] Seiler U., Koenig E., Narozny P. and Daembkes H., 1993. "Thermally triggered collapse of collector current in power heterojunction bipolar transistors". *Proceedings of the 1993 Bipolar/Bicoms Circuits and Technology*, pp. 257 - 260

[50] Liu, W., Nelson, S., Hill, D. G. and Khatibzadeh, A., 1993. "Current gain collapse in microwave multifinger heterojunction bipolar transistors operated at very high power densities". *IEEE Trans. Electron. Dev*., **40**, pp. 1917 – 1927.

[51] Chen, J. Y., Chen, C. Y., Lee, K. M., Yen, C. H., Tsai, S. F., Cheng, S. Y., Liu and W. C., 2004. "Temperature-dependent de characteristics of an InGaAs/lnGaAsP heterojunction bipolar transistor with an InGaAsP spacer and a composite-collector structure", *J. Vac. Sci. Technol. B*, **22**, pp. 2727 – 2733.

[52] Mimila-Arroyo, J. and Cabrera-Arenas, V, 2006. "Currents of the GaInP/GaAs heterojunction bipolar transistor as a function of the temperature". *Appl. Phys. Lett*., **88**, pp. 173512-1 – 173512-3.

[53] Crabbe, E.F., Cressler, J.D., Patton, G.L., Stork, J.M., Comfort, J.H. and Sun, J.Y. C., 1993. "Current gain rolloff in graded-base SiGe heterojunction bipolar transistors". *IEEE Electron Device Lett*., **14**, pp. 193 – 195.

[54] Liu W., 1995. "Thermal Coupling in 2-finger Heterojunction Bipolar Transistors". *IEEE Trans. Elec. Dev*., **42**, pp. 1033 – 1038.

[55] Zhu, Y., Kwynam, J., Yangura, M., Hasegawa, M., Hasegawa, T., Eguchi, Y., Amano Y., Suematsu, E., Sakuno, K., Matsumoto, N., Sato, H. and Hasizume, N., 2001. "Self-heating effect compensation in HBTs and its analysis and simulation". *IEEE Trans. Elec. Dev*., **48**, pp. 2640 – 2646.

[56] Huang, K.Y., Li, Y. and Lee C. P., 2004. "Computer simulation of multifinger heterojunction bipolar transistor with self-heating and thermal coupling models". *Microelectron. Eng*., **75**, pp. 137 – 144.

[57] Pomeroy, J. W., Kuball, M., l, Wallis, D. J., Keir, A. M., Hilton, K. P., Balmer, R. S., Uren, M. J., Martin, T. and Heard P. J., 2005. "Thermal mapping of defects in AlGaN/GaN heterostructure field-effect transistors using micro-Raman spectroscopy". *Appl. Phys. Lett*., **87**, pp. 103508-1 – 103508-3.

[58] Pomeroy, J. W., Kuball, M., Uren, M. J., Hilton K. P., Balmer R. S., and Martin T., 2006. "Insights into electroluminescent emission from AlGaN/GaN field effect transistors using micro-Raman thermal analysis". *Appl. Phys. Lett*. **88**, pp. 023507-01 – 023507-03.

[59] J. S. Yuan, 2004. *SiGe, GaAs, and InP Heterojunction Bipolar Transistors*, John Wiley & Sons.

[60] Dutta N. K., 1981. "Calculated temperature dependence of threshold current of GaAs-AlxGa1–xAs double heterostructure lasers". *Appl. Phys. Lett*. **52**, pp. 70-73.

[61] Uji, T., Iwamoto, K. and Lang, R., 1981. "Nonradiative recombination in InGaAsP/InP light sources causing light emitting diode output saturation and strong laser-threshold-current temperature sensitivity", *Appl. Phys. Lett*., **38**, pp. 193 – 195.

[62] Fathpour, S., Mi, Z., Bhattacharya, P., Kovsh, A. R., Mikhrin, S. S., Krestnikov, I. L., Kozhukhov, A., V. and Ledentsov, N. N., 2004. "The role of Auger recombination in the temperature-dependent output characteristics (T0 = infinity) of p-doped 1.3 μm quantum dot lasers". *Appl. Phys. Lett*., **85**, pp. 5164-5166.

[63] Hayakawa, T., 1999. "Facet temperature distribution in broad stripe high power laser diodes", *Appl. Phys. Lett*., **75**, pp. 1467-1469

[64] Dilhaire, S., Grauby, S., Jorez, S., Lopez, L.-D.P., Schaub, E. and Claeys, W., 2001. "Laser diode COFD analysis by thermoreflectance microscopy", *Microelectron Reliab.*, **41**, pp. 1597- 1601.

[65] Marcatili E. A. J., 1974. "Slab-coupled waveguides", *Bell System J*., **53**, pp. 645-672.

[66] Walpole, J. N., Donnelly, J. P., Taylor, P. J., Missaggia, L. J., Harris, C. T., Bailey, R. J., Napoleone, A., Groves, S. H., Chinn, S. R., Huang, R. and Plant, J., 2002. "Slab-coupled 1.3-μm semiconductor laser with single-spatial large-diameter mode". *IEEE Photon. Technol. Lett*., **14**, pp. 756 – 758.

[67] Donnelly, J. P., Huang, R. K., Walpole, J. N.; Missaggia, L. J., Harris, C. T., Bailey, R. J., Plant, J., Mull, D. E., Goodhue, W. T., Taylor, P. J., Napoleone, A. and Turner, G. W., 2002. "Slab-coupled semiconductor lasers with single-spatial large-diameter mode*". Proceedings of the SPIE - The International Society for Optical Engineering*, v 4871, pp. 115-122.

[68] Huang, R. K., Donnelly, J. P., Missaggia, L. J., Harris, C. T., Plant, J., Mull, D. E. and Goodhue, W. D., 2003. "High-power nearly diffraction-limited AlGaAs-InGaAs semiconductor slab-coupled optical waveguide laser". *IEEE Photon. Technol. Lett*., **15**, pp. 900 – 902.

[69] Juodawlkis, P. W., Plant, J. J., Huang, R. K., Missaggia, L. J. and Donnelly, J. P., 2003. "High-power 1.5-μm InGaAsP slab-coupled optical waveguide amplifiers and lasers". *IEEE LEOS Annual Meeting Conference Proceedings*. **1**, pp. 425-426.

[70] Juodawlkis, P. W., Plant, J. J., Huang, R. K., Missaggia, L. J. and Donnelly, J. P., 2005. "High-power 1.5-μm InGaAsP-InP slab-coupled optical waveguide amplifier". *IEEE Photon. Tech. Lett*. **17** pp. 279 – 281.

[71] Plant, J. J., Gopinath, J. T., Chann, B., Ripin, D. J., Huang, R. K. and Juodawlkis, P. W., 2006. "250 mW, 1.5 μm monolithic passively mode-locked slab-coupled optical waveguide laser". *Optic. Lett.* **31**, pp. -223 – 225.

[72] Chan, P.K.L., Pipe, K.P., Plant, J.J., Swint, R.B. and Juodawlkis, P.W., 2006. "Temperature mapping and thermal lensing in large-mode, high-power laser diodes", *Appl. Phys. Lett*., **89**, pp. 201110-01 – 201110-03.

[73] Lewis, D., Dihaire, S., Phan, T., Quintard, V., Horrnung, V., and Claeys., W., 1998. "Modeling and experimental study of heat deposition and transport in a semiconductor laser diode," *Microelectronics Journal*, **29**, pp. 171-179.

[74] Zhu, C., Zhang, Y. G., Li, A. Z., and Zheng, Y. L., 2005. "Comparison of thermal characteristics of antimonide and phosphide MQW lasers", *Semiconductor Science and Technology*, **20**, pp. 563-567.

[75] Piprek, J., Abraham P., and Bowers, J. E., 2000. "Self-consistent analysis of high-temperature effects on strained-layer multiquantum-well InGaAsP-InP lasers', *IEEE Journal of Quantum Electronics*, **36**, pp. 366-374.

[76] Sweeney, S. J., Lyons, L. J., Adams, A. R. and Lock, D. A., 2003. "Direct measurement of facet temperature up to melting point and COD in high-power 980-nm semiconductor diode lasers"**,** *IEEE Journal of Selected Topics in Quantum Electronics*, **9**, pp.1325-1332.

[77] Sugimura, A., 1981, "Band-to-band Auger recombination effect on InGaAsP laser threshold*", IEEE Journal of Quantum Electronics*, **17 (5)**, 627-635

[78] Incropera, F. P. and Dewitt, D. P., 1996. *Fundamentals of Heat and Mass Transfer,* John Wiley & Sons.

[79] Coldren, L. A. and Corzine, S. W., 1995. *Diode lasers and photonic integrated circuits*, *John Wiley & Sons*.

[80] Chan, P. K. L., Sathe, A. D., Pipe, K. P., Plant, J. J., and Juodawlkis, P. W., 2005. "Time-resolved microscale temperature measurements of semiconductor lasers*", Intl. Mech. Eng. Cong. & Exp., Heat Transfer Div.*, November 5-11, Orlando, FL, USA.

[81] Pipe, K. P. and Ram, R. J., 2003. "Comprehensive heat exchange model for a semiconductor laser diode", *IEEE Phot. Tech. Lett*., **15**, pp. 504 -506.

[82] Chan P. K. L., Sathe, A. D., Pipe, K. P., Plant, J. J., Swint, R. B., and Juodawlkis, P. W., 2006 "Submicron thermal imaging of high power slab coupled optical waveguide laser (SCOWL)", *Intl. Mech. Eng. Cong. & Exp., Heat Transfer Div.,* November 5-10, Chicago, IL (2006).

[83] www.ioffe.ru/SVA/NSM/Semicond

[84] Gini, E. and Melchior, H., 1996. "Thermal dependence of the refractive index of InP measured with integrated optical demultiplexer", *J. Appl. Phys.,* **79**, pp. 4335 – 4337.

[85] Tanobe, H., 1997. "Temperature dependence of refractive index in InGaAsP/lnP for the design of a temperature insensitive arrayed waveguide grating", Pacific *Rim Conference on Lasers and Electro-Optics*, CLEO, pp. 283 - 284.

[86] Swaruwatari, M. and Nawata, K., 1979. " Semiconductor laser to single-mode fiber coupler", *Applied Optics*, **18 (11)**, pp.1847

[87] Holzmann, M, Baumgartner, P., Engel, C., Nützel, J. F., Abstreiter, G. and Schäffler F., 1996. "Fabrication of n- and p-channel in-plane-gate transistors from Si/SiGe/Ge heterostructures by focused laser beam writing". *Appl. Phys. Lett.*, **68**, pp. 3025 – 3027.

[88] Bhattacharya P., 1997. *Semiconductor optoelectronic devices*. Prentice Hall Inc., NJ.

[89] Fathpour, S., Mi, Z. and Bhattacharya, P., 2005. "Small-signal modulation characteristics of p-doped 1.1- and 1.3-μm quantum-dot lasers", *IEEE Photon. Technol. Lett.*, **17**, pp. 2250-2252.

[90] Mi, Z.; Bhattacharya, P. and Fathpour, 2005. “High-speed 1.3 μm tunnel injection quantum-dot lasers”, *Appl. Phys. Lett.*, **86**, pp. 153109-01 – 153109-03.

[91] Botez, D., Connolly, J.C. and Gilbert, D.B., 1981. “High-temperature CW and pulsed operation in constricted double-heterojunction AlGaAs diode lasers”. *Appl. Phys. Lett*., **39**, pp. 3 – 6.

[92] Bhattacharya, P., Ghosh, S., Pradhan, S., Singh, J., Wu, Z. K.,, Urayama, J., Kim, K. and Norris, T.B., 2003. “Carrier dynamics and high-speed modulation properties of tunnel injection InGaAs-GaAs quantum-dot lasers”, *IEEE J. Quantum Electron*. **39**, pp.952 – 962.

[93] Piprek, J.,White, J.K. and SpringThorpe, A.J., 2002. “What limits the maximum output power of long-wavelength AlGaInAs/InP laser diodes?”. *IEEE J. Quantum Electron.,* **38**, pp. pp.1253 – 1259.

[94] Puchert, R.; Baerwolff, A.; Voss, M.; Menzel, U.; Tomm, Jens W. and Luft, J., 2000. “Transient thermal behavior of high power diode laser arrays”, *IEEE Transactions on Components and Packaging Technologies*, **23**, pp. 95 – 100.

[95] Chan P. K. L., Pipe, K. P., Mi, Z., Yang, Y., Bhattacharya, P. and Lüerßen, D., 2006. "Thermal relaxation time and heat distribution in pulsed InGaAs quantum dot lasers", *Appl. Phys. Lett*., **89**, pp. 011110-01 – 011110-03.

[96] Tang, C. W., and VanSlyke, S. A., 1987. “Organic electroluminescent diodes,” *Appl. Phys. Lett*., **51**, pp. 913–915, 1987.

[97] Peumans, P., Yakimov, A., and Forrest, S. R., 2003. “Small molecular weight organic thin-film photodetectors and solar cells”, *Appl. Phys. Lett*., **93**, pp. 3693-3723.

[98] Ma, L., Xu, Q., and Yang, Y., 2004. "Organic nonvolatile memory by controlling the dynamic copper-ion concentration within organic layer", *Appl. Phys. Lett.*, **84**, pp. 4908-4910.

[99] Jung, J. M., Kwon, K. Y., Ha, T. H., Chung, B. H., and Jung, H. T., 2006. "Gold-conjugated protein nanoarrays through block-copolymer lithography: From fabrication to biosensor design", *Small*, **2**, pp.1010 – 1015.

[100] Shtein, M., Mapel, J., Benziger, J. B. and Forrest, S. R., 2002. "Effects of film morphology and gate dielectric surface preparation on the electrical characteristics of organic-vapor-phase-deposited pentacene thin-film transistors", *Appl. Phys. Lett*., **81**, pp. 268 – 270.

[101] Yu, H. H., Hwang, S. J., and Hwang, K. C., 2005. "Preparation and characterization of a novel flexible substrate for OLED", *Optics Communication*., **248**, pp. 51 – 57.

[102] O'Connor, B., An K. H., Zhao, Y., Pipe, K. P. and Shtein, M., 2007. "Fiber Shaped Organic Light Emitting Device", *Adv. Mat*., in press

[103] An, K. H., O'Connor, B., Pipe, K. P., Zhao, Y, and Shtein, M., 2006. "Organic light-emitting device on a scanning probe cantilever", *Appl. Phys. Lett*., **89**, pp. 111117-01 – 111117-03.

[104] Pope, M. and Swenberg, C. E., 1999. *Electronic Processes in Organic Crystals and Polymers*, Oxford University Press

[105] Baranovskii, S.D., Cordes, H., Hensel, F. and Leising, G., 2000. "Charge-carrier transport in disordered organic solids", *Phys. Rev. B*, **62**, pp. 7934-7938.

[106] Baranovskii, S.D., Zvyagin, I.P., Cordes, H., Yamasaki, S. and Thomas, P., 2002. "Percolation approach to hopping transport in organic disordered solids", *Phys. stat.* sol. *(B),* **230**, pp. 281 – 287.

[107] Schmechel R, 2003. "Hopping transport in doped organic semiconductors: A theoretical approach and its application to p-doped zinc-phthalocyanine", *J. Appl. Phys*., **93**, pp. 4653 – 4660.

[108] Bassler, H., 1993. "Charge transport in disordered organic photoconductors a Monte Carlo simulation study", *Phys. Stat. Sol. B*, **175**, pp. 15–56.

[109] Schmechel R, 2002. "Gaussian disorder model for high carrier densities: Theoretical aspects and application to experiments", *Phys. Rev. B*, **66**, pp. 235206-1 – 235206-6.

[110] Fritzsche, H., 1971. "A general expression for the thermoelectric power", *Solid State Comm*, **9**, pp. 1813 – 1815.

[111] Pyo, S., Son, H., Choi, K. Y., Yi, M. H. and Hong, S. K., 2005. "Low-temperature processable inherently photosensitive polyimide as a gate insulator for organic thin-film transistors", *Appl. Phys. Lett.*, **86**, pp. 133508-01 – 133508-03.

[112] Klauk, H., Halik, M., Zschieschang, U., Schmid, G., Radlik, W. and Weber, W., 2002. "High-mobility polymer gate dielectric pentacene thin film transistors", *J. Appl. Phys.*, **92**, pp. 5259 – 5263.

[113] Jin, Y. B., Rang, Z. L., Nathan, M. I., Ruden, P. P., Newman, C. R. and Frisbie, C. D., 2004. "Pentacene organic field-effect transistor on metal substrate with spin-coated smoothing layer", *Appl. Phys. Lett.*, **85**, pp. 4406 – 4408.

[114] Toccoli, T., Pallaoro, A., Coppede, N., Iannotta, S., De Angelis, F., Mariucci, L. and Fortunato, G., 2006. "Controlling field-effect mobility in pentacene-based transistors by supersonic molecular-beam deposition", *Appl. Phys. Lett.,* **88**, pp. 132106-01 – 132106-03.

[115] Pernstich, K. P., Haas, S., Oberhoff, D., Goldmann, C., Gundlach, D. J., Batlogg, B., Rashid, A. N. and Schitter, G., 2004. "Threshold voltage shift in organic field effect transistors by dipole monolayers on the gate insulator", *J. Appl. Phys.,* **96**, pp. 6431 – 6438.

[116] Lee, J., Kim, K., Kim, J. H., Im, S. and Jung, D. Y., 2003. "Optimum channel thickness in pentacene-based thin-film transistors", *Appl. Phys. Lett*., **83**, pp. 4169 – 4171.

[117] Ruiz, R., Papadimitratos, A., Mayer, A. C. and Malliaras, G. G., 2005. "Thickness dependence of mobility in pentacene thin-film transistors", *Adv. Mater*, **17**, pp. 1795 – 1798.

[118] Muck, T., Wagner, V., Bass, U., Leufgen, M., Geurts, J. and Molenkamp, L. W., 2004. "In situ electrical characterization of DH4T field-effect transistors", *Synth. Met*., **146**, pp. 317 – 320.

[119] Lin, Y. Y., Gundlach, D. J., Nelson, S. F. and Jackson, T. N., 1997. "Pentacene-based organic thin-film transistors", *IEEE. Trans. Electron. Device*., **44**, pp. 1325 – 1331.

[120] McDowell, M., Hill, I. G., McDermott, J. E., Bernasek, S. L. and Schwartz, J., 2006. "Improved organic thin-film transistor performance using novel self-assembled monolayers", *Appl. Phys. Lett*, **88**, pp. 073505-01 – 073505-03.

[121] Maennig, B., Pfeiffer, M., Nollau, A., Zhou, X., Leo, K. and Simon, P., 2001. "Controlled p-type doping of polycrystalline and amorphous organic layers: Self-consistent description of conductivity and field-effect mobility by a microscopic percolation model", *Phys. Rev. B*, **64**, 159208-01 – 159208-09.

[122] Völkel, A. R., Street, R. A. and Knipp, D., 2002. "Carrier transport and density of state distributions in pentacene transistors", *Phys. Rev. B*, **66**, pp.195336-1 – 195336-7.

[123] Pfeiffer, M., Beyer, A., Fritz, T. and Leo, K. , 1998. "Controlled doping of phthalocyanine layers by cosublimation with acceptor molecules: a systematic Seebeck and conductivity study", *Appl. Phys. Lett.*, **73**, pp. 3202 – 3204.

[124] Forrest, S. R., 1997. "Ultrathin organic films grown by organic molecular beam deposition and related techniques", *Chemical Reviews,* **97**, pp .1793 – 1896.

[125] Gu, G., Kane, M. G., Doty, J. E., and Firester, A. H., 2005. "Electron traps and hysteresis in pentacene-based organic thin-film transistors", *Appl. Phys. Lett*., **87**, pp. 243512-1 – 243512-3.

[126] Dimitrakopoulos, C.D., Brown, A.R. and Pomp, A., 1996. “Molecular beam deposited thin films of pentacene for organic field effect transistor applications”, *J. Appl. Phys*, **80**, pp. 2501 – 2508.

[127] Lin, Y. Y., Gundlach, D. I,. Nelson, S. F. and Jackson, T.N., 1997. “Pentacene-based organic thin-film transistors”, *IEEE Trans. Electron Device*, 44, pp. 1325 – 1331.